Under Pressure: Decoding the Effect of High Densities on Derived Nebular Properties

ZORAYDA MARTINEZ, 1,2 Danielle A. Berg, 1,2 Bethan L. James, 3 Karla Z. Arellano-Córdova, 4 Daniel P. Stark, 5 Peter Senchyna, 6 Evan D. Skillman, 7 Noah S. J. Rogers, 8 and John Chisholm, 1,2

Department of Astronomy, The University of Texas at Austin, 2515 Speedway, Stop C1400, Austin, TX 78712, USA
 ²Cosmic Frontier Center, The University of Texas at Austin, Austin, TX 78712, USA
 ³AURA for ESA, Space Telescope Science Institute, 3700 San Martin Drive, Baltimore, MD 21218, USA
 ⁴Institute for Astronomy, University of Edinburgh, Royal Observatory, Edinburgh, EH9 3HJ, UK
 ⁵Department of Astronomy, University of California, Berkeley, Berkeley, CA 94720, USA
 ⁶Observatories of the Carnegie Institution for Science, 813 Santa Barbara Street, Pasadena, CA 91101, USA
 ⁷Minnesota Institute for Astrophysics, University of Minnesota, 116 Church St. SE, Minneapolis, MN 55455
 ⁸Center for Interdisciplinary Exploration and Research in Astrophysics (CIERA), Northwestern University, 1800 Sherman Avenue, Evanston, IL 60201, USA

ABSTRACT

Recent JWST observations have uncovered a population of compact, high-redshift (z > 6) galaxies exhibiting extreme nebular conditions and enhanced nitrogen abundances that challenge standard chemical evolution paradigms. We present a joint UV and optical abundance analysis using a new suite of Cloudy photoionization models covering a wide density range $(n_e = 10^2 - 10^9 \text{ cm}^{-3})$, combined with HST and JWST spectroscopy for a sample of star-forming galaxies across $0.0 \lesssim z \lesssim 10.6$. We find that assuming uniform, low-density conditions $(n_e \sim 10^2 \text{ cm}^{-3})$ in high-density environments $(n_e \sim 10^5 \text{ cm}^{-3})$ can bias nebular diagnostics by overestimating T_e (up to 1800 K), overpredicting $\log U$ (by > 1 dex), and underestimating O/H (up to 0.67 dex), while only modestly inflating N/O. Therefore, robust abundance determinations at high-z require a multi-phase density model. Using this model, we recalculate O/H and N/O abundances for our sample and present the first log Udiagnostics and ICFs for high-ionization UV N lines. We find that the UV tracers systematically overestimate N/O by $\sim 0.3-0.4$ dex relative to the optical benchmark. We find that N/O increases with redshift, correlating with both n_e and star formation rate surface density ($\Sigma_{\rm SFR}$), suggesting that N/O is temporarily enhanced in compact, high-pressure environments. However, the n_e evolution with z is more gradual than the $(1+z)^3$ scaling of virial halo densities, suggesting that n_e evolution is shaped by both cosmological structure growth and baryonic processes. These trends point to prompt N/O enrichment potentially driven by very massive stars, with key implications for interpreting UV emission and determining reliable chemical abundances from JWST observations of the early universe.

1. INTRODUCTION

Observed nebular properties of galaxies are a powerful tool for probing galaxy evolution, and accurate interpretation of these properties requires robust methods of characterizing the physical conditions in galaxies across cosmic time. Notably, the chemical composition of a galaxy encodes vital details about star formation and the dynamic processes that reshape galaxies over time. Furthermore, total O/H and relative N/O abundances are useful measures of cumulative and recent star

Corresponding author: Zorayda Martinez zorayda@utexas.edu

formation history, respectively, since each one is sensitive to enrichment from stars of different masses. However, accurate abundance determinations require observations of faint emission lines, which are both highly sensitive to gas-phase physical conditions (e.g., temperature, density, ionization) and difficult to observe at higher redshifts. While many assumptions about ionized gas physical conditions, notably electron densities (n_e) , are made based on galaxy properties from detailed $z\sim 0$ measurements, recent JWST studies suggest that ionized gas conditions and chemical compositions evolve significantly across redshift (e.g., Isobe et al. 2023a; Abdurro'uf et al. 2024; Topping et al. 2025a). As such, environments with high n_e in the ionized gas may significantly bias UV and optical abundance determinations.

JWST abundance studies of high-redshift (z >6) galaxies have revealed a nitrogen overabundance where some very young galaxies exhibit enhanced relative N/O abundances, as probed by their highionization rest-frame ultraviolet (UV) N III] $\lambda 1750$ and N IV] $\lambda\lambda 1483,1487$ emission lines. While these highionization N lines are rarely seen at low-redshift (e.g., Mingozzi et al. 2022), which is in part due to the significant instrument challenges involved in obtaining UV and optical spectra for low-z galaxies, a surprising number of high-z galaxies, whose UV and optical spectra can both be traced by JWST, have been observed with very strong UV N emission line intensities (e.g., Pascale et al. 2023; Bunker et al. 2023; Ji et al. 2024; Marques-Chaves et al. 2024; Topping et al. 2024; Schaerer et al. 2024). Furthermore, the relative N/O abundances derived from the UV lines are significantly higher than the N/O abundances measured from low-ionization, optical N^+ and O^+ emission lines.

While persistent UV-optical discrepancies may suggest fundamentally different N production mechanisms in early galaxies, this discrepancy could also be driven by the observed high values of n_e at high-z (Isobe et al. 2023a; Abdurro'uf et al. 2024; Topping et al. 2025a). Noting that most abundance studies adopt a low-density assumption ($n_e \sim 10^2~{\rm cm}^{-3}$), Hayes et al. (2025) recently used stacks of high-z JWST spectra to show that oxygen abundances changed significantly when electron temperatures were derived from a high-density assumption rather than a low-density one. To date, the effects of electron density evolution on abundances have yet to be explored in individual galaxies, and continued use of low-z assumptions will potentially bias inferred galaxy properties.

Density, in particular, is extremely important for careful determination of other nebular properties. stantially increasing the electron density of ionized gas causes a rise in gas pressure according to the ideal gas law, where pressure scales with both density and temperature. At high-densities, recombination rates accelerate, which alters the balance between ionized and neutral species, shifting the ionization equilibrium and reducing the ionization parameter. In these extreme environments, key observables such as emission line strengths, temperature diagnostics, and inferred metallicities will experience notable changes. Additionally, collisional de-excitation begins to occur for different emission lines at different densities meaning that carefully deriving gas conditions will be more crucial than ever in the high-density environments that are more common at high-z. Finally, while past works have yet to systematically explore these effects, many traditional

diagnostics may overestimate the ionization state and underestimate the metallicity in high-densities, which in turn create potential biases in our understanding of star-forming environments, active galactic nuclei, and galaxy evolution.

Frameworks for interpreting ionized gas consist of ionization zones, where the gas closer to an ionizing source has higher ionization. In the common three-zone framework, the inner high-ionization zone is defined by the O^{+2} gas (> 35.1 eV), the intermediate-ionization zone is defined by the S^{+2} gas (23.3-34.8 eV), and the outer low-ionization zone is defined by the N^+ gas (14.5-29.6)eV). Observationally, it has been suggested that the ionized gas in galaxies exhibit a gradient in their electron temperatures and densities across the ionization structure of the gas (e.g., Berg et al. 2021; Mingozzi et al. 2022). Essentially, measured densities from lowionization emission lines are found to be lower than the densities derived from intermediate- and high-ionization emission lines. If these high-ionization densities evolve with redshift, similar to low-ionization densities, at highz our derived nebular properties may be significantly biased by these extreme densities.

Notably, within a given ionization zone density inhomogeneities can also have a significant impact on the inferred low-ionization nebular properties of local objects (e.g., Seaton & Osterbrock 1957; Peimbert 1971; Rubin 1989; Méndez-Delgado et al. 2023; Rickards Vaught et al. 2024). These density fluctuations can be negligible $(< 100 \text{ cm}^{-3}; \text{ e.g., García-Benito et al. } 2010)$ or more significant ($\simeq 600 \text{ cm}^{-3}$; e.g., Hamel-Bravo et al. 2024) such that density diagnostics with low critical densities (e.g., $n_{e,crit}([O II]) \sim 10^3 \text{ cm}^{-3}$) will be significantly affected. While these n_e -fluctuations may evolve with z, only a handful of works have spatially mapped n_e at $z \gtrsim$ 2 (e.g., Cresci et al. 2023; Marconcini et al. 2024) and find variations that are similar to local results suggesting minimal redshift evolution in n_e -fluctuations. However, integrated densities from a given ion have been observed to increase at high-z (i.e., $n_e \gtrsim 10^5 \text{ cm}^3$) such that diagnostics with low critical densities are in the high-density limit, where most of their flux will be collisionally suppressed. As a result, even when such diagnostics are detected, they trace only the diffuse component and systematically underestimate the true densities of the ionized gas. This limitation is especially important for interpreting high-redshift measurements that rely exclusively on optical or NIR rest-frame lines. Fortunately, the low-critical density diagnostics tend to characterize the lower ionization ions used in this work, but UV N emitters are inherently high-ionization objects and so

the low-ionization emission lines only make a small contribution to the total abundance.

Building on the low-z foundation of density studies, we explore the more extreme nebular conditions of highz galaxies. We examine the effects of high-densities on determinations of nebular properties including electron temperature, ionization parameter, total O/H abundances, relative N/O abundances, and the overall impact on chemical evolution trends. Additionally, we only explore stellar populations as an ionizing source, but future follow-up work will examine other ionizing sources. We detail our sample of UV N-emitting galaxies from 0 < z < 11 in Section 2 and our robust emission line measurements, where possible, in Section 3. We present a new custom suite of Cloudy photoionization models that accounts for the observed ionized gas conditions up to $n_e \sim 10^9~{\rm cm}^{-3}$ and significant super-solar N/O enhancements in Section 4. We examine the effects of increasing n_e in a uniform density model in Section 5, exploring emission line diagnostics in § 5.1, electron temperatures in § 5.2, and ionization parameters, ionization correction factors, and abundances in § 5.3. A summary of these n_e effects along with a more observationallymotivated high-density core model is discussed in Section 5.6. In Section 6, we recalculate abundances for our sample using a multi-phase density model. We discuss the implications of our results on the evolution of N/O abundances in Section 7, with special consideration for the evolution of density (\S 7.1) and star formation rate surface density (\S 7.2). Finally, we provide a summary of our work and key conclusions in Section 8. Note that we use vacuum wavelengths throughout this work.

2. SAMPLE & DATA

In order to explore the conditions producing extreme UV N emission at high redshifts and the role that density plays, we select a sample of galaxies spanning $0 \lesssim z \lesssim 10.6$ with UV N line detections, either N IV] $\lambda\lambda 1483,1487$ or N III] $\lambda 1750^1$, and intermediate-or high-ionization electron density measurements from C III] or N IV], respectively. The resulting sample consists of 17 objects that we divide into two subsamples: the Low-z Sample (z < 1) and the High-z Sample (z > 1). The Low-z Sample consists of 8 nearby objects that we describe below in Section 2.1. The remaining 9 objects of the High-z Sample are intermediate-to

high-z objects selected from the literature as described in Section 2.2. Relevant information about our sample and corresponding references can be found in Table 1. We require that every object in our sample has at least an intermediate- or high-ionization density diagnostic. The available high-ionization temperature and density diagnostics for each object can found in Table 2.

2.1. Low-z Sample

The Low-z Sample was difficult to construct because very few rest-UV N emission line detections exist in the literature. We searched the literature for N IV] or N III] detections, finding nine galaxies with z < 0.1. We note that no galaxies with high-ionization UV N detections have yet been found for $0.1 < z < 1.0^2$. Seven of these galaxies are taken from the COS Legacy Archive Spectroscopy SurveY (CLASSY; Berg et al. 2022; James et al. 2022). CLASSY consists of 45 nearby star-forming galaxies with high-resolution rest-frame far-UV (FUV) HST/COS spectra, which allows detailed studies of nebular emission lines that are only possible with local galaxies.

One additional object is the extremely metal-poor $(Z<0.05Z_{\odot})$ galaxy Leo P (Skillman et al. 2013), whose rest-UV spectra are taken from Telford et al. (2023) and the HST-GO-17102 program (PI D. Berg). Following the CLASSY coadding processes described in Berg et al. (2022), we combined the high-resolution G130M and G160M gratings (from Telford et al. 2023) with the low-resolution G140L grating (from HST-GO-17102) to cover both the N IV] and N III] features, as well as C III] $\lambda\lambda1907,1909$. The multi-step process includes extracting, reducing, aligning, and coadding the spectra from the different gratings. The final spectrum is shown in Figure 17 in the Appendix.

Properties of the Low-z Sample are listed in Table 1. The entire Low-z Sample has high-quality rest-UV and optical spectra that cover density diagnostics in both low-ionization (e.g., [O II] and [S II]) and high-ionization gas (e.g., N IV], C III], and [Ar IV]), as well as low- and high-ionization N emission from [N II] $\lambda 6585$ and N III] $\lambda 1750$ and/or N IV] $\lambda \lambda 1483,1487$, respectively, (Mingozzi et al. 2022). Thus, the power of the Low-z Sample lies in its detailed dataset, which enables calculations of multi-phase gas properties and the first self-consistent comparison of N/O abundances derived from low- and high-ionization emission lines.

 $^{^1}$ N III] is a quintuplet composed of emission lines at $\lambda1746.82,$ $\lambda1748.65,~\lambda1749.67,~\lambda1752.16,$ and $\lambda1754.00.$ Note that the $\lambda1749.67$ and $\lambda1752.16$ lines are typically the strongest, but their ratio is density sensitive. In this work, we use N III] $\lambda1750$ to represent the sum of the quintuplet.

 $^{^2}$ From our experience with COS gratings, the sensitivity extends only to about 2000Å, which skews detections of towards N IV] or N III] to z<0.1

The N III] and N IV] emission line portions of the rest-UV spectra of the Low-z Sample are shown in Figure 1. Five of the nine galaxies have visible N III] $\lambda 1750$ emission and four have N IV] $\lambda \lambda 1483,1487$. Interestingly, no objects have significant emission from both N III] and N IV]. Given that N⁺³ emission requires higher ionization and excitation energies than N⁺², different physical conditions are needed to produce the observed dichotomy in N IV] and N III] detections in our sample.

2.2. High-z Sample

The primary goal of this work is to assess the evolution of gas density and its effect on observed nebular conditions and abundances, including the significantly N-enriched high-z galaxies observed with JWST. Therefore, we searched the literature for z>1 galaxies³ with reported N III] $\lambda 1750$ or N IV] $\lambda \lambda 1483,1487$ detections to form our the High-z Galaxy Sample. In order to perform robust calculations of nebular properties, we also limited our sample to sources that have published attenuation values (E(B-V)) or multiple Balmer line measurements from which we could derive E(B-V). As a result, we found nine galaxies in the redshift range of 1.3 < z < 10.6 with N III] or N IV] detections.

The properties of the High-z Sample are listed in Table 1. In contrast to the Low-z Sample, all nine high-z galaxies have N III] detections, and six of these also have N IV] $\lambda\lambda 1483,1487$ detections. However, only four of these galaxies have sufficiently red optical spectra from which we can derive N/O abundances using the low-ionization [N II] $\lambda 6585$ and [O II] $\lambda\lambda 3727,3730$ emission lines. Note that this sample includes the extreme GN-z11 galaxy, enabling us to examine its properties against a robust sample of high-ionization N emitters with density measurements across cosmic time.

3. EMISSION LINE MEASUREMENTS

We collated emission line measurements from the literature when available and measured emission line fluxes from archival spectra in all other cases. While we were able to collect all of the necessary emission line measurements from the literature for the High-z Sample, the Low-z Sample emission line measurements are mixed. For the Low-z Sample, all necessary optical emission lines have been previously reported, but

few rest-UV N fluxes exist. In curating this sample, we find three CLASSY galaxies without prior N III] emission line measurements in the literature. Therefore to maintain consistency in the UV emission line measurements of our Low-z Sample, we fit all the UV emission lines for the eight objects in the Low-z Sample. We find that when compared to Mingozzi et al. (2022), our N III], N IV], and O III] emission lines measurements agree within 3σ . In the case of the Highz Sample, for RXCJ2248-ID, GDS 3073, J1723+3411, CEERS 1019, SL2S J0217, Lynx, and A1703-zd6, we use the flux measurements presented in Topping et al. (2024), Ji et al. (2024), Rigby et al. (2021), Marques-Chaves et al. (2024), Berg et al. (2018), Fosbury et al. (2003), and Topping et al. (2025b), respectively. For GN-z11, all fluxes are from Bunker et al. (2023) except [O III] $\lambda 5008$, which we scaled from Álvarez-Márquez et al. (2025) to match the other fluxes. Additionally, we use the N IV] $\lambda 1483/\lambda 1487$ ratio for GN-z11 from Maiolino et al. (2024) in order to decompose the combined flux N IV] $\lambda\lambda 1483,1487$ reported in Bunker et al. (2023). Finally, for the Sunburst Arc, we obtain the UV flux measurements from Pascale et al. (2023) and the optical fluxes from Rivera-Thorsen et al. (2024), which agrees within uncertainties with the measurements presented by Welch et al. (2025).

Emission-lines were fit using the LMfit package in python. Each line was fit simultaneously using a Gaussian plus linear continuum and constrained by a single full width at half maximum (FWHM) velocity width. The resolution of our spectra enables us to fit the N IV] emission as a doublet, whereas the N III] emission is often blended and weak in the individual lines and so best fit with a single Gaussian whose width is allowed to vary. There are two exceptions: J0127-0619 and Leo P. For J0127-0619, we fit three individual lines in the N III] $\lambda 1750$ complex and for Leo P, we fit the two strongest lines. The uncertainties on the line fluxes are the estimated standard error derived from the least-squares minimization in LMfit, which considers the uncertainty on the Gaussian profile and linear continuum.

We present the flux measurements for each of the 9 objects in our Low-z Sample in Table 6 in the Appendix. To be reported, we require at least one N IV] line detection with signal to noise (SN) greater than 2 and the integrated N III] line flux to have SN> 2. Figure 1 shows the UV N profiles for the Low-z Sample and the emission line fits (red) for the eight galaxies without previous N lines reported.

 $^{^3}$ We utilize z>1 as the qualifier for the High–z Sample since this is the redshift at which [O III] $\lambda5008$ will redshift past 1 $\mu\mathrm{m}$, which is usually beyond the range of most ground based optical spectrographs.

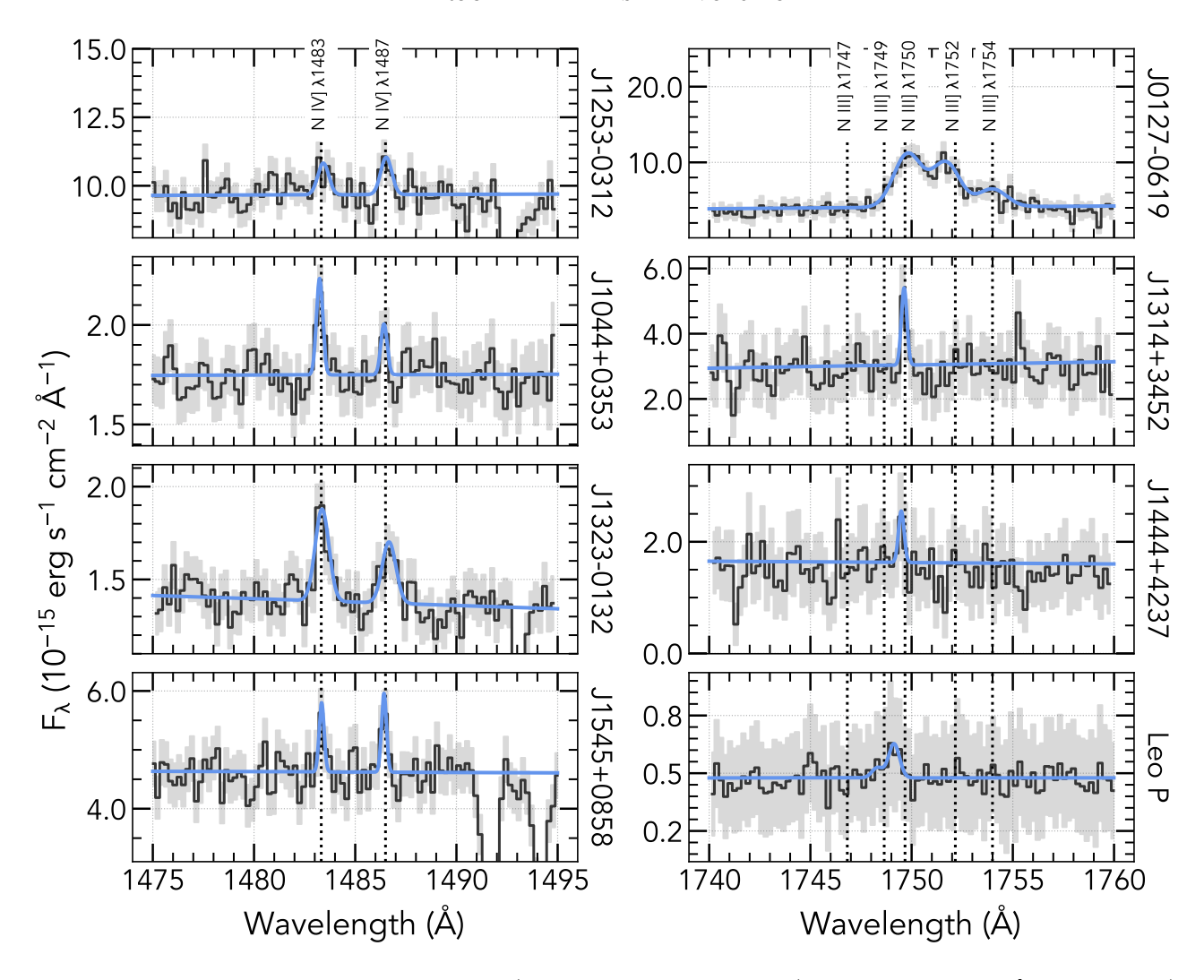


Figure 1. Rest-UV spectra for the Low-z Sample (see Section 2.1 and Table 1). The detected N IV] $\lambda\lambda 1483,1487$ (left) and N III] $\lambda 1750$ (right) emission profiles are shown; four galaxies have N IV] $\lambda\lambda 1483,1487$ emission and five have N III] $\lambda 1750$ emission, but none have both. We plot the emission line fits (blue line) for the eight of these galaxies without reported N IV] and N III] line fluxes in the literature.

Dereddened emission line intensities $(I_{\lambda}/I_{H\beta}^4)$ are determined using the nebular E(B-V) values in the literature for each object in our sample. We note that all the E(B-V) used in this work can be found in Tables 6 and 7 in the Appendix. For objects that lack published E(B-V) values, we determine E(B-V) using the published $H\alpha$, $H\beta$, and $H\gamma$ fluxes with the theoretical Balmer ratio assuming case B, $T_e=1.5\times10^4$ K, $n_e=10^2$ cm⁻³, and the parameterized extinction law of Cardelli et al. (1989). We note that for three of these objects the reddening derived from the Balmer

series emission returns a negative E(B-V). In these cases, we assume that there is no reddening from the host galaxy, but recent works have explored scenarios where the Balmer ratios would deviate from case B recombination (e.g. Scarlata et al. 2024; Yanagisawa et al. 2024; McClymont et al. 2025; Arellano-Córdova et al. 2025a). The E(B-V) values are then used to deredden the rest-optical emission lines assuming the Cardelli et al. (1989) extinction law and the rest-UV emission lines assuming the Reddy et al. (2016) extinction law. All line intensities used for this work, including those adapted from literature sources are reported in Tables 6 and 7 for the low-z and high-z samples, respectively, in the Appendix.

4. PHOTOIONIZATION MODELS

 $^{^4}$ We present UV emission line measurements for our Low-z Sample relative to $I_{\rm C~III]}$ to avoid introducing further uncertainties due to flux calibrations between the UV and optical spectra.

Table 1. UV N-Emitting Sample Properties

| | | Coords. | | $\log M_{\star}$ | log SFR | R_e | $\log \Sigma_{ m SFR}$ | 12+ | | N | Detection | ons |
|-------|---------------|----------------------|--------|------------------|-----------------------------------|-------|--|-------------------|------|--------|-----------|-------|
| Label | Name | (J2000) | z | (M_{\odot}) | $(\frac{M_{\odot}}{\mathrm{yr}})$ | (pc) | $\left(\frac{M_{\odot}}{\mathrm{yr~kpc^2}}\right)$ | $\log({\rm O/H})$ | Ref. | [N II] | N III] | N IV] |
| Low-z | Sample: | | | | | | | | | | | |
| Lz-1 | J0127 - 0619 | 21.89796, -6.32668 | 0.0054 | 8.74 | -0.75 | 20.0 | +1.85 | 7.68 | (1) | ✓ | ✓ | X |
| Lz-2 | J1314 + 3452 | 198.69736, +34.88328 | 0.0029 | 7.56 | -0.67 | 30.0 | +1.58 | 8.26 | (1) | ✓ | ✓ | × |
| Lz-3 | J1444+4237 | 221.04776, +42.62655 | 0.0023 | 6.48 | -1.94 | 45.0 | -0.04 | 7.64 | (1) | ✓ | ✓ | × |
| Lz-4 | Leo P | 155.43792, +18.08811 | 0.0009 | 5.75 | -4.31 | 0.4 | +1.69 | 7.17 | (2) | ✓ | ✓ | × |
| Lz-5 | J1253 - 0312 | 193.27487, -3.21637 | 0.0227 | 7.65 | +0.56 | 390.0 | +0.58 | 8.06 | (1) | ✓ | × | ✓ |
| Lz-6 | J1044+0353 | 161.24080, +3.88699 | 0.0129 | 6.80 | -0.59 | 100.0 | +0.61 | 7.45 | (1) | ✓ | × | ✓ |
| Lz-7 | J1323 - 0132 | 200.94775, -1.54776 | 0.0225 | 6.31 | -0.72 | 100.0 | +0.48 | 7.71 | (1) | ✓ | × | ✓ |
| Lz-8 | J1545 + 0858 | 236.43147, +8.96704 | 0.0377 | 7.52 | +0.37 | 250.0 | +0.78 | 7.75 | (1) | ✓ | X | ✓ |
| High- | z Sample: | | | | | | | | | | | |
| Hz-1 | RXCJ2248-ID | 342.17972, -44.53300 | 6.106 | 8.05 | +1.80 | 22.0 | +4.32 | 7.43 | (4) | ✓ | ✓ | ✓ |
| Hz-2 | GN-z11 | 189.10605, +62.24205 | 10.621 | 8.73 | +1.27 | 64.0 | +2.86 | 7.82 | (5) | X | ✓ | ✓ |
| Hz-3 | GDS 3073 | 53.07888, -27.88416 | 5.500 | 9.52 | +1.95 | 110.0 | +3.07 | 8.00 | (6) | ✓ | ✓ | ✓ |
| Hz-4 | Sunburst | 237.52013, -78.18314 | 2.371 | 9.04 | +1.00 | 7.8 | +4.42 | 7.96 | (7) | ✓ | ✓ | × |
| Hz-5 | J1723 + 3411 | 260.90067, +34.19946 | 1.329 | 8.77 | +0.90 | | | 8.30 | (8) | ✓ | ✓ | × |
| Hz-6 | CEERS 1019 | 215.03539, +52.89066 | 8.678 | 9.30 | +2.17 | 112.0 | +3.27 | 7.70 | (9) | X | ✓ | ✓ |
| Hz-7 | $SL2S\ J0217$ | 34.40515, -5.22494 | 1.844 | 8.26 | +1.35 | 300.0 | +1.60 | 7.50 | (10) | X | ✓ | × |
| Hz-8 | Lynx | 132.20317, +44.93044 | 3.300 | 7.67 | +1.68 | | | 7.76 | (11) | X | ✓ | ✓ |
| Hz-9 | A1703-zd6 | 198.75423, +51.83466 | 7.044 | 7.70 | +1.49 | 120.0 | +2.53 | 7.47 | (12) | X | ✓ | ✓ |

Note—Properties for our rest-UV N-emitter Low-z ($z \sim 0$) and High-z (1 < z < 11) Samples. Columns 1 and 2 list the label used in this work and the literature name of each object, followed by the coordinate R.A. and Decl. of their spectral observations and redshifts in Columns 3 and 4. Galaxy stellar mass, SFR, rest-UV effective radius, SFR surface density, and metallicity are listed in Columns 5, 6, 7, 8, and 9 respectively, with their corresponding references in Column 10. Finally, we note which rest-UV and optical N lines are detected at a 2σ significance in each object in Columns 11, 12, and 13.

References: (1) Berg et al. (2022), Mingozzi et al. (2022), Xu et al. (2022); (2) Skillman et al. (2013), McQuinn et al. (2015), Telford et al. (2023); (3) Berg et al. (2019) (4) Topping et al. (2024); (5) Tacchella et al. (2023), Bunker et al. (2023), Maiolino et al. (2024), Senchyna et al. (2024), Cameron et al. (2023), Álvarez-Márquez et al. (2025); (6) Vanzella et al. (2010), Grazian et al. (2020), Barchiesi et al. (2023), Übler et al. (2023), Ji et al. (2024); (7) Vanzella et al. (2022), Meštrić et al. (2023), Pascale et al. (2023), Rivera-Thorsen et al. (2024), Welch et al. (2025); (8) Rigby et al. (2021), Welch et al. (2024); (9) Marques-Chaves et al. (2024); (10) Berg et al. (2018); (11) Fosbury et al. (2003), Villar-Martín et al. (2004), Sanders et al. (2020); (12) Topping et al. (2025b);

In order to properly evaluate the effects of density structure on derived nebular properties, we computed new Cloudy 23.01 photoionization models (Chatzikos et al. 2023; Gunasekera et al. 2023) over a large range of densities. We assumed a spherical geometry and used "Binary Population and Spectral Synthesis" (Eldridge et al. 2017, BPASSv2.14) burst models combined with an ionization parameter to define the input ionizing radiation field. For these models we intentionally covered an extended parameter space appropriate to the conditions of our sample galaxies observed across cosmic time. This included an age range of $10^{6.0} - 10^{7.6}$ yr to probe the young bursts likely associated with the very-highionization emission observed, a range of stellar metallicities $(Z_{\star} = Z_{\text{neb}} = 0.01, 0.02, 0.03, 0.04, 0.06, 0.08 =$ $0.05, 0.10, 0.15, 0.20, 0.30, 0.40Z_{\odot}$) that cover the observed gas-phase abundances of our sample and the expected values for early galaxies, an expanded range of N/O and C/O abundances (described below), and a large range of uniform gas densities ($10^2 < n_e < 10^9$) to explore the effects of high density (i.e., pressure). Note that great care must be taken to consider the sensitivity range of observed density diagnostics in comparison to photoionization models.

We also explored a large range in ionization parameter of $-3.5 < \log U < -1.0$. Cloudy defines the dimensionless ionization parameter as

$$U \equiv \frac{Q(\mathrm{H})}{4\pi r_o^2 n_{\mathrm{H}} c},\tag{1}$$

where Q(H) is the number of H-ionizing photons at the illuminated face of the gas cloud, r_o is the distance from the ionizing source to the cloud face, n_H is the total H density at the cloud face, and c denotes the speed of light. Note that in a fully ionized nebula, n_H will be approximately equivalent to the electron density, n_e , but not exactly because He contributes a non-negligible

Table 2. Electron Temperature and Density Diagnostics

| | Availa | ble High- | Ion. Diag | nostics |
|---------------|-----------------------|--|-------------------------------|------------------------------|
| Name | $T_{e,high}$ O^{+2} | $\begin{array}{c} n_{e,int.} \\ \mathbf{C}^{+2} \end{array}$ | $n_{e,high}$ Ar ⁺³ | $n_{e,high}$ N ⁺³ |
| Low-z Sample | e: | | | |
| J0127-0619 | ✓ | ✓ | X | Х |
| J1314 + 3452 | ✓ | ✓ | ✓ | X |
| J1444+4237 | ✓ | ✓ | X | X |
| Leo P | ✓ | ✓ | ✓ | X |
| J1253-0312 | ✓ | ✓ | ✓ | ✓ |
| J1044+0353 | ✓ | ✓ | ✓ | ✓ |
| J1323-0132 | ✓ | ✓ | ✓ | 1 |
| J1545+0858 | ✓ | 1 | ✓ | ✓ |
| High-z Sampl | e: | | | |
| RXCJ2248-ID | ✓ | 1 | X | 1 |
| GN-z11 | ✓ | X | X | 1 |
| GDS 3073 | ✓ | X | X | 1 |
| Sunburst | ✓ | ✓ | X | X |
| J1723 + 3411 | ✓ | ✓ | X | X |
| CEERS 1019 | ✓ | X | X | 1 |
| $SL2S\ J0217$ | ✓ | ✓ | X | X |
| Lynx | ✓ | ✓ | X | 1 |
| A1703-zd6 | ✓ | ✓ | Х | ✓ |

Note— The high-ionization, high-excitation diagnostics available for each object in our sample are denoted by a checkmark if their emission line ratios are detected (SNR > 2). Each objects has both the T_e diagnostic and one of the n_e diagnostics, enabling a calculation of $T_{e,high}$ with a n_e from the a similar ionization zone.

fraction of electrons through photoionization. The density dependence suggests that the ionization parameters inferred for high—z galaxies will be significantly reduced when large gas densities are present (e.g., Reddy et al. 2023). Overall, $\log U$ is an important parameter that gives insight into the strength of the radiation field and is critical for understanding the physical conditions in the ISM.

The GASS10 solar abundance ratios within Cloudy were used to initialize the relative gas-phase abundances. These abundances were then scaled to cover the observed range in nebular metallicity and relative C/O and N/O abundances. The expanded ranges in relative N/O and C/O were motivated to test the validity of the extremely large range of values reported at high-z from JWST observations (e.g., Cameron et al. 2023; Pascale

et al. 2023; Ji et al. 2024; Marques-Chaves et al. 2024)⁵, resulting in coverage of $0.05 \lesssim (C/O)/(C/O)_{\odot} \lesssim 3$, corresponding to a range of $-1.75 < \log(C/O) < +0.25$, and $0.25 \lesssim (N/O)/(N/O)_{\odot} \lesssim 75$, corresponding to a range of $-1.5 < \log(N/O) < +1.0$.

5. LOW- TO HIGH- DENSITY MODELS

N and O are two of the most important elements for understanding chemical evolution. O is predominantly synthesized in short-lived, massive stars (MSs; $M_{\star} \gtrsim 10 \ M_{\odot}$, e.g., Kobayashi et al. 2020) and ejected into the ISM via core-collapse supernovae (CCSNe) on timescales of $\lesssim 10$ Myr (the peak of CCSNe). It is an important element for cooling processes and dust formation, and is used as a proxy for the gas-phase metallicity of a galaxy $(Z = 12 + \log(O/H))$. Since O/H abundance increases with each new generation of stars (Wheeler et al. 1989), it serves as a robust tracer of the cumulative SFH and the current evolutionary state of a galaxy. N, in contrast, is generated in both MSs and intermediate mass stars (IMSs; 10 $M_{\odot} \gtrsim M_{\star} \gtrsim 2 M_{\odot}$, e.g., Kobayashi et al. 2020), and, therefore, produced on longer time scales (> 200 Myr). As a result, N/O is sensitive to the relative contribution of high-mass versus intermediate-mass stars to a galaxy's chemical enrichment.

We use the new photoionization model grid described in Section 4 to explore the effects of increasing density on measured nebular conditions and abundances in the simple case of a constant, uniform density model. Specifically, we explore the effect on diagnostic emission line ratios (\S 5.1), derived electron temperatures (\S 5.2), directmethod abundances (\S 5.3 - 5.5), ionization parameters (\S 5.5.1), and ionization correction factors (\S 5.5.1).

5.1. Emission Line Diagnostics

Emission line ratios that are essential to determining nebular abundances in galaxies are sensitive to both electron temperature (T_e) and density (n_e) . In particular, the collisionally-excited metal lines used in these ratios experience an exponential dependence on T_e , which is dictated by the Maxwell-Boltzmann distribution of electron kinetic energies ($\propto e^{-\Delta E/kT_e}$). The critical density, $n_{e,crit}$, marks the point where the spontaneous emission and collisional de-excitation rates are equal (e.g., Osterbrock & Ferland 2006; Draine 2011). At low-densities $(n_e \ll n_{e,crit})$, the dominant decay mechanism

⁵ We note that UV emission lines are extremely sensitive to T_e and some current measurements lack a robust T_e detection, which could severely bias these derived values.

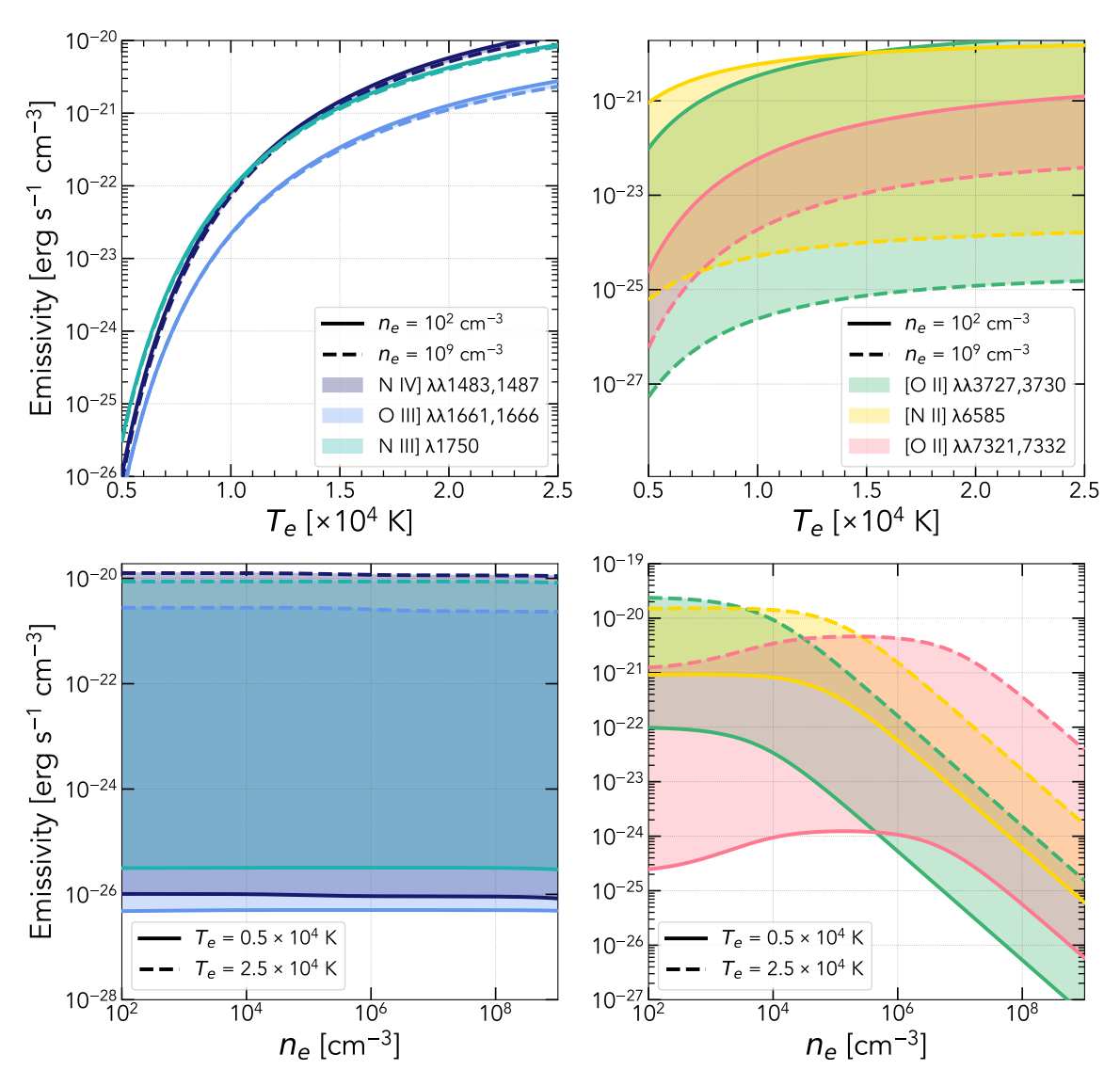


Figure 2. The emissivities of N IV] $\lambda\lambda 1483,1487$, N III] $\lambda 1750$, and O III] $\lambda\lambda 1661,1666$, determined with PyNeb, are shown in the left column, while the right column shows the same for the emissivities of [O II] $\lambda\lambda 3727,3730$, [N II] $\lambda6584$, and [O II] $\lambda\lambda 7321,7332$. The upper panels show emissivities as a function of T_e (5,000 to 25,000 K), and the lower panels describe these emissivities as a function of n_e (10² - 10⁹ cm⁻³). Note that we show the full range of densities used in photoionization models to show the different ranges each line is sensitive over. The top panels illustrate that n_e has a larger impact on optical lines that have lower critical n_e , while the bottom panels show that UV lines are more impacted by T_e than the optical lines given that they have higher excitation energies.

is spontaneous emission; however, at higher densities $(n_e \gtrsim n_{e,crit})$ the contribution from collisional deexcitation will become increasingly important. Note that while $n_{e,crit}$ marks the equivalence between deexcitation mechanisms, the contribution from collisional deexcitation becomes significant at much lower densities. To facilitate the discussion in this section, we present Table 3 which contains useful emission line characteristics for many of the most relevant emission lines in this work.

In Figure 2 we use the getEmissivity function in PyNeb (Luridiana et al. 2012, 2015) to plot the emissiv-

ities of the UV and optical O and N emission lines as a function of electron T_e (upper panels) and n_e (lower panels). The upper left panel of Figure 2 shows that strong emission ($\gtrsim 10^{-21}~{\rm erg~s^{-1}~cm^{-3}}$) from the high-ionization UV N and O emission lines require high T_e ($T_e \gtrsim 1.5 \times 10^4~{\rm K}$) due to their high-excitation energies ($\gtrsim 7.1~{\rm eV}$). In general, UV emission lines have higher excitation energies than optical emission lines, which are plotted with respect to T_e in the upper right panel of Figure 2 (e.g., Osterbrock 1989; Draine 2011). For example, the excitation energies of the

Table 3. Emission Line Characteristics

| | λ_{vac} | Transition | I.P. | E_{exc} | $n_{e,crit}$ |
|----------|-----------------|-------------------------|----------|-----------|-----------------------|
| Line | (Å) | $(l_u \rightarrow l_l)$ | (eV) | (eV) | (cm^{-3}) |
| | | UV Emissio | on Lines | | |
| N IV] | 1483.321 | $4 \rightarrow 1$ | 47.445 | 8.359 | 1.83×10^{5} |
| N IV] | 1486.496 | $3 \rightarrow 1$ | 47.445 | 8.341 | 5.62×10^{9} |
| O III] | 1660.809 | $6 \rightarrow 2$ | 35.121 | 7.479 | $4.87{\times}10^{10}$ |
| O III] | 1666.150 | $6 \rightarrow 3$ | 35.121 | 7.479 | 4.87×10^{10} |
| N III] | 1746.823 | $4 \rightarrow 1$ | 29.601 | 7.098 | 1.16×10^{9} |
| N III] | 1748.646 | $3 \rightarrow 1$ | 29.601 | 7.090 | $1.12{\times}10^{10}$ |
| N III] | 1749.674 | $5 \rightarrow 2$ | 29.601 | 7.108 | 6.84×10^{9} |
| N III] | 1752.160 | $4 \rightarrow 2$ | 29.601 | 7.098 | 1.16×10^{9} |
| N III] | 1753.995 | $3 \rightarrow 2$ | 29.601 | 7.090 | $1.12{	imes}10^{10}$ |
| C III] | 1906.683 | $4 \rightarrow 1$ | 24.384 | 6.503 | $8.59{	imes}10^{4}$ |
| [C III] | 1908.734 | $3 \rightarrow 1$ | 24.384 | 6.496 | 1.14×10^{9} |
| [O III] | 2321.663 | $5 \rightarrow 2$ | 35.121 | 5.354 | $3.12{\times}10^7$ |
| | О | ptical Emis | sion Lin | es | |
| [O II] | 3727.092 | $3 \rightarrow 1$ | 13.618 | 3.327 | 4.77×10^{3} |
| [O II] | 3729.875 | $2 \rightarrow 1$ | 13.618 | 3.324 | $1.38{	imes}10^{3}$ |
| [O III] | 4364.435 | $5 \rightarrow 4$ | 35.121 | 5.354 | 2.88×10^{7} |
| [Ar IV] | 4712.579 | $3 \rightarrow 1$ | 40.735 | 2.613 | $1.73{\times}10^4$ |
| [Ar IV] | 4741.448 | $2 \rightarrow 1$ | 40.735 | 2.615 | $1.56{	imes}10^{5}$ |
| [O III] | 5008.239 | $4 \rightarrow 3$ | 35.121 | 2.514 | $7.83{	imes}10^{5}$ |
| [N II] | 6585.270 | $4 \rightarrow 3$ | 14.534 | 1.899 | $1.04{	imes}10^{5}$ |
| [S II] | 6718.291 | $3 \rightarrow 1$ | 10.360 | 1.845 | $1.92{\times}10^3$ |
| [S II] | 6732.670 | $2 \rightarrow 1$ | 10.360 | 1.842 | $5.07{\times}10^3$ |
| [Ar III] | 7137.755 | $4 \rightarrow 1$ | 27.630 | 1.737 | $5.11{\times}10^6$ |
| [O II] | 7320.935 | $5 \rightarrow 2$ | 13.618 | 5.018 | $4.70{\times}10^6$ |
| [O II] | 7322.002 | $4 \rightarrow 2$ | 13.618 | 5.017 | $6.88{	imes}10^{6}$ |
| [O II] | 7331.680 | $5 \rightarrow 3$ | 13.618 | 5.018 | $4.70{\times}10^6$ |
| [O II] | 7332.751 | $4 \rightarrow 3$ | 13.618 | 5.017 | 6.88×10^{6} |
| | | | | | |

Note—To aid in the discussion provided in Section 5.1, we provide the vacuum wavelengths, transitions, ionization potential energies, excitation energies, and critical densities for the emission lines relevant to this work.

most common O⁺² emission lines in increasing energy are [O III] $\lambda 5008$, [O III] $\lambda 4364$, [O III] $\lambda 2322$, and O III] $\lambda 1666$ ($E_{exc}=2.51, 5.35, 5.35, 7.48$ eV; for more see Table 3). Thus, given their higher excitation energies, strong detections of the UV O and N emission lines require high electron temperatures and/or high densities near or less than their respective critical densities ($n_{e,crit}=7.8\times 10^5, 2.9\times 10^7, 3.1\times 10^7, 4.9\times 10^{10}$ cm⁻³; for more see Table 3).

The lower right panel of Figure 2 shows emissivities of the low-ionization optical O and N emission lines as a function of density. Note that while our density diagnostics are only sensitive up to $\sim \! 10^7 \ \mathrm{cm}^{-3}$ but we show larger range of densities over which emission lines are affected. Emission from a given line begins to de-

crease as the density approaches its $n_{e,crit}$ and collisional de-excitation becomes dominant over spontaneous emission. The [O II] $\lambda\lambda 3727,3730$ transitions have the lowest $n_{e,crit}$ of the lines plotted (see Table 3 for $n_{e,crit}$). Thus, for $n_e \gtrsim 10^3 \text{ cm}^{-3}$, the [O II] $\lambda\lambda 3727,3730$ emission significantly decreases (Juan de Dios & Rodríguez 2021; Méndez-Delgado et al. 2023). On the other hand, the $n_{e,crit}$ of [N II] $\lambda 6585$ is higher (see Table 3) such that the observed [N II] $\lambda 6585/[O\ II]\ \lambda\lambda 3728,3730$ ratio will increase for $10^3 \lesssim n_e \lesssim 10^5 \text{ cm}^{-3}$. At higher densities $(n_e \gtrsim 10^5 \text{ cm}^{-3})$, the [N II] $\lambda 6585/[\text{O II}] \lambda \lambda 3728,3730$ ratio levels out as both the N and O emission decrease at similar rates due to collisional de-excitation. The [N II] $\lambda 6585/[O II] \lambda \lambda 7321,7332$ will decrease slightly at $n_e < 10^7$ cm⁻³, but at even higher densities, $n_e \gtrsim 10^7 \text{ cm}^{-3}$, the ratio will level out due to the [O II] $\lambda\lambda7321,7332$ emission lines reaching their $n_{e,crit}$ and becoming weaker (see Table 3 for $n_{e,crit}$).

The lower left panel of Figure 2 shows similar density sensitivity trends for the emission of the UV N and O lines, but with the turnover to lower emissivities occurring at higher densities $(n_e < 10^6)$. This is because in addition to higher excitation energies, the UV emission lines (N IV] $\lambda\lambda 1483,1487$, O III] $\lambda\lambda 1661,1666$, and N III] $\lambda 1750$) also have higher $n_{e,crit}$. The N IV] $\lambda\lambda 1483,1487$ lines have $n_{e,crit}$ of 1.8×10^5 and 5.6×10^9 cm⁻³, respectively, while the lines in the O III] $\lambda\lambda 1661,1666$ doublet both have an $n_{e,crit}$ of 4.9×10^{10} cm⁻³. As a result, the N IV] $\lambda\lambda 1483,1487/O$ III] $\lambda\lambda 1661,1666$ ratio will be relatively robust to varied n_e (e.g., Zhang et al. 2025). Each of the lines in the N III] $\lambda 1750$ quintuplet has $n_{e,crit} \approx 10^9 - 10^{10} \text{ cm}^{-3}$, which implies little change in the N III] $\lambda 1750/O$ III] $\lambda \lambda 1661,1666$ across a large range in n_e .

In summary, the relatively low-critical densities of optical lines will lead them to collisionally de-excite in extreme environments like those observed at high-z. This highlights the importance of robust physical condition measurements for interpreting emission line strengths, which in turn has significant implications for diagnostic emission line ratios. However, for more details on the physics of nebular emission, see Osterbrock & Ferland (2006) and Draine (2011).

We explore several common diagnostic emission line ratios using the suite of cloudy photoionization models from Section 4. To match the properties of our sample ($< 0.5 Z_{\odot}$), we focus on the models that correspond to $0.05-0.40 Z_{\odot}$. We explore the effects of the n_e , T_e , and ionization structure on the observed emission lines and how they influence the derived nebular properties. Here-

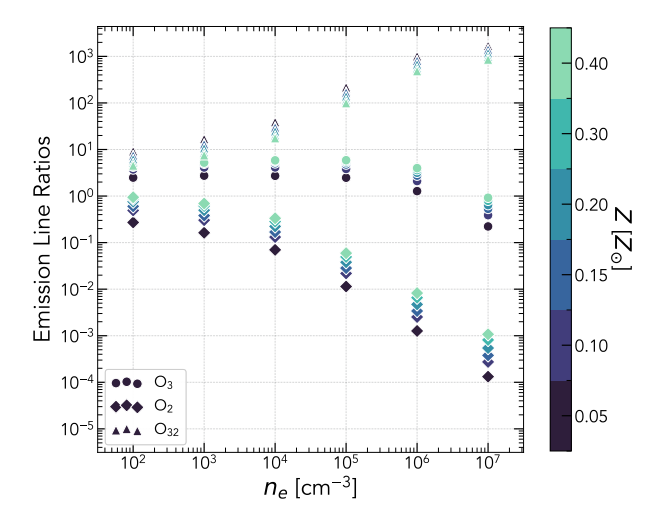


Figure 3. The modeled emission line ratios, O_3 , O_2 , and O_{32} , from Cloudy across $n_e = 10^2 - 10^7$ cm⁻³, the range over which we expect these diagnostics to be sensitive. The circles show O_3 , the diamonds are O_2 , and the triangles describe O_{32} . The colors show different metallicities ranging from $0.05~Z_{\odot}$ and $0.40~Z_{\odot}$ given in the color bar on the right. O_3 and O_2 begin to change rapidly after the $n_{e,crit}$ of [O III] and [O II], respectively, and, as a result, the O_{32} ratio changes drastically at $n_e > 10^3$ cm⁻³.

after, we adopt the following emission line ratio naming convention:

1. O₃: [O III] $\lambda 5008/H\beta \lambda 4863$

2. O_2 : [O II] $\lambda\lambda 3727,3730/H\beta\lambda 4863$

3. O_{32} : [O III] $\lambda 5008/[O II] \lambda \lambda 3727,3730$

4. N₄₃: N IV] $\lambda\lambda 1483,1487/N$ III] $\lambda 1750$

5. Ar₄₃: [Ar IV] $\lambda\lambda 4713,4742/[Ar III] \lambda7138$

6. S_{32} : [S III] $\lambda\lambda 9069,9532/[S II] \lambda\lambda 6717,6731$

7. N2O2: [N II] $\lambda 6585/$ [O II] $\lambda \lambda 3727,3730$

8. N3O3: N III] $\lambda 1750/O$ III] $\lambda \lambda 1661,1666$

9. N4O3: N IV] $\lambda\lambda 1483,1487/O$ III] $\lambda\lambda 1661,1666$

In Figure 3, we examine O_3 , O_2 , and O_{32} as a function of density. For this exercise, we use $10^2 \le n_e \le 10^7$ cm⁻³, which is the range over which the diagnostics we examine are sensitive. The O_3 and O_2 emission line ratios are relatively insensitive to n_e at low- n_e , but begin to change rapidly as they approach their respective $n_{e,crit}$ values (see Table 3 for $n_{e,crit}$). More specifically, O_3 is robust against variations for $n_e \lesssim 10^5$ cm⁻³, while O_2 and O_{32} begin to be severely impacted by densities of $n_e \gtrsim 10^3$ cm⁻³. In the subsequent sections, we examine the effects of increasing density on the derivation of physical gas conditions from these emission lines.

 O_3 and O_2 are commonly used tracers of the gasphase metallicity. Individually, these ratios trace the

ionic O abundances in the high- and low-ionization zones, which are then added together to derive a total O abundance. In the absence of temperature-sensitive line ratios, strong-line calibrations utilizing the sum of O_3 and O_2 are used to determine gas-phase metallicity. Therefore, both direct-method and strong-line calibrations will be impacted by notable effects on these line ratios due to high- n_e .⁶ Significant efforts have been made to calibrate strong-line methods at higherredshifts using samples with low-to-moderate n_e in the low-ionization gas (e.g., Bian et al. 2018; Sanders et al. 2023; Scholte et al. 2025). However, such studies lack density measurements in the high-ionization gas and so cannot not account for collisional de-excitation effects in high-ionization emission lines. O_{32} is also often used as an observational tracer for $\log U$, which was introduced in Section 4, and can be used to parameterize the ionization correction factors (e.g. Berg et al. 2016). Therefore, our ability to accurately account for unseen ionic species will also be impacted by the effects of high- n_e $(n_e > 10^3 \text{ cm}^{-3}) \text{ on O}_{32} \text{ (see Figure 3)}.$

5.2. Electron Temperatures and Densities

Accurate T_e and n_e determinations across their relevant ionization zones are not only important to understand the gas conditions within galaxies, but are also critical for determining the metallicities and relative abundances that shape many galaxy evolution trends. A three-zone ionization model is commonly used to characterize ionized nebular gas, where the low-ionization zone is typically defined by the ionization potential range associated with N^+ (14.5–29.6 eV), the intermediateionization zone defined by the range of S^{+2} (23.3–34.8 eV), and the high-ionization zone traced by the range of O^{+2} (35.1–54.9 eV). In this ionization zone model, each zone has a characteristic electron temperature and density such that $T_{e,low}$, $T_{e,int}$, and $T_{e,high}$ are used to describe the gas temperatures of nebula and $n_{e,low}$, $n_{e,int}$, and $n_{e,high}$ detail the densities of the gas. When temperature is measured for only a single ionization zone, empirical or photoionization model based temperaturetemperature relationships can then be used to estimate the temperatures of the other ionization zones (e.g., Garnett 1992). Note, however, that similar relationships do not exist for connecting the densities.

Figure 4 shows the effects of increasing n_e on three different $T_{e,hiqh}$ -sensitive emission line ratios

⁶ Note that strong-line calibrations are statistical with individual measurements varying as much as ± 0.4 dex between different calibrations (Kewley & Ellison 2008); therefore, applying these calibrations to small samples may lead to severe errors.

([O III] $\lambda 4364/[O III] \lambda 5008$, O III] $\lambda 1666/[O III] \lambda 5008$, and O III] $\lambda 1666/[O III] \lambda 4364$) for a set of Cloudy The $T_{e,high}$ -sensitive line ratios involving models. [O III] $\lambda 5008$ begin to increase very quickly for $n_e \gtrsim 10^5$ cm⁻³, near the critical n_e of [O III] $\lambda 5008$ (see Table 3 for $n_{e,crit}$). Even the most common probe of T_e , [O III] $\lambda 4364/[O III] \lambda 5008$, which has been used in studies of high-z galaxies with JWST, is known to be very sensitive to the n_e of the nebular gas at extreme ionized gas n_e (e.g., Draine 2011; Katz et al. 2023). Figure 4 shows that [O III] $\lambda 4364/[O III] \lambda 5008$ and O III] $\lambda 1666/[O III] \lambda 5008$ are robust for $n_e \lesssim 10^5 \text{ cm}^{-3}$, but will be biased high at higher densities. Alternatively, O III] $\lambda 1666/[O\ III]\ \lambda 4364$ is relatively constant up to $\mathrm{den} \lesssim 10^7 \; \mathrm{cm}^{-3}$ making it an overall more robust tracer of the T_e (although it has a significant dependence on reddening).

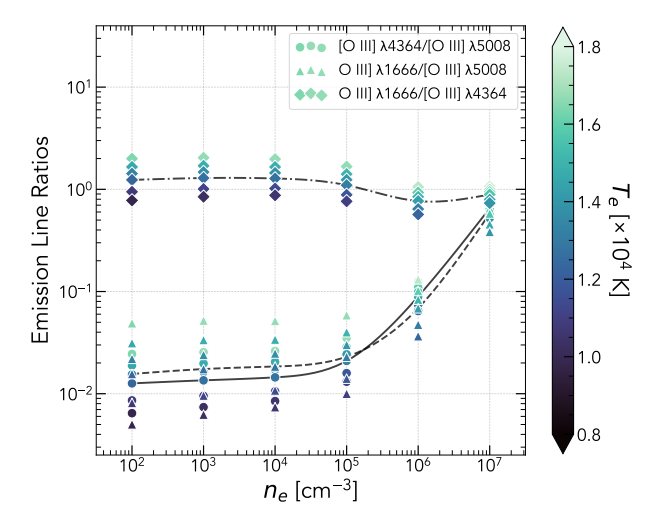


Figure 4. Cloudy models of T_e -sensitive [O III] emission line ratios versus a range of $n_e=10^2-10^7~{\rm cm}^{-3}$. The circle markers are the [O III] $\lambda4364/{\rm [O~III]}~\lambda5008$ ratio, the triangles are O III] $\lambda1666/{\rm [O~III]}~\lambda5008$, and the diamonds are O III] $\lambda1666/{\rm [O~III]}~\lambda4364$. The color bar on the right indicates the T_e in each model. The O III] $\lambda1666/{\rm [O~III]}~\lambda4364$ line ratio is nearly constant over this density range due to the high critical densities of both lines. However, the two ratios involving [O III] $\lambda5008$ both change significantly above $n_e\gtrsim 10^5~{\rm cm}^{-3}$ due to its lower critical density.

5.3. Direct Abundances

Despite the importance of both N and O, significant challenges remain in quantifying robust O/H and N/O abundances across cosmic time. These challenges stem primarily from (1) the lack of uniform O/H and N/O abundance measurement methods in the literature, especially at high redshift, and (2) large uncertainties asso-

ciated with the calculations of important values, including attenuation, electron temperature and density, and ionization correction factors. For instance, no UV N/O abundance studies in galaxies have characterized the T_e , n_e , $\log U$, and ionization correction factors in each ionization zone, which leads to samples of measurements that are simply not analogous. We, therefore, present a uniform method for determining direct O/H and N/O abundances, including the first ionization correction factors for the UV N/O abundance.

Relative ionic abundances are determined as

$$\frac{N(X^i)}{N(\mathrm{H}^+)} = \frac{I_{\lambda_i}}{I_{\mathrm{H}\beta}} \frac{\varepsilon_{\mathrm{H}\beta}}{\varepsilon_{\lambda_i}},\tag{2}$$

where ϵ is the emissivity for ion X^i at the appropriate T_e and n_e , which can be determined using the getEmissivity function in PyNeb. For each ionic abundance, the appropriate physical conditions refers to the T_e and n_e that trace each zone of the three-zone ionization framework. Relative and total abundances are then determined by adding together the relevant ionic species and correcting for any unseen species using an ionization correction factor (ICF). We describe the specifics of this process for O/H and N/O abundances below.

5.4. Oxygen Abundances

We derive O^+/H^+ and O^{+2}/H^+ using the appropriate T_e and n_e . Total O/H abundances in a galaxy are determined by adding all the individual ionic species of O:

$$\frac{O}{H} = \frac{O^0}{H^+} + \frac{O^+}{H^+} + \frac{O^{+2}}{H^+} + \frac{O^{+3}}{H^+}.$$

The relevant ionic fractions are determined as

$$\begin{split} \frac{\mathrm{O}^{+}}{\mathrm{H}^{+}} &= \frac{I_{\lambda\lambda3728,3730}}{I_{\mathrm{H}\beta}} \times \frac{\epsilon_{\mathrm{H}\beta}}{\epsilon_{\lambda\lambda3728,3730}} \\ \frac{\mathrm{O}^{+2}}{\mathrm{H}^{+}} &= \frac{I_{\lambda5008}}{I_{\mathrm{H}\beta}} \times \frac{\epsilon_{\mathrm{H}\beta}}{\epsilon_{\lambda5008}} \\ \mathrm{or} &= \frac{I_{\lambda1666}}{I_{\mathrm{H}\beta}} \times \frac{\epsilon_{\lambda1666}}{\epsilon_{\mathrm{H}\beta}}, \end{split}$$

where O^+ is determined using $T_{e,low}$ and $n_{e,low}$ and O^{+2} is determined using $T_{e,high}$ and $n_{e,high}$.

In the left panel of Figure 5 we plot the ionization fractions of O versus ionization parameter. Note that ${\rm O^{+2}/H^{+}}$ is the dominant species of O for most ionization parameters. At $\log U > -3.0$, we find that the ${\rm O^{0}/H^{+}}$ contribution is small ($\lesssim 10\%$) and ${\rm O^{+3}/H^{+}}$ is negligible across all $\log U$. This is consistent with the findings of Berg et al. (2021), who directly measure [O IV] emission from the UV to conclude that ${\rm O^{+3}}$ only contributes about 1-2% to ${\rm O_{tot}}$ in high-ionization galaxies. Additionally, recent work by Rickards Vaught et al. (2025)

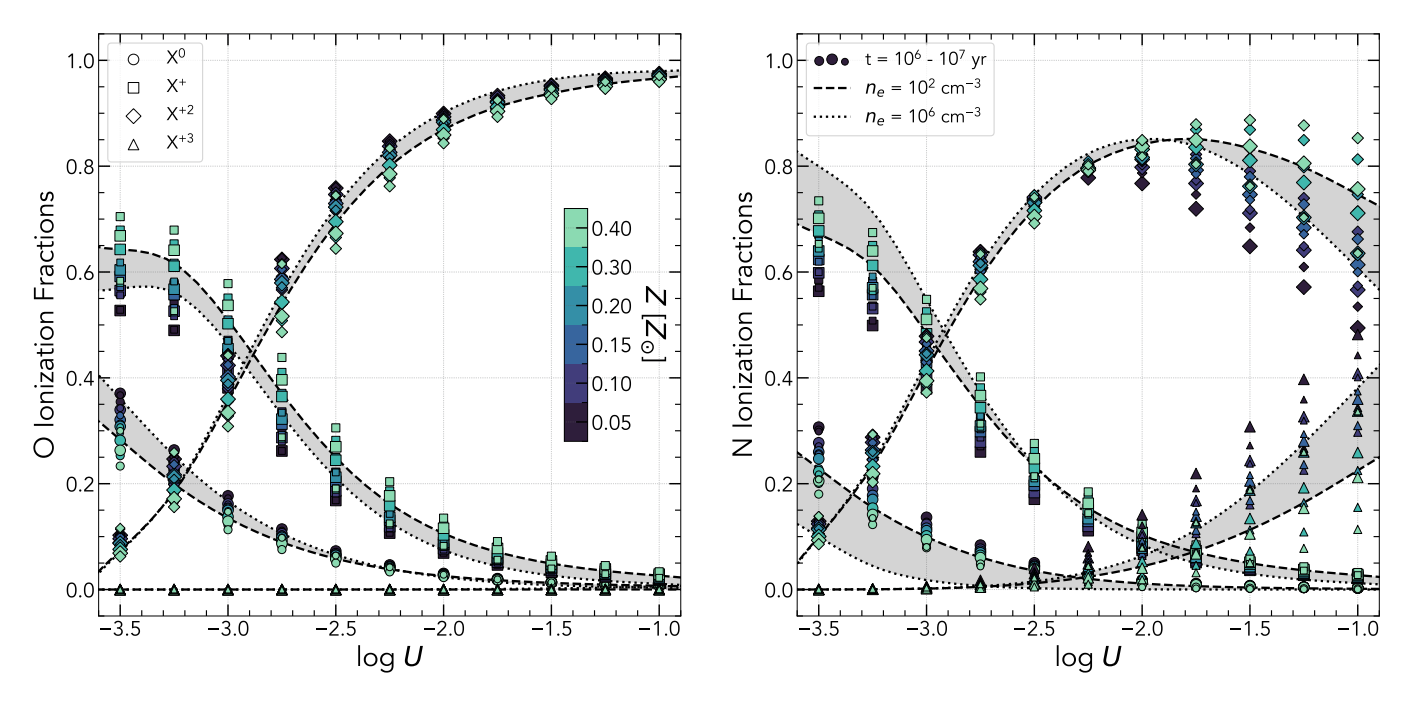


Figure 5. We show the ionization fractions as a function of $\log U$ for both O (left) and N (right). The different marker shapes correspond to the different ionization species, where circles are neutral, squares are singly ionized, diamonds are doubly ionized, and triangles are triply ionized species. The colors differentiate models of varying metallicity from 0.05 Z_{\odot} - 0.40 Z_{\odot} . The marker size represents varying burst ages between $10^{6.0}$ - $10^{7.0}$ yr. Finally, the lines follow a single set of models at burst age of $10^{6.7}$ and metallicity of 0.20 Z_{\odot} . The dashed line distinguishes the model at 10^2 cm⁻³ from the model at 10^6 cm⁻³, which is described by a dotted line.

shows that the use of an ICF to derive a theoretical contribution of ${\rm O}^{+3}/{\rm H}^+$ may be underestimating the contribution from this ion by a factor of 2, but the 2-zone and 3-zone O abundances agree within their uncertainties. Therefore, the total O abundance is calculated from ${\rm O}^+/{\rm H}^+$ and ${\rm O}^{+2}/{\rm H}^+$. Figure 5 also shows that the O ionization fractions are most sensitive to metallicity and burst age, and that each of the ionization fractions are relatively insensitive to n_e , with the most change due to density at $\log U > -3.0$, in ${\rm O}^+/{\rm H}^+$ and ${\rm O}^{+2}/{\rm H}^+$.

In Section 5.2, we discussed the effects of high- n_e on the derived T_{high} , which is crucial to determining accurate total O abundances. Since collisionally-excited line emission from O ions are the dominant cooling mechanism in the ISM at $n_e < 10^7 \text{ cm}^{-3}$, T_e and gas-phase metallicity are negatively correlated in this regime. When assuming the low- n_e limit in gas with higher n_e values, T_e is biased high (see Figure 4), resulting in metallicity determinations that are artificially biased low. For example, T_e measurements of O⁺ and S⁺ have been found to be systematically higher than $T_e(N^+)$ due to the much lower $n_{e,crit}$ of [O II] $\lambda\lambda 3727,3730$ and [S II] $\lambda\lambda 6717,6731$ (Méndez-Delgado et al. 2023; Rickards Vaught et al. 2024). Therefore, it is pertinent

to also exercise caution in using $T_e(O^+)$ or $T_e(S^+)$ as a representative T_e of the low-ionization zone.

5.5. Relative N/O Abundances

The N2O2, N3O3, and N4O3 emission line ratios can be used to probe the relative ionic abundance of N/O. N/O abundances are most commonly derived from low-ionization optical emission using [N II] $\lambda 6585$ and [O II] $\lambda \lambda 3727,3730$, N2O2. However, the increase in JWST detections of the UV N III] $\lambda 1750$ and N IV] $\lambda \lambda 1483,1487$ lines has enabled N/O determinations from the N3O3 and N4O3 ratios. We utilize Cloudy models to investigate the relationship between three different emission line probes of N/O (N2O2, N3O3, N4O3) and the total log(N/O) of the models.

The first panel in Figure 6 shows that there is a monotonic relationship between $\log(N/O)$ and the emission line ratio, N3O3. However, the models show that there is a 0.24 - 0.36 dex spread in N3O3 for a given $\log(N/O)$ that is primarily driven by ionization parameter. Other factors, such as burst age and density have little impact on the emission line ratio at a given $\log(N/O)$.

For N4O3, which is shown in the second panel of Figure 6, there is a similar increasing relationship between the emission line ratio and $\log({\rm N/O})$, but the 1.32 - 1.80 dex spread in models for N4O3 is much larger the spread

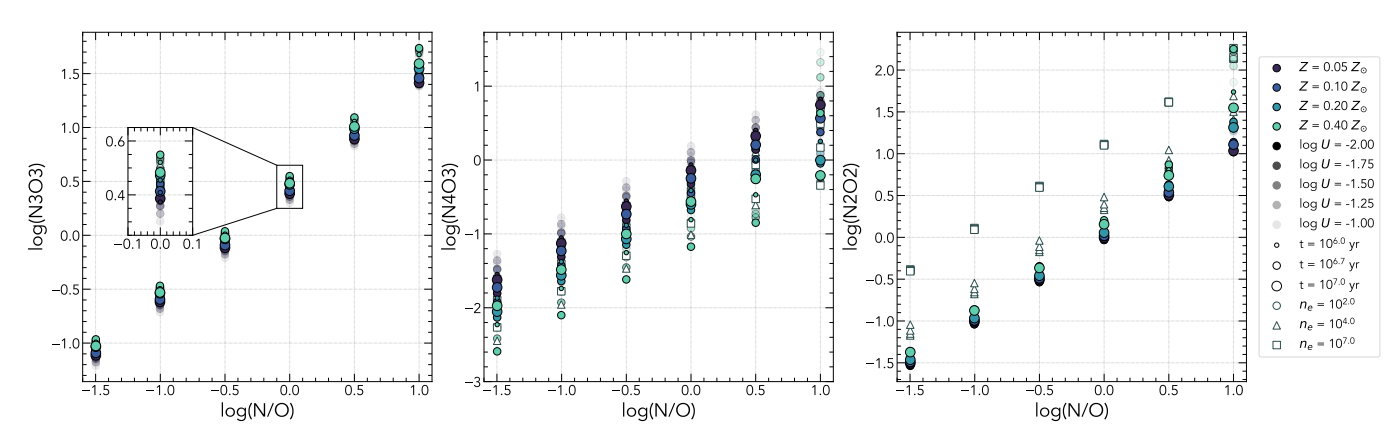


Figure 6. A grid of plots displaying different sets of Cloudy photoionization models at various relative N/O abundances. Every plot contains models that span metallicities from $0.05~\rm Z_{\odot}$ to $0.4~\rm Z_{\odot}$, which correspond to different color models going from darkest (lowest metallicity) to lightest (highest metallicity). Each panel has a different emission line ratio on the y-axis. From left to right, these are N3O3, N4O3, and N2O2. In each of the plots, circles correspond to models at n_e of $10^{2.0}$, triangles are models at $10^{4.0}$, and squares are models at $10^{7.0}$. Additionally, the size of the circle markers corresponds to burst ages between $10^{6.0}$ - $10^{7.0}$. Finally, the spread in models from $\log U$ of -2.0 to -1.0 is indicated by points of decreasing opacity. The N/O tracers each increase monotonically with relative N/O abundance and experience varying degrees of spread at a given N/O due to metallicity, ionization parameter, density, and burst age.

in N3O3. There is a bigger distinction between models of different metallicities for this emission line ratio. At all metallicities shown, burst age, density, and ionization parameter also contribute significantly to the spread in models at varying $\log(N/O)$.

In the final panel of Figure 6, the N2O2 for a given $\log(\text{N/O})$ is severely impacted by high densities. The 1.15-1.24 dex spread in N2O2 at a given $\log(\text{N/O})$ is driven primarily by high densities. This variation is a result of [O II] being suppressed at $n_e \gtrsim 10^3$ (e.g., Rubin 1989; Stasińska 2023). On the other hand, the N2O2 emission line ratio is nearly invariant to burst age, ionization parameter, and metallicity.

All three N/O emission line ratios are sensitive to $\log(N/O)$, however N4O3 and N2O2 are also fairly sensitive to metallicity, ionization parameter, density, and burst age. Between these three emission line ratios, N3O3 is be the most invariant probe of $\log(N/O)$. Given the range in sensitivity of the different N/O emission line ratios, it is important to examine the effects in observed N/O abundances.

The N/O ionic fractions are determined as

$$\begin{split} \frac{\mathrm{N}^{+}}{\mathrm{O}^{+}} &= \frac{I_{\lambda 6585}}{I_{\lambda \lambda 3727,3730}} \times \frac{\epsilon_{\lambda \lambda 3727,3730}}{\epsilon_{\lambda 6585}} \\ \mathrm{or} &= \frac{I_{\lambda 6585}}{I_{\lambda \lambda 7321,7332}} \times \frac{\epsilon_{\lambda \lambda 7321,7332}}{\epsilon_{\lambda 6585}} \\ \frac{\mathrm{N}^{+2}}{\mathrm{O}^{+2}} &= \frac{I_{\lambda 1750}}{I_{\lambda 1666}} \times \frac{\epsilon_{\lambda 1666}}{\epsilon_{\lambda 1750}} \\ \frac{\mathrm{N}^{+3}}{\mathrm{O}^{+3}} &= \frac{I_{\lambda \lambda 1483,1487}}{I_{\lambda 1401}} \times \frac{\epsilon_{\lambda 1401}}{\epsilon_{\lambda \lambda 1483,1487}}, \end{split}$$

where N⁺ is determined using $T_{e,low}$ and $n_{e,low}$, N⁺² is determined using $T_{e,int}$ and $n_{e,int}$, and N⁺³ is determined using $T_{e,high}$ and $n_{e,high}$. When calculating the N⁺²/O⁺² ratio for both the low-z and high-z samples, we consider the measured flux to be a blend of the N III] $\lambda 1750$ complex and therefore use the sum of all 5 emissivities in the quintuplet for our abundances calculations

In general, the relative N/O abundance can be determined directly by adding all of the relevant species together as

$$\frac{N}{O} = \frac{N^+ + N^{+2} + N^{+3}}{O^+ + O^{+2} + O^{+3}}.$$

Since all three species of N and O are almost never observed in the same object, accurate estimates of $\rm N/O$ require an ICF to account for the unseen ionic species such that

$$\frac{N}{O} = \frac{\sum_i N^{+i}}{\sum_j O^{+j}} \times \left[\frac{\sum_i X(N^{+i})}{\sum_j X(O^{+j})} \right]^{-1} = \frac{\sum_i N^{+i}}{\sum_j O^{+j}} \times N \text{ ICF}.$$

 $\sum_i N^{+i}$ and $\sum_j O^{+j}$ are the sum of the observed N and O ionic species, respectively, and ICF is composed of the ionization fractions of N and O, $X(N^{+i})$ and $X(O^{+j})$, respectively. Therefore, we need a robust set of ICFs to enable N/O determinations for different combinations of observed N and O ionic species.

5.5.1. N/O Ionization Correction Factors

To determine N/O abundances, we estimate the ICF as a function of the ionization parameter using our photoionization models. The ${\rm O}_{32}$ ratio is the most commonly used ionization parameter diagnostic since ${\rm O}^+$

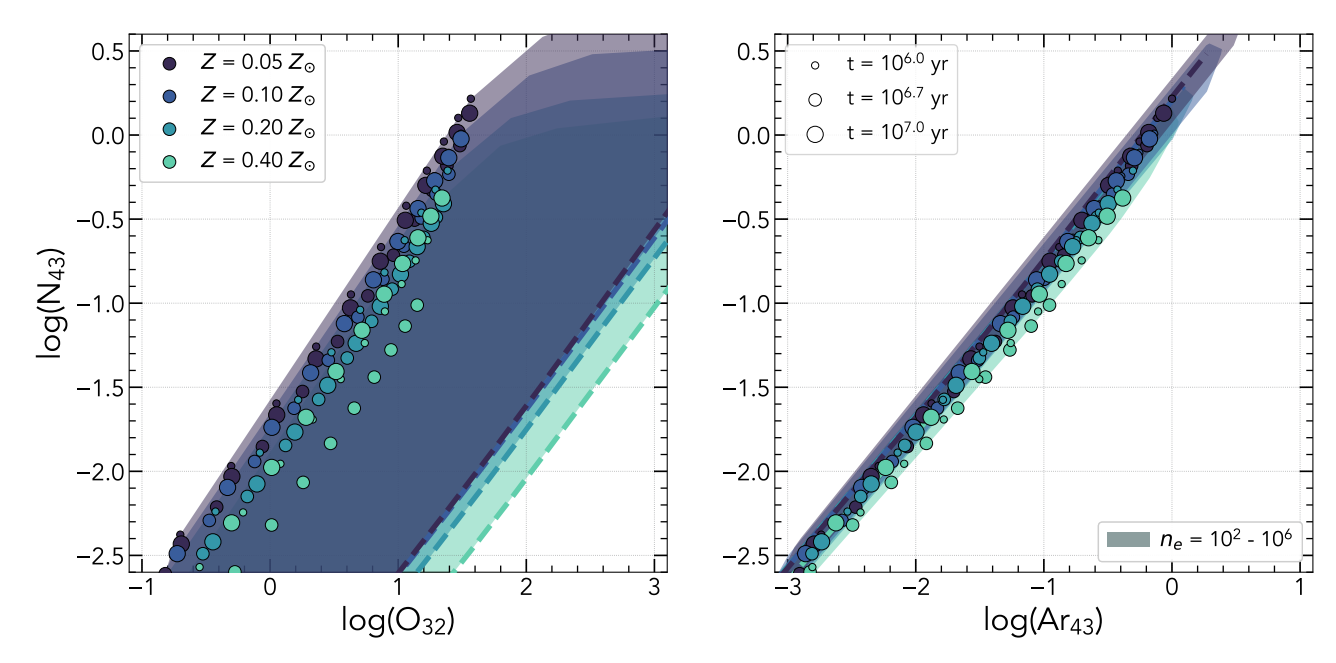


Figure 7. Comparison of different diagnostics of ionization parameter from Cloudy photoionization models (see Section 4). The plots contains models that span metallicities from $0.05 \, \mathrm{Z}_{\odot}$ to $0.4 \, \mathrm{Z}_{\odot}$, as indicated by the color-coding, while the size of the circle markers corresponds to burst ages between $10^{6.0}$ - $10^{7.0}$. The spread in models by varying $n_e = 10^2 - 10^6 \, \mathrm{cm}^{-3}$ is indicated by the shaded regions, where the dashed line represents the maximum $n_e = 10^6 \, \mathrm{cm}^{-3}$ model. Left: The UV $\mathrm{N}_{43} \, \log U_{high}$ diagnostic versus the classic optical $\mathrm{O}_{32} \, \log U_{int}$. diagnostic. The large spread is due to the O_{32} dependence on density, indicating it is a less reliable diagnostic of ionization parameter when the density in the high-ionization zone is unknown. Right: The UV $\mathrm{N}_{43} \, \log U_{high}$ diagnostic versus the optical $\mathrm{Ar}_{43} \, \log U_{high}$ diagnostic introduced by Berg et al. (2021). The tight relationship between N_{43} and Ar_{43} is nearly density independent, suggesting N_{43} can be used as a robust $\log U_{high}$ diagnostic.

and ${\rm O}^{+2}$ cover the standard 3-ionization zones from $\sim 15-55$ eV. However, Berg et al. (2021) showed that for galaxies with very high-ionization emission (> 54 eV), ${\rm O}_{32}$ may not probe high enough energies to properly characterize the gas conditions. In these cases, it is useful to examine multiple probes of the ionization parameter, where ${\rm Ar}_{43}$ can be used to characterize the high-ionization zone ionization parameter (U_{high}) , ${\rm O}_{32}$ can be used to characterize the intermediate-ionization zone ionization parameter (U_{int}) , and ${\rm S}_{32}$ can be used to characterize the low-ionization zone ionization parameter (U_{low}) .

Following Berg et al. (2021), we explore ionization parameters that probe higher ionization energies than O_{32} , for galaxies that have very-high-ionization emission. However, the optical Ar_{43} line ratio is rarely observed at high redshifts. Fortunately, the N_{43} line ratio offers alternative diagnostic power. In the left panel of Figure 7, we plot the optical O_{32} ratio compared to the UV N_{43} ratio for a constant $(N/O)/(N/O)_{\odot} = 0.23$ ($log(N/O) \approx -1.4$, typical of metal-poor galaxies, e.g., Berg et al. 2019). The range in metallicity of the models is indicated by the color-coding, showing a small offset to higher O_{32} with increasing metallicity. Small variations are also seen with changing burst age, as shown by the

increasing point size from $t=10^6-10^7$ Myr. As metallicity increases, the variation due to burst age becomes more noticeable. There is, however, a large spread in the models caused by varying n_e , which is shown by the shaded regions extending from filled circles with $n_e=10^2$ cm⁻³ to the dashed lines marking $n_e=10^6$ cm⁻³. As discussed in Section 5.1, this n_e -effect on the ${\rm O}_{32}$ line ratio is due to the $n_{e,crit}$ of ${\rm O}^+$ at $n_e\gtrsim 10^3$ and ${\rm O}^{+2}$ at $n_e\gtrsim 10^5$, suggesting it is less effective as an ionization parameter diagnostic when density is unknown.

In the right panel of Figure 7, we plot the UV N_{43} ratio compared to the optical Ar_{43} high-ionization zone ionization parameter diagnostic. Here, N_{43} is sensitive to the high and very-high ionization zones probed by N^{+2} (29.6–47.4 eV) and N^{+3} (47.4–77.5 eV), respectively, similar to the Ar^{+2} (27.6–40.7 eV) and Ar^{+3} (40.7–59.8 eV) ionization potentials. In general, we find a tight trend between N_{43} and Ar_{43} that is nearly independent of density. Overall, this analysis suggests that the UV N_{43} ratio is consistent with optical probes of $\log U_{high}$ and can, therefore, be used as an alternative diagnostic of $\log U_{high}$ when these lines are available. On the other hand, the discrepancy between $\log U_{high}$ and $\log U_{int}$ measured with N_{43} and O_{32} , respectively,

is related to n_e . This dependency renders O_{32} unreliable when the high-ionization zone density is $> 10^3$.

Given the strong n_e -sensitivity of the ${\rm O}_{32}$ ratio, we present new $\log U$ diagnostics that account for this effect. Adopting the 4-zone ionization model presented in Berg et al. (2021), we examine the ${\rm O}_{32}-\log U_{int}$ and ${\rm N}_{43}-\log U_{high}$ relationships from the Cloudy photoionization model grid (presented in Section 4) in Figure 8. The left column shows the color-coded 3-dimensional surfaces probing the dependence of $\log U$ on emission line ratio, metallicity, and density, while the right column shows a 2-dimensional projection along the metallicity axis. The 2-dimensional plot of ${\rm O}_{32}$ (upper), shows the significant sensitivity to density, while little spread is seen for ${\rm N}_{43}$ (lower).

To characterize the trends in Figure 8, we fit bicubic surfaces to the $O_{32} - \log U_{int}$ and $N_{43} - \log U_{high}$ relationships using the scipy.optimize.least_squares function in python. The resulting fit, f(x,y), is a bicubic surface with the form: $f(x,y) = \log U = A + Bx +$ $Cy+Dxy+Ex^2+Fy^2+Gxy^2+Hyx^2+Ix^3+Jy^3$, where $y = Z/Z_{\odot}$ (metallicity) and $x = \log O_{32}$ or $x = \log N_{43}$. The coefficients that describe these bicubic surface are reported in Table 4. The ranges of validity for these relationships are $0.05 \le Z/Z_{\odot} \le 0.4$, $-1.0 \le \log O_{32} \le 2.5$, and $-3.0 \le \log N_{43} \le 0.5$. Note that the densityinsensitivity of the N₄₃ diagnostic suggests that it can be robustly used even in the absence of a measurement of the high-ionization zone density. Therefore, we recommend using the N₄₃ diagnostic of ionization parameter over O_{32} when the requisite lines are available. For another n_e -insensitive probe of $\log U$ that instead utilizes O⁺²/O⁺, which may be useful in studies where N IV and N III are not present, see Appendix C.

We determine five ICFs for each of the following ionic abundance ratios:

$$\begin{split} &1. \ \frac{N}{O} = \frac{N^{+}}{O^{+}} \times ICF(N^{+}/O^{+}) \\ &2. \ \frac{N}{O} = \frac{N^{+2}}{O^{+2}} \times ICF(N^{+2}/O^{+2}) \\ &3. \ \frac{N}{O} = \frac{N^{+3}}{O^{+2}} \times ICF(N^{+3}/O^{+2}) \\ &4. \ \frac{N}{O} = \frac{N^{+} + N^{+2}}{O^{+} + O^{+2}} \times ICF((N^{+} + N^{+2})/(O^{+} + O^{+2})) \\ &5. \ \frac{N}{O} = \frac{N^{+2} + N^{+3}}{O^{+2}} \times ICF((N^{+2} + N^{+3})/O^{+2}), \end{split}$$

where O⁺ is determined from [O II] $\lambda\lambda 3727,3729$, O⁺² is determined from O III] $\lambda 1666$, N⁺ is determined from [N II] $\lambda 6585$, N⁺² is determined from N III] $\lambda 1750$, and N⁺³ is determined from N IV] $\lambda\lambda 1483,1487$. Note that

Table 4. Ionization Parameter Fits

| | | | $n_e \text{ (cm}^{-3}\text{)}$ | | |
|-------------------|------------------|-----------------------|--------------------------------|------------|-----------|
| | 10^{2} | 10^{3} | 10^{4} | 10^{5} | 10^{6} |
| z = f(| $(x,y) = \log U$ | $J_{int}; x = \log t$ | $g(O_{32}); y =$ | Z | |
| $A \dots$ | -3.00199 | -3.06316 | -3.28872 | -3.71434 | -4.08448 |
| $B \dots$ | 0.61875 | 0.65186 | 0.62685 | 0.53053 | 0.54480 |
| $C \dots$ | 0.41277 | 0.45934 | 0.32662 | 0.07827 | 0.17599 |
| $D \dots$ | 0.96910 | 0.60495 | 0.44956 | 0.16911 | -0.23221 |
| $E \dots$ | 0.11489 | 0.04757 | 0.05904 | 0.05866 | 0.01351 |
| F | 2.10518 | 1.34596 | 1.19054 | 1.65578 | 2.15922 |
| $G \dots$ | -0.88265 | -0.61689 | -0.61832 | -0.62173 | -0.47220 |
| $H \dots$ | 0.55524 | 0.25114 | 0.19987 | 0.18713 | 0.19535 |
| I | 0.18323 | 0.04025 | 0.00771 | 0.00364 | 0.00841 |
| $J \dots$ | -4.65728 | -3.24251 | -2.62744 | -2.54602 | -2.95869 |
| $\sigma_{ m rms}$ | 0.02 | 0.01 | 0.01 | 0.01 | 0.01 |
| z = f(| $(x,y) = \log U$ | $J_{high}; x = 1$ | $og(N_{43}); y =$ | = <i>Z</i> | |
| $A \dots$ | -1.29754 | -1.61212 | -1.66787 | -1.6783 | -1.6839 |
| $B \dots$ | 1.60610 | 1.03768 | 0.91085 | 0.89072 | 0.88034 |
| $C \dots$ | 4.10271 | 2.59196 | 2.2672 | 2.20159 | 1.93562 |
| $D \dots$ | 3.82481 | 2.04872 | 1.63593 | 1.56124 | 1.55433 |
| $E \dots$ | 0.52310 | 0.18279 | 0.09245 | 0.08156 | 0.08954 |
| F | 12.37774 | 9.37845 | 8.61368 | 8.23949 | 8.03766 |
| $G \dots$ | 0.22144 | -0.27803 | -0.45877 | -0.55776 | -0.43756 |
| $H \dots$ | 0.74401 | 0.32021 | 0.20331 | 0.17851 | 0.22411 |
| I | 0.09083 | 0.02670 | 0.00723 | 0.00484 | 0.00874 |
| $J \dots$ | -17.63486 | -15.11384 | -14.59398 | -14.35798 | -13.90218 |
| $\sigma_{ m rms}$ | 0.04 | 0.03 | 0.03 | 0.03 | 0.03 |

Note—The bicubic surface fit to Cloudy photoionization models for the ionization parameters are parameterized by the following equation: $z = f(x,y) = A + Bx + Cy + Dxy + Ex^2 + Fy^2 + Gxy^2 + Hyx^2 + Ix^3 + Jy^3$.

ICF 4, $(N^+ + N^{+2})/(O^+ + O^{+2})$, combines low ionization and intermediate to high ionization lines that should more accurately represent relative N/O. Additionally, ICF 1 may also be used to in combination with the near-UV [O II] $\lambda 2470^7$ and N II] $\lambda \lambda 2139,2143$ emission lines.

Similar to the $\log U$ fits, we fit bicubic surfaces for each set of n_e grids from 10^2-10^6 cm⁻³. However, the ICFs are more sensitive to burst age than the ionization parameters, so we weight the fit by the spread in burst ages between the models at a given $\log U$. The coefficients for these fits can be found in Table 5. We note that the ICF fits presented in this work are only valid for $-3.5 < \log(U) < -1.0$. Figure 9 shows the five ICFs considered in this work versus ionization parameter. Each ICF is shown for six different metallicities.

 $^{^7}$ [O II], in the near-UV, is a doublet composed of emission lines at $\lambda 2470.22$ and $\lambda 2470.34,$ which would be unresolved in galaxy spectroscopy.

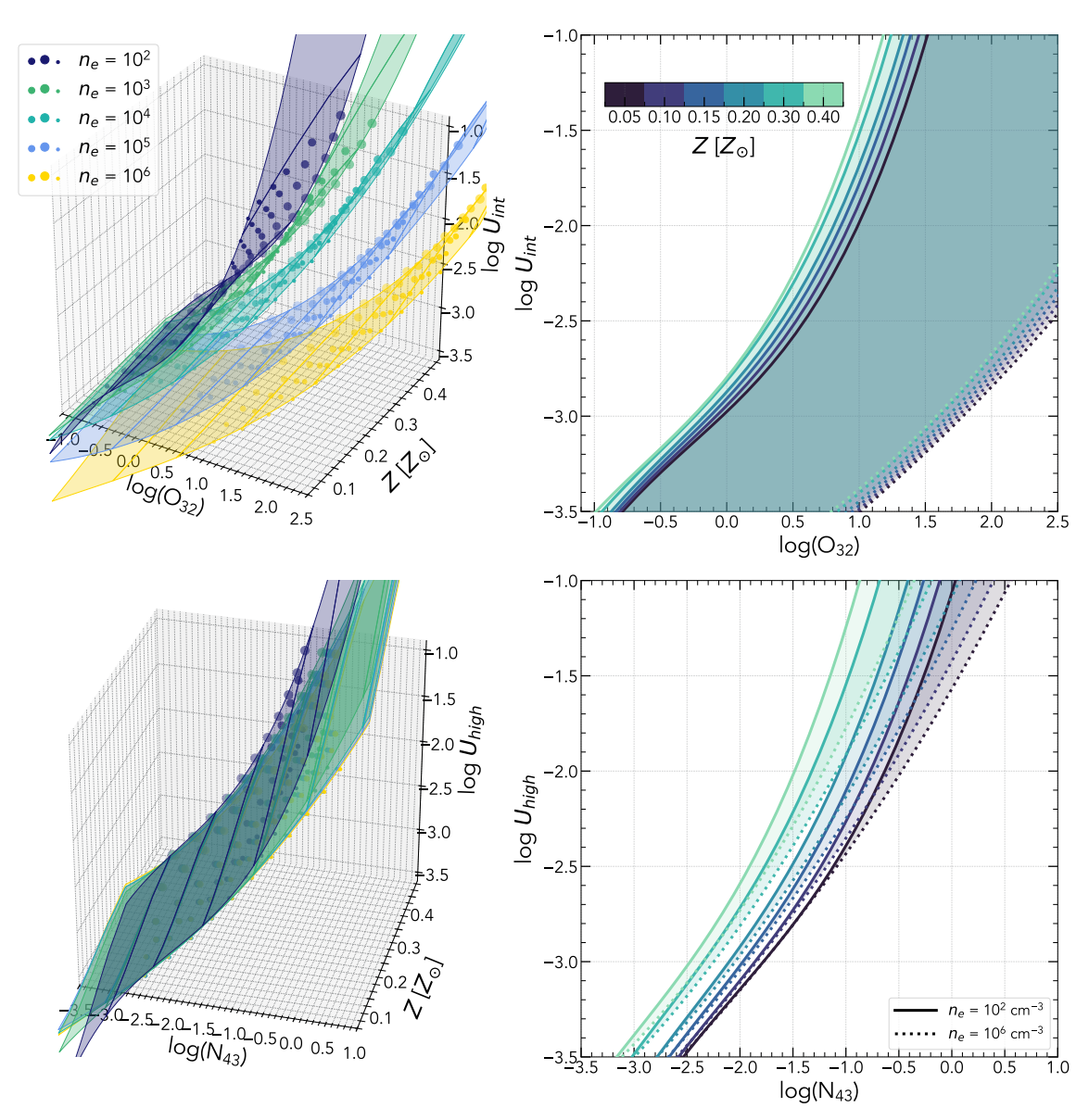


Figure 8. The cloudy model relationship between both O_{32} (upper) and N_{43} (lower) and ionization parameter, U. The left column shows 3D plots of the bicubic fits for each grid of models. Marker color corresponds to n_e ranging from 10^2 - 10^6 cm⁻³. In the right column, we show a 2D projection where the range of n_e is shown by the shaded region. The metallicities range between $0.05 \ Z_{\odot}$ and $0.40 \ Z_{\odot}$ as indicated by the color bar in the upper right plot. Clearly, n_e has a large impact on O_{32} , however, N_{43} is much more robust to extreme n_e .

The first column in Figure 9 gives each model ICF as a function of $\log U$ at $n_e=10^2~{\rm cm}^{-3}$. In this low-density limit of the N⁺/O⁺ ICF, we find that a relatively small correction is needed (< 10%) across a large range of $\log U$, which is consistent with the convention that N/O \approx N⁺/O⁺ (e.g. Peimbert & Costero 1969; Nava et al. 2006; Amayo et al. 2021). The N⁺²/O⁺² ratio will overestimate N/O by < 50% at low $\log U$, and underestimate N/O by up to 200% at high $\log U$. While the N⁺³/O⁺² ratio underestimates N/O between 100 - 15000% across a variety of $\log U$, the relative (N⁺ +

 N^{+2})/(O⁺ + O⁺²) ionic abundance will underestimate N/O ($\sim 150\%$) at high $\log U$ and overestimate N/O (< 10%) at low $\log U$. Finally, the $(N^{+2} + N^{+3})/O^{+2}$ ICF indicates that this relative ionic abundance will overestimate the relative N/O abundance by as much as 30%, however, at higher $\log U$ correction required will be much smaller.

The fifth column in Figure 9 again gives each ICF as a function of $\log U$, however, the $n_e = 10^6$ cm⁻³. The N⁺/O⁺ will overestimate the relative N/O by nearly 40% at the lowest metallicities and $\log U$. For

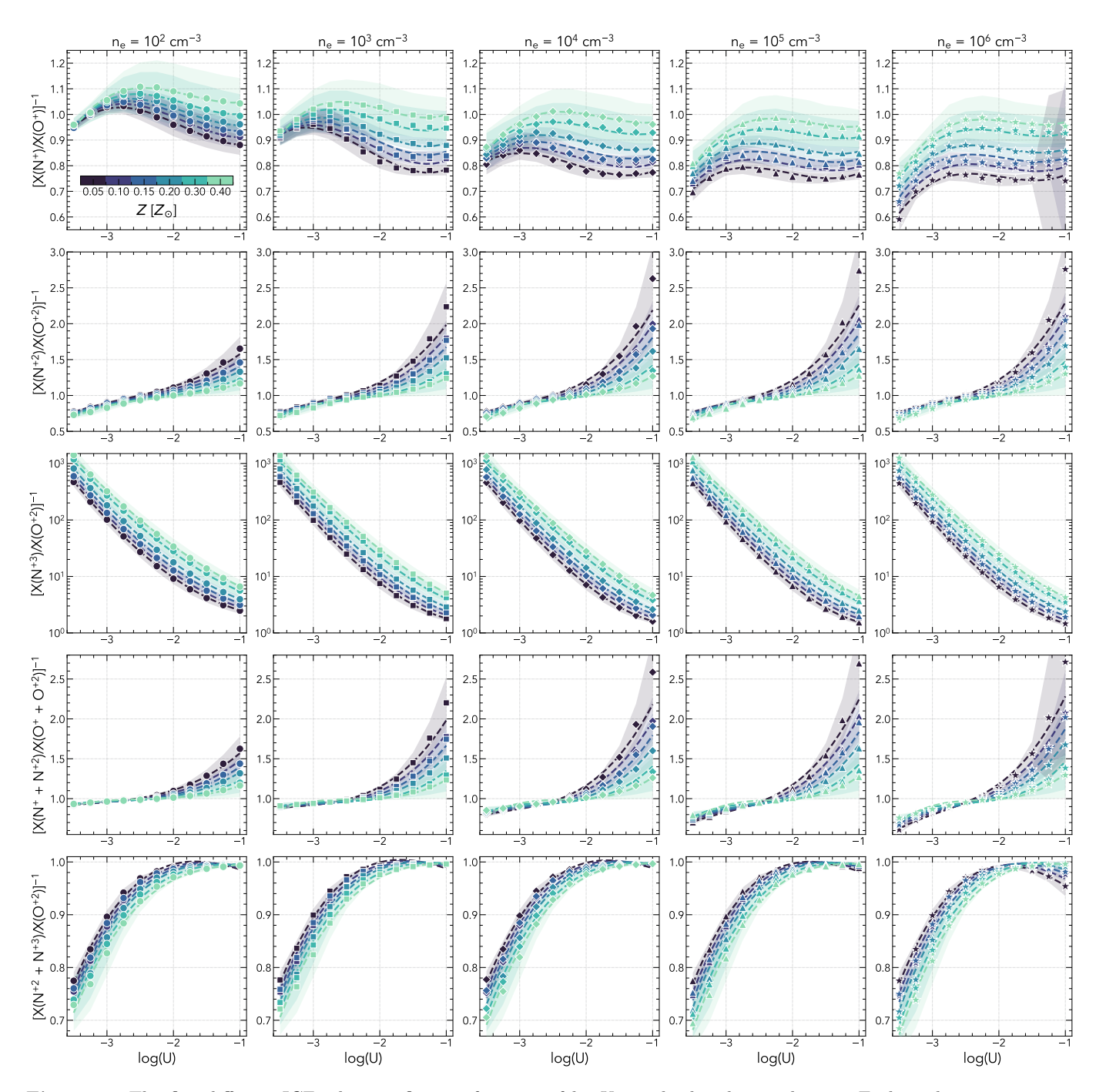


Figure 9. The five different ICFs that we fit as a function of $\log U$ are displayed in each row. Each is shown at a range of metallicities between $0.05~Z_{\odot}$ and $0.40~Z_{\odot}$ indicated by the color bar in the upper leftmost tile. The shaded region that corresponds to a spread in burst age $(t = 10^{6.0} - 10^{7.0} \text{ Myr})$. Every column corresponds to a different constant from $n_e = 10^2 - 10^6$. Row 1: N^+/O^+ is a fairly good estimate of relative N/O. Row 2: N^{+2}/O^{+2} shows that this ionic abundance is overestimating N/O at low ionization parameter and underestimating it at high ionization parameter. Row 3: N^{+3}/O^{+2} is underestimating N/O across the entire range of ionization parameters we consider, but most notably so at low ionization. Row 4: The $(N^+ + N^{+2})/(O^+ + O^{+2})$ ICF is underestimating relative N/O at all ionization parameters, but this is most severe at high ionization. Row 5: Finally, the $(N^{+2} + N^{+3})/O^{+2}$ seems to infer relative N/O very well at $\log(U) > -2.75$.

the N⁺²/O⁺² ratio, N/O is overestimated by < 50% at low log U, and underestimated by up to 300% at high log U. On the other hand, the N⁺³/O⁺² ratio underestimates relative N/O between 100 - 15000% over all log U. The relative (N⁺ + N⁺²)/(O⁺ + O⁺²) ionic abundance will underestimate N/O (\sim 250%) at high log U and overestimate N/O (< 50%) at low log U. The (N⁺² + N⁺³)/O⁺² ICF reveals that this relative ionic abundance will overestimate the relative N/O abundance by < 30%; however, at log U > -2.0 the correction will be closer to > 5%.

When considering the effects of n_e , N^+/O^+ goes from being within 10% of the total N/O to overestimating the N/O by up to 40% for some $\log U$ and metallicities at the highest n_e . From low- to high- n_e , N^{+2}/O^{+2} maintains its shape but goes from being within $\sim 50\%$ of the total N/O to under-estimating the N/O by up to 300% at high $\log U$ and low metallicity. While across the same range of n_e , N^{+3}/O^{+2} maintains consistency in that it underestimates total N/O by as much 100 - 15000% and continues underestimating the total N/O by roughly the same amount. On the other hand, the $(N^+ + N^{+2})/(O^+ + O^{+2})$ and $(N^{+2} + N^{+3})/O^{+2}$ ICFs do not change significantly with n_e .

5.6. Summary of Density Effects and Recommendations

In the previous sections, we discussed the impact of high- n_e on emission line ratios, physical conditions, ICFs, and total O/H abundances. High values of density $(10^2 \le n_e \le 10^7)$ will have the most effect on relative N/O abundances via biases that trickle down throughout the process of deriving N/O. When tracing N/O with the optical tracer, N2O2, the extreme sensitivity to n_e discussed in Section 5.1 will make this emission line ratio less representative of the relative N/O. However, the UV tracers, N3O3 and N4O3, are relatively insensitive to n_e , but dramatically dependent on the T_e as demonstrated in Figure 2. This becomes important when considering that deriving T_e from [O III] $\lambda 4364/\lambda 5008$ in high- n_e gas will bias T_e high. This derived T_e will impact the O/H and, as a result, influence the ICFs, which have a secondary dependence on metallicity. The ICFs can also be significantly influenced by n_e effects on the O_{32} ratio, which is classically used to diagnose the $\log U$ (see Sections 5.1 and 5.5.1).

To demonstrate the cumulative impact of density effects on derived nebular properties we explore the following three simple cases: (1) assuming a low density in a high density environment, (2) a multi-phase ISM in which low-ionization gas is uniform low-density and

Table 5. Ionization Correction Factor Fits

| 1 | lable 5. I | onization | Correction | on Factor | Fits |
|-----------------------------------|---------------------------|--------------------|-----------------------|--------------------|--------------------|
| | | | $n_e (cm^{-3})$ | | |
| | 10^{2} | 10^{3} | 10^{4} | 10^{5} | 10^{6} |
| z = f(| $(x,y) = N^+$ | $/O^+$ ICF; | x = log(U) | ; y = Z | |
| $A \dots$ | | | 1.04256 | 1.05359 | |
| $B \dots$ | 0.35805 | | 0.52349 | 0.54522 | |
| $C \dots$ | 0.73829 | 0.57962 | 0.14444 | 0.02129 | |
| $D \dots$ | -0.00147 | -0.20911 | | -0.52622 | |
| $E \dots$ | 0.25599 | 0.37927 | | 0.28401 | 0.31784 |
| $F \dots$ | | 0.13139 | | 1.11581 | 1.111112 |
| $G \dots$ | | -0.14117 | 0.00501 | 0.18414 | 0.20679 |
| $H \dots$ $I \dots$ | -0.04340 0.04517 | -0.11589 0.05690 | -0.15029 0.04052 | -0.12303 0.04511 | -0.06881 0.05389 |
| $J \dots$ | | -1.00523 | | -1.75450 | |
| $\frac{\sigma}{\sigma_{\rm rms}}$ | 0.01 | 0.01 | 0.01 | 0.01 | 0.02 |
| | $(x,y) = N^+$ | | | | |
| $\frac{z-f}{A}$ | | 4.18005 | | 5.20832 | 5.32595 |
| | 1.40827 | | | | 3.82306 |
| $C \dots$ | | -7.42258 | | | -9.73777 |
| $D \dots$ | | -4.08756 | | -5.59671 | |
| | 0.41454 | | | 1.12023 | |
| $F \dots$ | 2.86050 | 5.91850 | 7.28429 | 7.46491 | 6.66459 |
| G | 0.89889 | 1.77628 | 2.22999 | 2.33000 | 2.20890 |
| H | -0.26525 | -0.56759 | -0.74483 | -0.79911 | -0.82169 |
| I | 0.04878 | 0.08888 | 0.11297 | 0.12032 | 0.12301 |
| $J \dots$ | 0.13269 | -0.43755 | -0.42475 | -0.22878 | 0.41586 |
| $\sigma_{ m rms}$ | 0.02 | 0.03 | 0.04 | 0.04 | 0.04 |
| z = f(| $(x,y) = \log$ | (N^{+3}/O^{+2}) | $ICF)^{\dagger}; x =$ | =log(U); y = | =Z |
| $A \dots$ | 0.33721 | 0.32989 | 0.27897 | 0.27431 0.58497 | 0.24361 |
| $B \dots$ | | | | | |
| $C \dots$ | | -0.68007 | | -0.51353 | |
| $D \dots$ | -1.33811 | -1.56364 | | -1.53730 | |
| $E \dots F \dots$ | 0.27971 | 0.45572 | | 0.49791 | 0.50260 |
| $G \dots$ | 5.83889 0.31924 | 5.36918 0.52243 | 5.11709 0.54710 | 4.79966 | |
| $H \dots$ | -0.26487 | -0.30772 | _0.34710 | 0.52024 -0.31010 | _0.30233 |
| <i>I</i> | 0.00662 | 0.03347 | 0.03900 | 0.04044 | 0.04061 |
| $J \dots$ | | | -7.62178 | | -6.28983 |
| $\sigma_{ m rms}$ | 0.03 | 0.03 | 0.03 | 0.03 | 0.03 |
| | $(x,y) = \frac{N^+}{O^+}$ | $+N^{+2}$ ICF | x = log(U) | y = Z | |
| $\frac{A}{A}$ | | | | 5.23403 | 5 38100 |
| $B \dots$ | | | 3.50850 | | |
| $C \dots$ | | | | -10.16471 | |
| $D \dots$ | | -4.44062 | | -5.67998 | |
| $E \dots$ | 0.42943 | 0.81553 | 1.01895 | 1.11019 | |
| $F \dots$ | 3.55046 | 6.75686 | 8.30719 | 8.65627 | |
| $G \dots$ | 1.09105 | 2.04896 | 2.52596 | 2.76166 | 2.83279 |
| H | -0.29179 | -0.59753 | -0.74177 | -0.73561 | -0.67993 |
| I | 0.04290 | 0.08034 | 0.10332 | 0.11846 | 0.13442 |
| $J \dots$ | -0.39350 | -0.97013 | -1.20540 | -0.92040 | -0.33026 |
| $\sigma_{ m rms}$ | 0.01 | 0.02 | 0.03 | 0.04 | 0.04 |
| z = f(| $(x,y) = (N^{-1})$ | $+^{2} + N^{+3}$ | $/O^{+2}$ ICF; | x=log(U) | y = Z |
| $A \dots$ | 0.93486 | 0.93562 | 0.94769 | 0.93356 | 0.84213 |
| $B \dots$ | | -0.03369 | | -0.01832 | |
| $C \dots$ | 0.28011 | 0.27477 | 0.25282 | 0.32434 | 0.67947 |
| $D \dots$ | 0.24291 | 0.22211 | 0.16544 | 0.17688 | 0.32963 |
| $E \dots$ | 0.02786 | 0.02993 | 0.03802 | 0.04019 | 0.02188 |
| $F \dots$ | | -0.18937 | | -0.47628 | |
| $G \dots H \dots$ | | -0.14771 | -0.14786 | | -0.29574 |
| H | 0.02356 0.01429 | 0.01550 0.01478 | -0.00045 0.01579 | -0.00391 0.01642 | 0.00886 0.01486 |
| $J \dots$ | | -0.12369 | 0.01379 | 0.01042 0.18150 | 0.01480 0.42906 |
| $\sigma_{\rm rms}$ | 0.10010 | 0.01 | 0.04501 | 0.13130 | 0.42300 |
| - rms | U.U.1 | U.U.I | U.U.1 | U.U.1 | U.U. |

Note— The bicubic surface fits to Cloudy photoionization models for the ICFs are parameterized by the following equation: $f(x,y) = A + Bx + Cy + Dxy + Ex^2 + Fy^2 + Gxy^2 + Hyx^2 + Ix^3 + Jy^3$.

 † Note that the fit for the N⁺³/O⁺² ICF returns the logarithm of the ICF.

high-ionization gas is uniform high-density, and (3) a multi-phase ISM in which a given ionization zone of gas is a mix of low- and high-density gas.

5.6.1. Assuming Low Densities in a High-Density Environment

We first determine the level of bias introduced in nebular properties if the density is underestimated. For example, if we adopt a $n_e = 10^5 \text{ cm}^{-3}$ nebular model, but assume a density of 10^2 cm⁻³, the T_e determined from [O III] $\lambda 4364/\lambda 5008$ will be overestimated by, on average, 1800 K. In the lowest Z models the T_e derived from [O III] $\lambda 4364/\lambda 5008$ is overestimated by approximately 1300 K, while this bias is closer to 2300 K in the highest Z models. This T_e bias results in the O^{+2}/H^+ relative abundance and, thus, the direct gas-phase metallicity being underestimated by roughly 0.67 dex. The O⁺/H⁺ is also affected by the T_e bias, where $T_e(\mathcal{O}^+)$ is determined from the $T_e(O^{+2})$ with a T_e - T_e relationship, but this has smaller overall effect on O/H due to the lower density of this gas and the smaller ion fraction. These assumptions also lead to a overestimation of log(N/O) using N^{+2}/O^{+2} of ~ 0.16 dex. The resulting bias from this exercise, while moderate for log(N/O), has larger ramifications on the N/O-O/H plane and our interpretations of chemical enrichment in dense, high-z galaxies. This underestimation is not limited to the case of making model assumptions when lacking density measurements; in practice, many standard optical density diagnostics intrinsically lose sensitivity and saturate above their critical densities, biasing observationally-inferred densities to lower values whenever dense clumps dominate the emission measure. We will discuss the implications of these findings in Section 6 for a sample of UV N emitting galaxies from $0 \lesssim z \lesssim 11$.

Given the potentially significant effects of high n_e , we recommend that future UV N/O abundance studies adopt the following approach. (1) Measure multiphase n_e , when possible, to fully characterize the n_e in each ionization zone. (2) Use the appropriate density to determine the temperature of a given ionization zone, e.g., calculate $T_{e,high}(n_{e,high})$. In the absence of T_e -sensitive emission line ratios for the lowor intermediate-ionization zones, adopt the appropriate T_e for each zone using a T_e - T_e relationship (Garnett 1992; Pilyugin et al. 2009; Croxall et al. 2016; Arellano-Córdova & Rodríguez 2020; Rogers et al. 2021). (3) Calculate O⁺/H⁺ and O⁺²/H⁺ using the appropriate low- and high-ionization T_e and n_e , and determine the gas-phase metallicity directly from these total ionic abundances. (4) Derive relative ionic N/O abundances (e.g., N^+/O^+ , N^{+2}/O^{+2} , N^{+3}/O^{+2}) using the correct T_e and n_e for each ion. (5) Determine $\log U$ using a n_e -insensitive diagnostic such as N₄₃ or Ar₄₃. If N₄₃ and Ar₄₃ are unavailable, use the O₃₂ diagnostic with the measured $n_{e,high}$ or use the O⁺²/O⁺ diagnostic; the latter should be used when $n_{e,high}$ is also unavailable. (6) Finally, determine the total N/O abundance using the appropriate log U, O/H abundance, and density to determine the ICFs and apply these corrections to account for unseen ionic species. This empirically-motivated multi-phase ionization model fully accounts for the T_e and n_e structure of the ionized gas in galaxies.

Finally, we emphasize that the recommendation outlined above is assuming the source of ionization is purely from stellar populations. Assuming ionization from stellar populations, the extreme emission we are examining in this work can only be produced by very young stellar populations (Jaskot & Ravindranath 2016). Note that these young ages are consistent with the stellar population ages from the UV continuum in the CLASSY galaxies (Parker et al. 2025). However, different ionizing sources may be contributing to the high-ionization conditions and gas n_e in galaxies with extreme emission lines. It may be that the light from objects with strong N IV] emission is being dominated by AGN, but determining the source of ionizing radiation in our sample is topic of future work.

5.6.2. A Multi-phase ISM with Uniform Low-Density Low-Ionization Gas and High-Density High-Ionization Gas

In Section 5, we discussed nebular models using a uniform n_e framework. To better align our interpretation with observations, we explore the Cloudy models using a multi-phase n_e model. There is physical evidence that gas near a SF region is higher density (e.g., Berg et al. 2021), often referred to as a dense core, we attempt to model this as simply as possible, where we use linear combinations of our existing Cloudy models as a first order approximation of dense cores. We create linear combinations of models where low- n_e ($10^2 {\rm cm}^{-3}$) and high- n_e ($10^5 {\rm cm}^{-3}$) contribute varying percentages of the total emission.

In Figure 10, we plot O_3 , O_2 , and O_{32} emission line ratios where the [O III] arises only from the high- n_e core and [O II] emits only from the low- n_e regions of the nebula. We find that the O_3 ratio is dominated by the high- n_e gas and remains relatively constant with increasing high- n_e core contribution. The O_2 begins to decrease rapidly with increasing H emission from the high- n_e region of gas. This is because the integrated O_2 line ratio will only have [O II] emission from the low- n_e gas, but H emission from both the low- n_e and high- n_e gas. Since emission will increase as n_e^2 , the denominator of

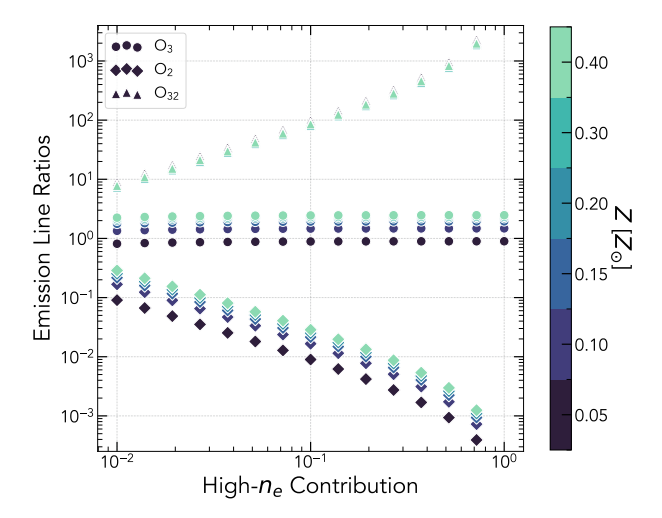


Figure 10. Cloudy models are able to reproduce extreme emission line ratios of O_3 , O_2 , and O_{32} (y-axis) given varied contributions of emission from low- and high- n_e gas (x-axis). The circles show O_3 , the diamonds are O_2 , and the triangles describe O_{32} . The colors show different metallicities ranging from $0.05~Z_{\odot}$ and $0.40~Z_{\odot}$ given in the color bar on the right.

the O_2 fraction will quickly become dominated by H emission from the high- n_e region as the core fraction increases. The O_{32} models are able to reproduce even the most extreme observed ratios at relatively low ($\sim 0.01\%$) contributions from high- n_e gas. We note that this multiphase- n_e nebula model is not expected to impact the N/O emission line ratios since they mostly come from the same ionization zones. This exercise demonstrates how easily high- n_e gas can dominate the emission in a multiphase- n_e nebula. However, future work utilizing more complex modeling that includes an intermediate ionization zone will be useful to better understand contributions from dense cores.

5.6.3. A Multi-Phase Ionization Zone With A Mix of Lowand High-Densities

Previous studies have investigated the biases inherent to electron density diagnostics and showed that the interplay between an ion's ionization potential and $n_{e,crit}$ is essential to determining which gas phases each diagnostic reliably traces (e.g., Rubin 1989; Méndez-Delgado et al. 2023). In this work, we have also examined the role of different densities in different ionization zones (gas of different ionization potentials). We now shift our focus to the specific role of critical density. To isolate this effect, we consider a single ion (i.e., a single ionization zone) but allow the gas to have a non-uniform density distribution. We explore how fractional contributions from low- and high- n_e gas components influence n_e -diagnostics within this single-ion model by predicting

emission line fluxes via PyNeb emissivities and combining them using a simple linear mixture weighted by the high- and low- n_e volume fractions of each component. For this exercise, we adopt two representative density phases: a low-density component at 10^3 cm⁻³ and a high-density component at 10^5 cm⁻³.

Figure 11 illustrates the resulting effects of this multiphase density structure of a single ion's diagnostic behavior. The left panel shows the inferred n_e $(n_{e,infer})$ from six different n_e diagnostics as a function of the fractional contribution from the high- n_e gas, along with the volumetric mean n_e $(n_{e,avq})$ of the two components. This simple two-phase model reveals that the diagnostics with the lowest critical densities (the low-ionization optical lines in this case), are strongly biased towards the low-density gas value. This occurs because emission from the high- n_e gas is collisionally de-excited, suppressing contributions to the observed flux. As a result, these diagnostics trace the low-density component even when it constitutes less than $\approx 15\%$ of the total volume. On the other hand, diagnostics with higher critical densities (e.g., the high-ionization UV lines) remain sensitive to the high- n_e gas except when it contributes < 15% to the total volume. Notably, these higher- $n_{e,crit}$ diagnostics also yield inferred densities that are in much closer agreement with $n_{e,avq}$.

The right panel of Figure 11 compares $n_{e,infer}$ and $n_{e,avg}$ for the six n_e diagnostics, where the highest ionization n_e diagnostics more closely trace $n_{e,avg}$. Overall, this exercise highlights how collisional de-excitation in high-density gas can bias n_e diagnostics toward lower inferred values, particularly for transitions with low critical densities. A more complex model—relaxing the simplifying assumptions adopted here—would be required for quantitative accuracy, but this approach effectively captures the underlying physical trend and diagnostic biases.

6. IMPLICATIONS FOR THE HIGH-Z AND LOW-Z SAMPLES

In Section 5, we showed that high densities can significantly impact our derived nebular properties, especially the temperature, ionization parameter, and oxygen abundance. An additional implication of our results is that electron densities derived from low- $n_{e,crit}$ diagnostics should be regarded as lower limits of the true conditions of the ionized gas. In this section, we examine two methods to determine physical conditions (i.e., $\log U$, T_e , n_e) and abundances (O/H and N/O) for the Low-z and High-z Samples: (1) the uniform density model commonly adopted in the literature, assuming a 2-zone ionization structure for the temperature and (2) a

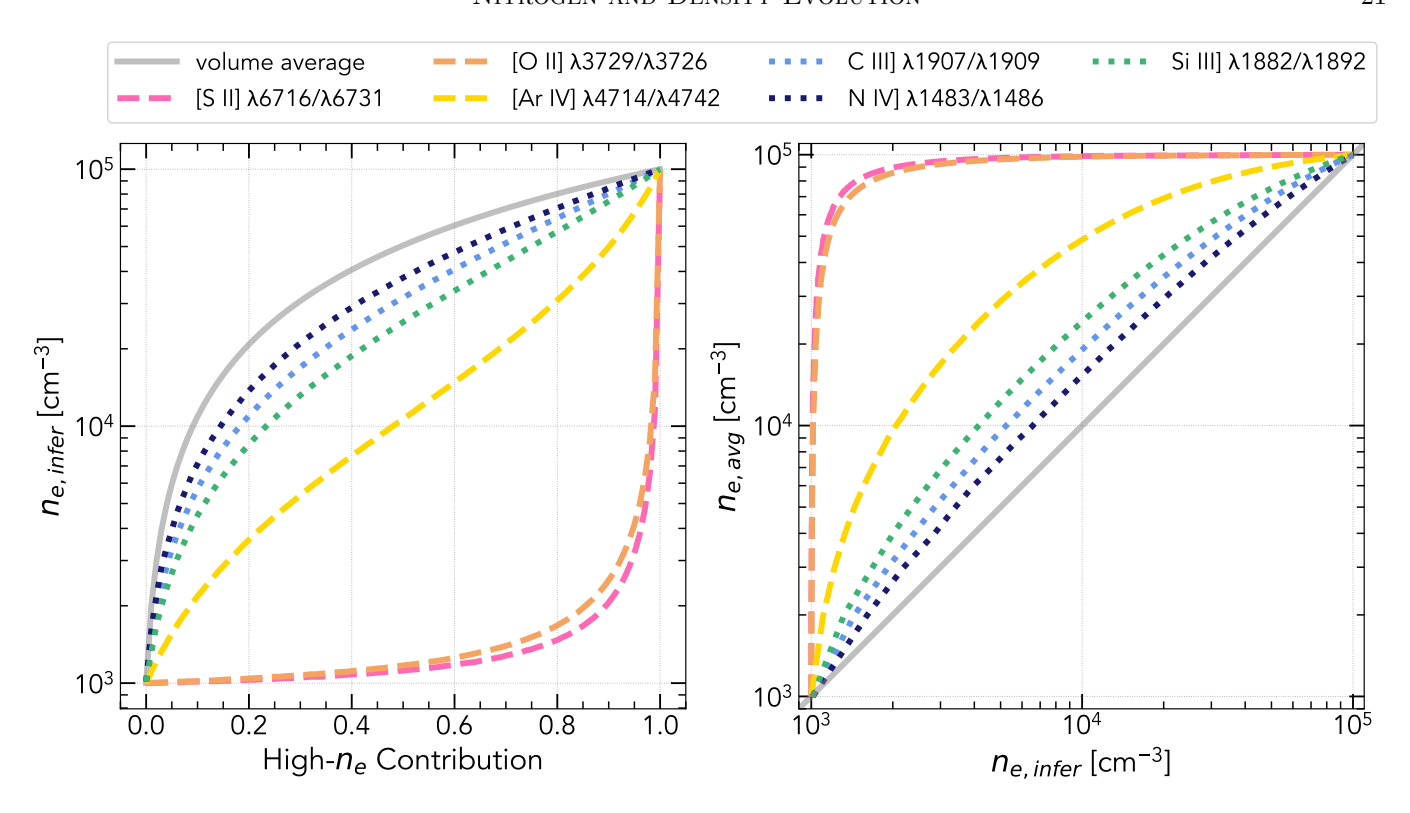


Figure 11. Left: Density inferred from a given density diagnostic emission line ratio versus the volume fraction of high-density gas for a two-phase density model for a given ion, with low-density gas of 10^3 cm⁻³ and high-density gas of 10^5 cm⁻³. The true volumetric averaged density is plotted as the solid magenta line. In comparison, nebular density diagnostics measure lower densities with the low-ionization optical diagnostics severely biased to the low-density value for most of the fractional range, while the high-ionization UV diagnostics more closely trace the $n_{e,avg}$ due to their increased sensitivity to high- n_e gas. Right: We compare the $n_{e,infer}$ for each diagnostic emission line ratio to the $n_{e,avg}$ to emphasize which ions serve as good tracers of the true $n_{e,avg}$ for an ionization zone with a multi-phase density.

multiphase density model adopting a T_e and n_e for each ionization zone in the classic 3-zone ionization model.

6.1. Multi-Phase Physical Conditions and Their Effects

As discussed in Section 5.2, accurate nebular diagnostics require correctly interpreting the electron temperature and density across the ionization structure We use the getTemDen function in of the nebula. PyNeb to determine the temperature and density in each ionization zone. For density determinations, we assume a T_e of 1.5×10^4 K, as n_e determinations are not very sensitive to T_e (e.g., Osterbrock & Ferland 2006), and use the [S II] $\lambda 6733/\lambda 6718$ ratio for the lowionization zone ($n_{e,low}({\bf S}^+)$), the C III] $\lambda 1909/\lambda 1907$ ratio for the intermediate-ionization zone $(n_{e,int}, (C^{+2}))$, and N IV] $\lambda 1487/\lambda 1483$ for the high-ionization zone $(n_{e,high}(N^{+3}))$. However, many of the objects in our high-z sample do not have resolved low-ionization density diagnostics, so we use the $n_e - z$ relation derived in Abdurro'uf et al. (2024) to characterize the $n_{e.low}$. We note that the $n_e - z$ relation presented Abdurro'uf

et al. (2024) is consistent with other relations in the literature (e.g., Isobe et al. 2023a; Topping et al. 2025a) such that this choice of relation will have little impact on the results. The resulting low-ionization densities range from $n_{e,low} = (0.3-4.4) \times 10^2$ cm⁻³ for the low-z sample (e.g., Davies et al. 2021; Berg et al. 2022) and from $n_{e,low} = (1.0-22.6) \times 10^2$ cm⁻³ for the high-z sample (e.g., Topping et al. 2025a; Stanton et al. 2025).

When comparing densities from different ionization zones it is important to consider the diagnostic range of each density diagnostic. A conservative, but useful range to use for a given diagnostic is

$$0.1 \times n_{e,crit.}^{low} \lesssim \text{ diagnostic range } \lesssim 10 \times n_{e,crit.}^{high},$$
 (3)

where $n_{e,crit.}^{low}$ is the lower critical density and $n_{e,crit.}^{high}$ is the higher critical density of a given diagnostic ratio. With this definition, we adopt the following diagnostic ranges (see Table 3 for $n_{e,crit}$): $\sim 1 \times 10^2 - 5 \times 10^4$ cm⁻³ for n_e [O II], $\sim 2 \times 10^2 - 5 \times 10^4$ cm⁻³ for n_e [S II], $\sim 9 \times 10^3 - 1 \times 10^{10}$ cm⁻³ for n_e C III], and $\sim 2 \times 10^4 - 6 \times 10^{10}$ cm⁻³ for n_e N IV]. Within the diag-

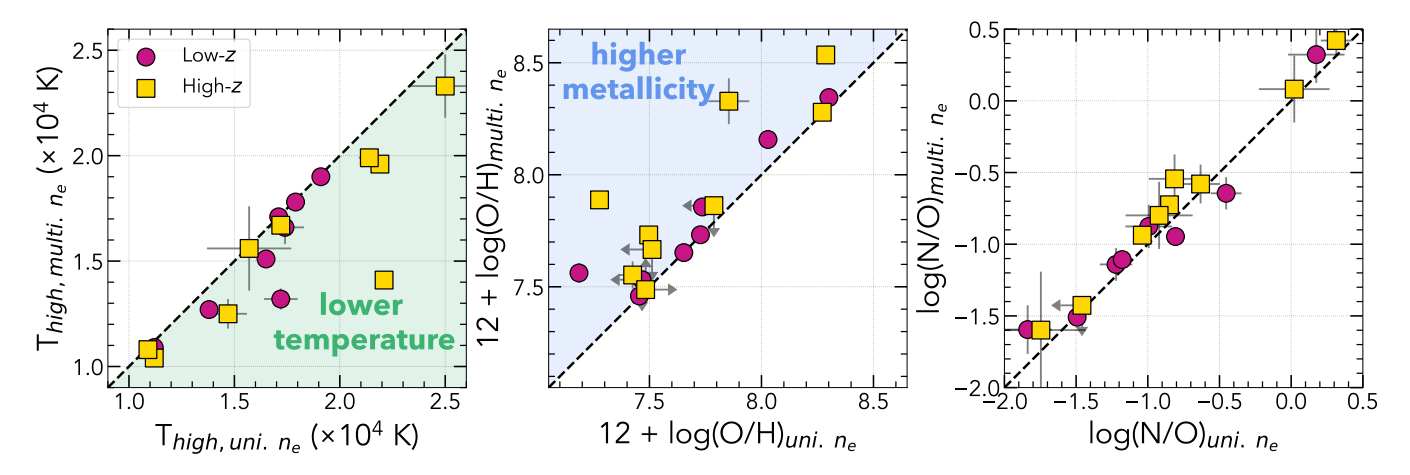


Figure 12. Left: $T_{e,high}$ when assuming a constant n_e when compared to when assuming a 3-zone n_e . We find that the 3-zone n_e model produces lower $T_{e,high}$ than the constant n_e model. Middle: Comparing the gas-phase metallicities between these two models predictably shows that the 3-zone n_e model generates higher metallicities. Right: When looking at the UV $\log(N/O)$ derived in each model, we find that the 3-zone n_e model on average drives UV $\log(N/O)$ up for both our high-z and low-z samples.

nostic range of a given line ratio, the ratio will change sensitively as a function of density, but outside of this range the diagnostic line ratio will flatten. The so-called "low-density limit" defines the upper diagnostic line ratio plateau (typically $F_1/F_2 \sim 1.3-1.6$) at densities less then $0.1 \times n_{e,crit}^{low}$ and the "high-density limit" defines the lower diagnostic line ratio plateau (typically $F_1/F_2 \sim 0-0.5$) at densities greater then $10 \times n_{e,crit}^{high}$. This means that low densities of $\lesssim 10^3 \ {\rm cm}^{-3}$ will never be measured with C III] or N IV] and high densities of $\gtrsim 10^5 \ {\rm cm}^{-3}$ will never be measured with [O II] or [S II].

Considering only measurements in the diagnostic sensitivity ranges, the densities derived from the intermediate- and high-ionization tracers (i.e., N IV], C III) are often significantly higher than those derived from low-ionization lines (i.e., [S II]), especially for the high-redshift galaxies. This implies significantly different densities in the different ionization zones, where density increases with ionization. Note that if the low- and high-ionization zone densities were similar in reality, at least one of diagnostic line ratio measurements would be in the low- or high-density limit. Additionally, even the measurements in the sensitivity range for $n_{e,int}$ and $n_{e,high}$ should be considered upper limits, as the n_e^2 dependence of emission lines means that integrated flux will be dominated by regions of higher n_e in gas with an inhomogeneous n_e distribution. Harikane et al. (2025) emphasizes the presence of multiphase gas in objects that are known to have high-density gas as traced by UV and optical emission line ratios. The authors argue that detections of [O III] $52\mu m$ and [O III] $88\mu m$, which both have relatively low $n_{e,crit}$, are only possible if these systems also contain low-density gas given that [O III] $52\mu m$ and [O III] $88\mu m$ would be completely suppressed in an entirely high-density nebula.

We explore the possibility of using [Ar IV] $\lambda\lambda 4713,4742$ to probe $n_{e,high}$ given that this n_e diagnostic is securely sensitive above 1.73×10^3 cm⁻³. However, for the seven low-z galaxies for which we can derive $n_{e,high}(Ar^{+3})$, we note that only one of them is above the sensitivity limit for this diagnostic. In cases where we can compare these n_e to $n_{e,high}(N^{+3})$ and $n_{e,int}(C^{+2})$, we also find that the derived $n_{e,high}(Ar^{+3})$ values are systematically lower. The C III] and N IV] ions require higher ionization potentials, excitation energies, and originate from levels with higher $n_{e,crit}$ than [Ar IV] (see Table 3). The presence of all these emission lines suggest that the UV lines may be produced in different subregions of an inhomogeneous, non-uniformly mixed high-ionization zone than the optical [Ar IV] lines (e.g., Pascale et al. 2023). Therefore, to probe the highest n_e regimes in a given ionization zone, we opt to exclusively use $n_{e,high}(N^{+3})$ and $n_{e,int}(C^{+2})$ in this work.

In the low-z sample, we estimate that the average high-ionization density is ~ 20 times higher than the low-ionization density and 3.45 times higher than the intermediate-ionization density, while in the high-z sample we find that the average high-ionization density is ~ 260 times higher than the low-ionization density and ~ 2 times higher than the intermediate-ionization density. This suggests a multiphase gas with a density gradient such that the higher-ionization zones have higher densities, consistent with previous $z \sim 0$ findings (e.g., Berg et al. 2021; Mingozzi et al. 2022), but with steeper

gradients at higher redshifts. Therefore, for objects that do not have either a C III] or N IV] detection, we estimate the other from using the averages above.

We derive high-ionization zone temperatures $(T_{e,high})$ using an [O III] emission line ratio with a high-ionization zone density. We use the [O III] $\lambda 4364/\lambda 5008$ for objects with $> 3\sigma$ detections. For the other galaxies, namely GN-z11, the Sunburst arc, J1723+3411, SL2S J0217, and the Lynx arc, we use the O III] $\lambda 1666/$ [O III] $\lambda 5008$ ratio. To infer low- and intermediate-ionization temperatures, we use the T_e - T_e relations from Garnett (1992). The resulting temperatures and densities are reported in Tables 9 and 10 in Appendix D.

In the left panel of Figure 12, we compare the multiphase versus constant n_e determinations of $T_{e,high}$ for our low-z and high-z samples. It is clear that constraining $T_{e,high}$ with a low-ionization n_e probe leads to higher high-ionization zone temperatures on average, which in turn lead to lower metallicities.

6.2. Ionization Parameters

We use the bicubic relationship presented in Section 5.5 to derive $\log U_{int}$, which describes the intermediate ionization zone, for the objects in our sample that have O_{32} . For the seven low-z objects with detections of both [Ar III] and [Ar IV], we use the Ar₄₃ diagnostic from Berg et al. (2021) to determine $\log U_{high}$. Since the high-z sample lacks Ar_{43} measurements, instead, we use the N₄₃ fit from Table 4 for the objects that have both N III] and N IV] to determine $\log U_{high}$. Note that the N_{43} ratios for our high-z sample are higher than the range of our photoionization models, suggesting very high ionization parameters of $\log U > -1.0$. However, it is difficult to disentangle whether the true $\log U$ is definitely higher or if N IV and N III are being produced by different mechanisms. The ability to independently derive $\log U_{high}$ from another highto intermediate-ionization emission line ratio would be helpful in distinguishing which is the case. This leaves a total of 5 objects across the low-z and high-z samples for which we cannot derive a $\log U_{high}$. For both $\log U_{int}$ and $\log U_{high}$, we use the fits from the uniform low- n_e models that are described in detail in Section 5 with the $n_{e,high}$ values reported in Tables 9 and 10 in Appendix D. Ionization parameters are also reported in Tables 9 and 10 in Appendix D.

6.3. O/H and N/O Abundances

We follow the abundance methods described in Section 5.3. We use the T_e and n_e calculated in Section 6.1 to derive direct gas-phase abundances for our entire sample under two n_e assumptions. For the uniform density model, we use the $n_{e,low}$ versions of $T_{e,low}$

to determine O^+ , N^+ , and N^{+2} and $T_{e,high}$ to determine O^{+2} and N^{+3} . For the multi-phase model, the intermediate-ionization N^{+2} ion is instead determined using the $n_{e,int.}$ -derived $T_{e,int.}$ and the high-ionization O^{+2} and N^{+3} ions are determined the $n_{e,high}$ -derived $T_{e,high}$.

The ionic oxygen abundances are added to determine the total oxygen abundance. In the absence of [O II] emission, the derived O abundance is a lower limit. However, for weak detections of [O II] emission, we report O/H abundances as upper limits. We determine the N/O abundance using the five ion ratios and their corresponding ICFs described in Section 5.5.1. For the uniform density model, $\log U_{int.}$ is used for the ICFs. However, for the multi-phase model, $\log U_{high}$ is used for the ICFs. In the cases where $\log U_{high} = -1.0$ is calculated by N_{43} , the ICFs are near 1.0 for N^+/O^+ , between $\sim 1.1 - 1.6$ for N^{+2}/O^{+2} , and at their least extreme for N^{+3}/O^{+2} . Given the high-ionization lines the true $\log U$ must be high, but if it is instead -2.0 < $\log U < -1.0$, the ICFs don't change significantly for N^{+}/O^{+} , N^{+2}/O^{+2} , and N^{+3}/O^{+2} . The total O/H and relative N/O abundances can be found in Tables 9 and 10 in Appendix D.

The middle and right hand panels of Figure 12 compare the oxygen abundances and UV N/O abundances, respectively from the uniform density and multi-phase methods. The uniform low density method tends to be biased towards lower oxygen abundances, which is a result of the temperatures being biased higher. On the other hand, when comparing a uniform density to a multi-phase density framework, the derived UV N/O does not change significantly. This is because the UV N and O emission lines have high critical densities and so are are relatively insensitive to density. The optical N and O emission lines, on the other hand, have lower critical densities, making their ratio more sensitive to densities for $n_e > 10^3 \ \rm cm^{-3}$ (see Figure 6).

7. THE EVOLUTION OF N/O

Detailed chemical abundance studies of local H II regions and galaxies have long used low-ionization optical emission to trace relative N/O abundances. These studies have established the well-known bi-modal N/O–O/H relationship (e.g., Garnett 1990; Henry et al. 2000; van Zee & Haynes 2006; Nava et al. 2006; Pilyugin et al. 2012; Berg et al. 2012, 2019; Izotov et al. 2023). At low metallicity ($12 + \log(O/H) \lesssim 8.0$), the N/O ratio is relatively constant due to the metallicity-independent (primary) production of both N and O. However, at higher metallicities ($12 + \log(O/H) \gtrsim 8.0$), the rate of N production through the metallicity-dependent (secondary)

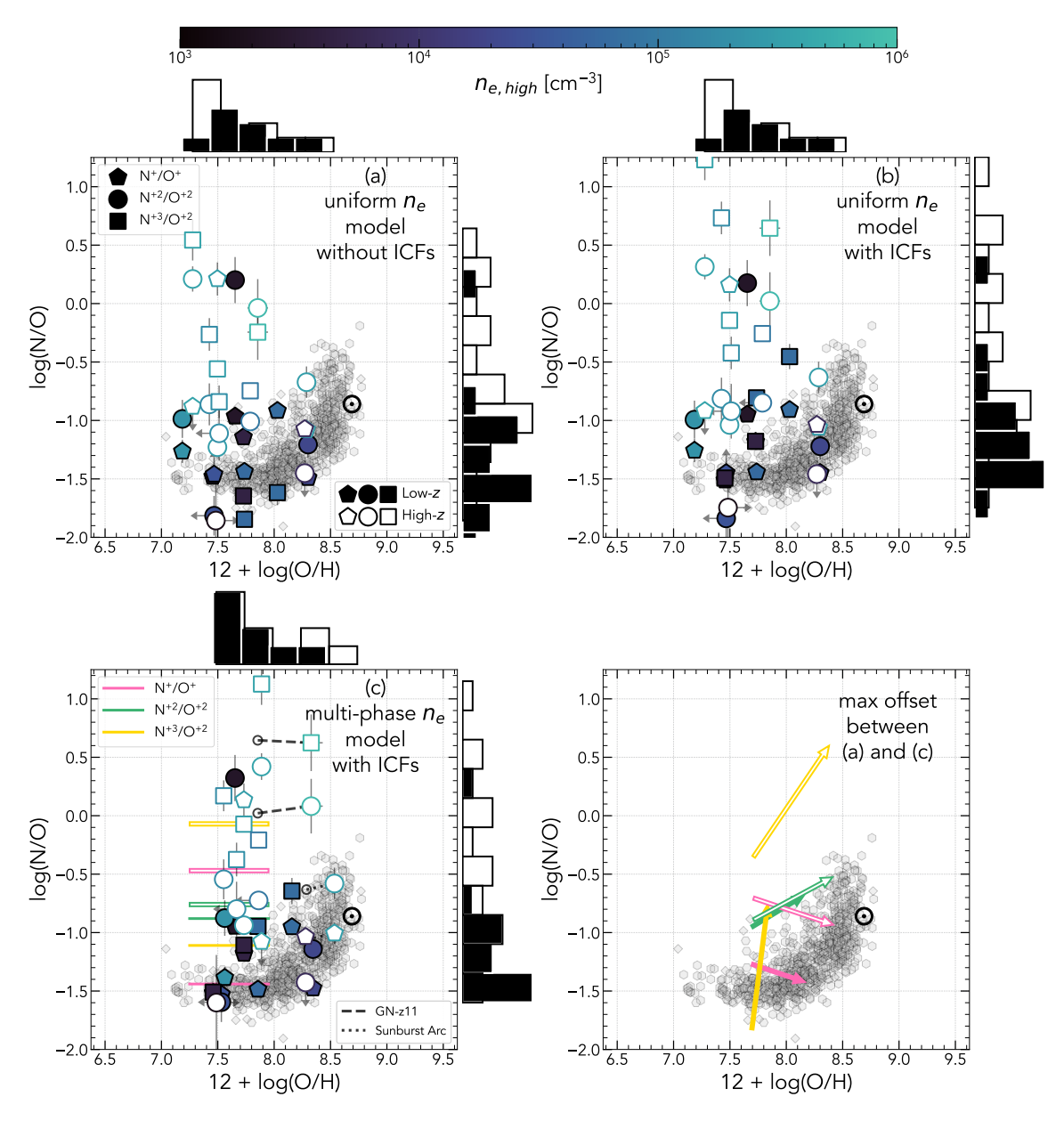


Figure 13. The gray scatter of points in both panels are the N/O-O/H scatter for local measurements of N/O in H II regions (Pilyugin et al. 2012; Berg et al. 2020; Rogers et al. 2021, 2022), low-mass metal-poor galaxies (Berg et al. 2012, 2019; Izotov et al. 2023), and CLASSY galaxies (Arellano-Córdova et al. 2025b). These measurements demonstrate clearly the expected evolution of N/O based on low-ionization optical emission. The various ICF corrected variations of N/O that we calculated are distinguished by marker shape. The pentagons represent N^+/O^+ , circles are N^{+2}/O^{+2} , and squares show N^{+3}/O^{+2} . The filled shapes are galaxies in our low-z sample and the high-z sample are plotted as unfilled shapes. The color bar gives the n_{high} used in the calculations for the 3-zone n_e model. The histograms show the distributions of N/O and O/H values in each panel for the low-zand high-z, which are shown with black and white histograms, respectively. In each of these panels, the low-z outlier at high-N/O is Mrk 996, which is being enriched by a large population of WN stars. Upper Left: The uniform n_e model described in Section 6 without ICFs. There is a clear discrepancy between literature scatter and most of our low-z and high-z measurements. Upper Right: We plot the uniform n_e model detailed in Section 6 with ICFs. We note that the discrepancy seen in the first panel is still present in the second one and is more severe for some points. Lower Left: Our new physical conditions determinations, described in Section 6, are used to calculate new direct gas-phase metallicities and N/O measurements, where possible, for both samples. Additionally, we include lines that demonstrate the median value for each type of N/O for $12 + \log(O/H) < 8.0$ in the low-z (filled line) and high-z (unfilled line) samples. These medians allow us to highlight that the high-z sample has, on average, higher N/O than the low-z sample suggesting a redshift evolution in the derived N/O for all tracers. Note, we mark with dashed and dotted lines the changes between (b) and (c) for two objects, GN-z11 and Sunburst Arc, which we discuss further in Section 7. Lower Right: We plot the maximum vector offsets for the each tracer of N/O for both the low-z and high-z sample between the uniform n_e model with no ICFs and our multiphase with ICFs n_e model. The N⁺/O⁺ measurements on average shift down and to the right. The N⁺²/O⁺² measurements generally shift up and, or, to the right for our recalculated values. The N^{+3}/O^{+2} values change the most notably since these measurements require much larger ICFs across varying $\log U$.

processes exceeds the rate at which O is being produced and the ratio increases (e.g., Edmunds & Pagel 1978; Henry et al. 2000). There is also significant scatter in the N/O vs O/H relationship ($\sigma \sim 0.5$ dex, Berg et al. 2019) that is thought to result from various time-dependent mechanisms such as inflows of pristine gas, metal-rich outflows, and stellar yields (Pérez-Montero et al. 2016; Berg et al. 2019; Arellano-Córdova et al. 2025b, e.g., CCSNe, asymptotic giant branch).

While decades of work on low-ionization optical N/O abundances paints the familiar picture described above, how the N/O-O/H trend evolves with redshift is not well-known. This is due, in part, to the fact that extending N/O studies to higher redshifts is difficult, as the optical lines are redshifted into the infrared. The advent of the JWST has opened a new window onto high redshift abundance studies, with NIRSpec's sensitivity and restwavelength coverage $(0.6-5.3 \mu m)$ enabling [N II] $\lambda 6585$ detections out to $z \sim 7$. For example, Scholte et al. (2025) recently presented a direct-method N/O-O/H analysis of 12 galaxies spanning $1.80 \le z \le 5.2$ (see also Strom et al. 2017; Hayden-Pawson et al. 2022; Sanders et al. 2023), but larger studies are needed to assess the evolution statistically. Unfortunately, the optical [N II] line is typically weak in the metal-poor galaxies that are expected to be more common at high redshifts, and so has proven difficult to detect. Alternatively, N/O abundances can be determined using the high-ionization rest-UV N IV] $\lambda\lambda 1483,1487$, O III] $\lambda\lambda 1661,1666$, and N III] $\lambda 1750$, when available. However, recent highz studies find significantly elevated N/O derived from these high- and very-high-ionization UV emission lines that is in conflict with local studies. Therefore, understanding the evolution of N/O requires robust and consistent measurements of N/O from both UV and optical lines.

The N/O–O/H trend is illustrated in Figure 13 for the uniform-density method without ICFs (upper left), uniform-density method with ICFs (upper right), multiphase method (lower left), and maximum vector offsets between uniform-density method without ICF and the the multiphase method. The gray points are $z \sim 0$ low-ionization optical N/O measurements (data from Pilyugin et al. 2012; Berg et al. 2012, 2019, 2020; Rogers et al. 2021, 2022; Izotov et al. 2023; Arellano-Córdova et al. 2025b). In comparison, we plot the N/O abundances derived from N⁺/O⁺ (pentagons), N⁺²/O⁺² (circles), and N⁺³/O⁺² (squares) for our sample, color-coded by their high-ionization zone densities.

The low-z sample values are fairly consistent for the uniform-density and multi-phase density panels with ICFs; however, several of the high-z sample points

change significantly owing to their higher $n_{e,high}$ values, which shift their O/H abundances to higher values in the multi-phase model. As a result, the N/O enrichment above the $z \sim 0$ trend is reduced for several of the galaxies in our sample. For example, the Sunburst Arc's metallicity increases from a $12 + \log(O/H) = 8.3$ to 8.5, shifting it to agree with the secondary N/O relationship. Further, using the mutli-phase density model for GN-z11 increases the O/H abundance by 0.47 dex and increases the N/O abundance from N^{+2}/O^{+2} by ~ 0.10 dex, bringing the N^{+2}/O^{+2} and N^{+3}/O^{+2} abundances closer together and reducing the enhancement above the N/O-O/H trend to ~ 0.7 dex. However, we note that the lack of variation on the N/O-O/H plane does not imply a homogeneous n_e structure. At low-z the density inhomogeneities could be on the order of a few hundred cm⁻³; this would not significantly impact the UV and optical emission lines examined here but would have a noticeable effect on infrared fine-structure lines (e.g., [O III] $52\mu m$, [O III] $88\mu m$, [N II] $122\mu m$, [N II] $205\mu m$).

While using the multi-phase density model produces more accurate N/O abundances that better agree with the expected N/O-O/H trend, significant outliers remain. For the subset of low-metallicity galaxies in low-z sample $(12+\log(O/H) < 8.0)$, we find that the median N/O abundance from N^+/O^+ is -1.44 dex (green plateau in Figure 13), consistent with decades of local studies examining the N/O plateau traced by low-ionization emission (e.g., van Zee & Haynes 2006; Berg et al. 2019). The UV N/O values measured from N^{+2}/O^{+2} and N^{+3}/O^{+2} for the same sample are higher, with median values of -0.88 and -1.11 dex (green and gold solid lines in Figure 13), respectively. This $\Delta N/O = 0.33 - 0.56$ dex disagreement is unexpected, as different ionic abundance methods should converge on consistent elemental abundance ratios if properly calibrated. Thus, the unknown origin of this discrepancy raises concerns that the high-ionization UV N/O diagnostics may systematically overestimate N/O and calls into question the robustness of the high-ionization UV N/O measurements in high-redshift systems.

For the low-metallicity high-z galaxies, the median N/O values are -0.47, -0.76, and -0.07 dex from N⁺/O⁺, N⁺²/O⁺², and N⁺³/O⁺², respectively (dashed lines in Figure 13). These values suggest that the UV-optical discrepancy only decreases for N⁺²/O⁺² and increases for N⁺²/O⁺² at higher-redshifts to Δ N/O = -0.27 and 0.40 dex with higher N/O values regardless of the measurement method. Note, however, that the high-z N⁺/O⁺ median value is only based on two measurements that are highly discrepant. While the high-z median N⁺³/O⁺²-derived N/O value is consistent with

the UV N-emitters in recent studies (e.g., Senchyna et al. 2024; Isobe et al. 2023b), there is significant scatter in the UV N/O measurements at high-z such that the median value is close to solar, reducing its discrepancy. Given these results, more robust N/O measurements from N⁺/O⁺ are needed at high redshifts to understand the significance of any N/O evolution.

Recent work by Hayes et al. (2025) derives UV N/O from stacks of high-z galaxy spectra from the DAWN JWST $Archive^8$ (DJA). The authors find that using a $n_e \sim 10^6$ cm⁻³ in the abundance determinations for these stacks has more impact on the derived T_e , and subsequently the gas-phase metallicity, than the UV N/O. However, this change is significant in that it brings the measured points in agreement with the high-metallicity increase in the optical N/O scatter on the N/O-O/H plane. Additionally, this result is consistent with our findings in Figure 13, where we determine that using the appropriate physical conditions can have a notable impact on the placement of points on the N/O-O/H plane overall.

If the N/O-enhancement of the high-z galaxies is taken to be true, it would imply either earlier that expected star-formation such that significant AGB enrichment has occurred or a surprisingly fast enrichment of N (e.g., Kobayashi & Ferrara 2024; Arellano-Córdova et al. 2025a). Prompt enrichment of nitrogen could occur via very massive stars (VMSs; $M_{\star} > 100 M_{\odot}$; e.g., Nandal et al. 2024a), where rotational mixing enables hot-CNO cycling and early N production. Then, the observed scatter in N/O at fixed O/H could be explained by the diversity of star formation modes and stellar populations in our total sample, with some galaxies enriched by early generations of VMSs and others dominated by delayed AGB enrichment.

7.1. Density Evolution

We have shown that emission line ratios and abundances are sensitive to the derived physical conditions. Previous works have also show that high- n_e , in particular, can bias interpretations of observed galaxy properties (Katz et al. 2023; Cullen et al. 2025; Rusakov et al. 2025), while earlier studies of $z \sim 2-3$ galaxies have suggested that nebular density may evolve with redshift (e.g., Sanders et al. 2016; Kaasinen et al. 2017). Thus, the observed high N/O abundances may also be related to the evolution of n_e .

Figure 14 presents the z evolution of the $n_{e,low}$ (green), $n_{e,int}$ (light blue), and $n_{e,high}$ (dark blue).

From a cosmology perspective, the virial density of dark matter halos evolve according to $(1+z)^3$. It follows naturally that ISM conditions would scale similarly towards more extreme n_e with increasing z. We fit the z evolution of $n_{e,int}$ and $n_{e,high}$ using $n_e = A(1+z)^p$, where we fix A to be the average density of the low-z sample. We find that the best-fit redshift evolution of the intermediate- and high-ionization densities for the combined low-z and high-z samples are given by

$$n_{e,int} = 1.11 \times 10^3 \cdot (1+z)^{1.93 \pm 0.08}$$
 (4)

$$n_{e,high} = 5.40 \times 10^3 \cdot (1+z)^{1.62 \pm 0.12}.$$
 (5)

In comparison, we plot the redshift-evolution trends for the low- and intermediate-ionization densities from Isobe et al. (2023a), Abdurro'uf et al. (2024), and Topping et al. (2025a). The trends for the low-, intermediate-, and high-ionization densities have similar shapes, but offset to higher normalization with increasing ionization. Notably, our $n_{e,int}$ trend is offset from the Topping et al. (2025a) relation due to our sample being generally more extreme and having higher n_e . These offset redshift evolutions of the multi-phase densities in our sample stresses the importance of accurately probing of the complete n_e structure of a galaxy especially in high-z galaxies, where high densities are more likely to bias interpretations of galaxy properties.

While the virial density of dark matter halos increases as $(1+z)^3$ in Λ CDM cosmology, electron density evolves as $(1+z)^{1.93}$ for intermediate-ionization gas and $(1+z)^{1.62}$ for high-ionization gas (Equations 4 and 5). This suggests that the nebular gas density evolves more slowly than the virial density, where feedback, gas accretion, and ISM regulation can moderate how compact the star-forming gas becomes. On the other hand, the ionized gas traced by emission lines is thought to trace a small, pressurized, ionized portion of the entire gas reservoir of a galaxy and this region may have a different scaling with redshift than the neutral gas, molecular gas, or dark matter. Thus, measured densities may reflect more localized environmental conditions rather than global ISM properties and how star formation rate surface density, ionizing photon flux, and geometry evolve with redshift. These findings imply that while cosmological density evolution sets the stage, internal galaxy physics moderate the conditions under which N enrichment proceeds.

Arellano-Córdova et al. (2025b) recently found an increasing trend between $n_{e,low}$ densities, probed by [S II], and N/O values from N⁺/O⁺ for both local and z=2-6 galaxies. These authors suggest that this trend is driven by collisional de-excitation of [O II] in the low-ionization gas.

⁸ https://dawn-cph.github.io/dja/

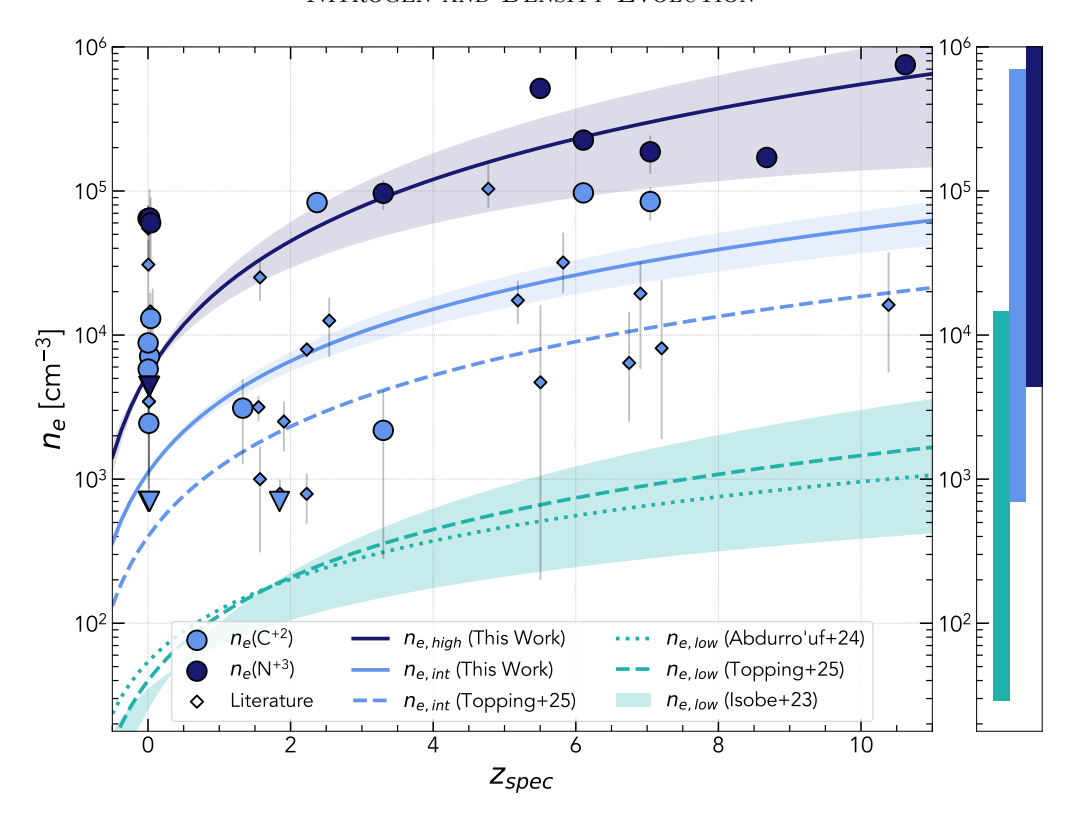


Figure 14. The redshift evolution of $n_e(C^{+2})$ and $n_e(N^{+3})$ for our low-z and high-z sample of galaxies. Our fits to this relationship for $n_e(C^{+2})$ and $n_e(N^{+3})$ are shown in solid light and dark blue lines, respectively. The light blue circles show $n_e(C^{+2})$ values, while the dark blue circles are $n_e(N^{+3})$ values. We include literature measurements of $n_e(C^{+2})$ from Maseda et al. (2017), Berg et al. (2019), and Topping et al. (2025a) as small light blue diamonds. Downward pointing triangles of any color are showing where the derived n_e are upper limits. Additionally, we compare the $n_{e,low}-z$ trends derived by Abdurro'uf et al. (2024) and Topping et al. (2025a) as dotted and dashed lines. In the right panel, we show the sensitivity ranges of the diagnostics used in deriving low-, intermediate-, and high-ionization n_e . We show that the intermediate- and high-ionization n_e are higher than the low-ionization n_e across all redshifts, and the higher-ionization n_e diagnostics follow $\propto (1+z)^{1.5-2.0}$, which similar to the trend for the low-ionization n_e redshift evolution.

To further explore the n_e -N/O trend for all ionization zones of gas, we combine the density and N/O measurements in Figure 15 by plotting the N/O abundances derived from N⁺/O⁺ (green pentagons), N⁺²/O⁺² (light blue circles), and N⁺³/O⁺² (dark blue squares) versus the electron density for the corresponding N ion. Each of these n_e diagnostics have different ranges of sensitivity, and in Figure 15 we show which measurements fall below the lower bounds of a conservative sensitivity range for each diagnostic with semi-transparent points. The n_e plotted as triangles are upper limits for cases where the diagnostic ratio was higher than the low-density limit, however, we emphasize that we only fit measurements are within the conservative sensitivity range for each of the different densities. We find that for $n_e \gtrsim 3 \times 10^3 \text{ cm}^{-3}$, even after accounting for unseen ionic species and appropriate n_e structure, there is an increasing N/O trend with the n_e used to derive them. This relationship is well fit by the same type of analytic

function used to describe the scaling between O/H and N/O in Groves et al. (2004) and Nicholls et al. (2017).

$$\log(N/O) = \log(10^{-1.27 \pm 0.11} + 10^{\log(n_e) - (5.49 \pm 0.11)}),$$
(6)

which shows that most of the extreme-N/O systems, as probed by high-ionization emission lines, also have the highest densities. Similar trends are also seen for the low-, intermediate-, and high-ionization $N/O-n_e$ relationships individually, suggesting that the extreme abundances in these galaxies may be driven by conditions that also drive extreme high-ionization densities. The general trend of increasing N/O with gas density implies that denser, more pressurized environments favor efficient N enrichment, possibly through VMS formation or enhanced mixing.

Notably, the extreme n_e and T_e observed in N/O enhanced galaxies at high-z suggest a highly multi-phase ISM that may be the result of witnessing galaxies in the very early phase of an extreme burst of star forma-

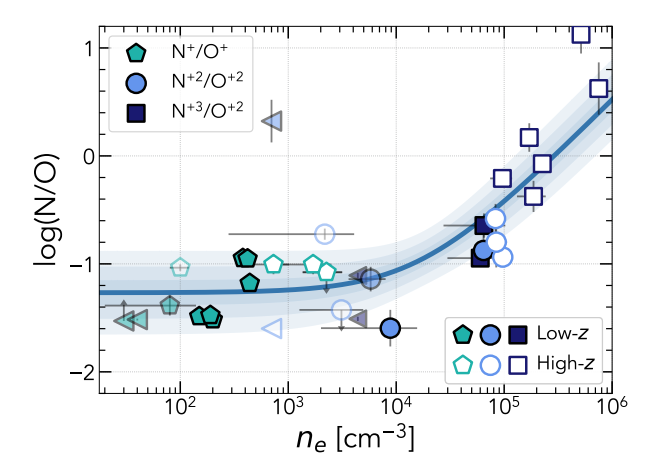


Figure 15. We explore the relationship between n_e and various tracers of N/O. The color and marker shape distinguish the various measured N/O, where green pentagons are the N⁺/O⁺, light blue circles are N⁺²/O⁺², and dark blue squares are the high-ionization N⁺³/O⁺². Each N/O measurement is plotted against the n_e used to calculate the emissivity for the N ion utilized in each measurement (i.e., N^{+}/O^{+} vs. n_{low} , N^{+2}/O^{+2} vs. n_{int} , N^{+3}/O^{+2} vs. n_{high}). While filled points show galaxies in our low-z sample, unfilled points are galaxies in our high-z sample. As a precaution, we plot values that fall below the (conservative) sensitivity range as semi-transparent. Specifically, in cases where the diagnostic ratio was greater than the low-density limit, we plot the densities as triangles. It is therefore clear that we are robustly tracing different n_e in different ionization zones for the majority of our sample. We find that the overall increasing relationship between n_e and N/O in this work can be described by a logarithmic fit. Note the outlier in this trend is Mrk 996, which is known to have WR driven Nenhancement.

tion such that thermal pressure equilibrium has not been reached. We consider the possibility that high-ionization zones could be transiently over-dense pockets of gas, where the suppression of collisional coolants keeps the T_e high, so these regions remain both hot $(2-2.5\times10^4~{\rm K})$ and dense. These dense regions would be both dynamical and multi-phase, requiring a comprehensive picture of pressure balance to accurately model, including thermal, radiation, turbulent, ram, and magnetic pressures. However, modeling of such a dynamic environment is outside the scope of this work.

7.2. Relating Nebular Properties and Global Σ_{SFR}

Motivated by the strong correlations of N/O with density, we also examine the star formation rate surface density ($\Sigma_{\rm SFR}$). We determine the $\Sigma_{\rm SFR}$ for our sample using the rest-UV effective radii (R_e) and SFRs presented

in Table 1 along with the following equation:

$$\Sigma_{\rm SFR} = \frac{\rm SFR}{2\pi R_e^2}.\tag{7}$$

The resulting $\Sigma_{\rm SFR}$ values are listed in Table 1.

Topping et al. (2025b) find that the N IV] emission lines in high-z galaxies occur only at the highest ${\rm H}\beta$ equivalent widths pointing to very young stellar populations (Leitherer et al. 1999; Endsley et al. 2023; Matthee et al. 2023) in a short-lived period during a burst of star formation. Additionally, Schaerer et al. (2024) specifically examines $\Sigma_{\rm SFR}$ in UV N-emitters and finds that these galaxies inhabit an extreme position on the $\Sigma_{\rm SFR}$ - $\Sigma_{\rm M_{\star}}$ plane. We note that, in general, spatial resolution limitations can make robust size measurements for highz galaxies challenging, particularly in cases where galaxies are not highly-magnified by lensing. However, going forward, deep JWST imaging will be instrumental in reducing the scatter in the trends involving $\Sigma_{\rm SFR}$.

We examine this in our sample by looking at the $n_e - \Sigma_{\rm SFR}$ relationship for the low- (green pentagons), intermediate- (light blue circles), and high-ionization (dark blue squares) zones in Figure 16, which demonstrates that extreme densities are in fact related to the most extreme regions of SF in a galaxy. We calculate the Pearson's r correlation coefficient along with their corresponding p-values for each set of n_e and for all of them individually. Based on their p-values, each of the Pearson's r values suggest a significant linear correlation except the relationship between $n_{e,high}$ and Σ_{SFR} . We find a weak increasing trend between the derived n_e and the $\Sigma_{\rm SFR}$, which is consistent with the relationship found by previous works between Σ_{SFR} and $n_{e,low}$ (e.g. Shimakawa et al. 2015; Davies et al. 2021; Topping et al. 2025a). This is expected, as higher $\Sigma_{\rm SFR}$ corresponds to more intense and compact star formation, which increases ISM pressure and compresses gas, leading to higher local electron densities. We fit a linear trend to the relationship between $\Sigma_{\rm SFR}$ and n_e that is best described by

$$\log(n_e) = (0.38 \pm 0.14) \times \log(\Sigma_{SFR}) + (2.94 \pm 0.32).$$
 (8)

Additionally, our galaxy sample is divided such that the lower- n_e low-z sample populates the trend at $\Sigma_{\rm SFR} < 100~M_{\odot}~{\rm yr}^{-1}~{\rm kpc}^{-2}$ and the higher-density high-z sample, mostly, populates the $\Sigma_{\rm SFR} > 100~M_{\odot}~{\rm yr}^{-1}~{\rm kpc}^{-2}$ parameter space. This is consistent with Schaerer et al. (2024), who find that dense, compact, UV N-emitting high-z galaxies can be distinguished by their extreme $\Sigma_{\rm SFR}$ and stellar mass surface densities. These findings point to a physical link between local ISM structure and chemical enrichment and suggest that galaxies at earlier

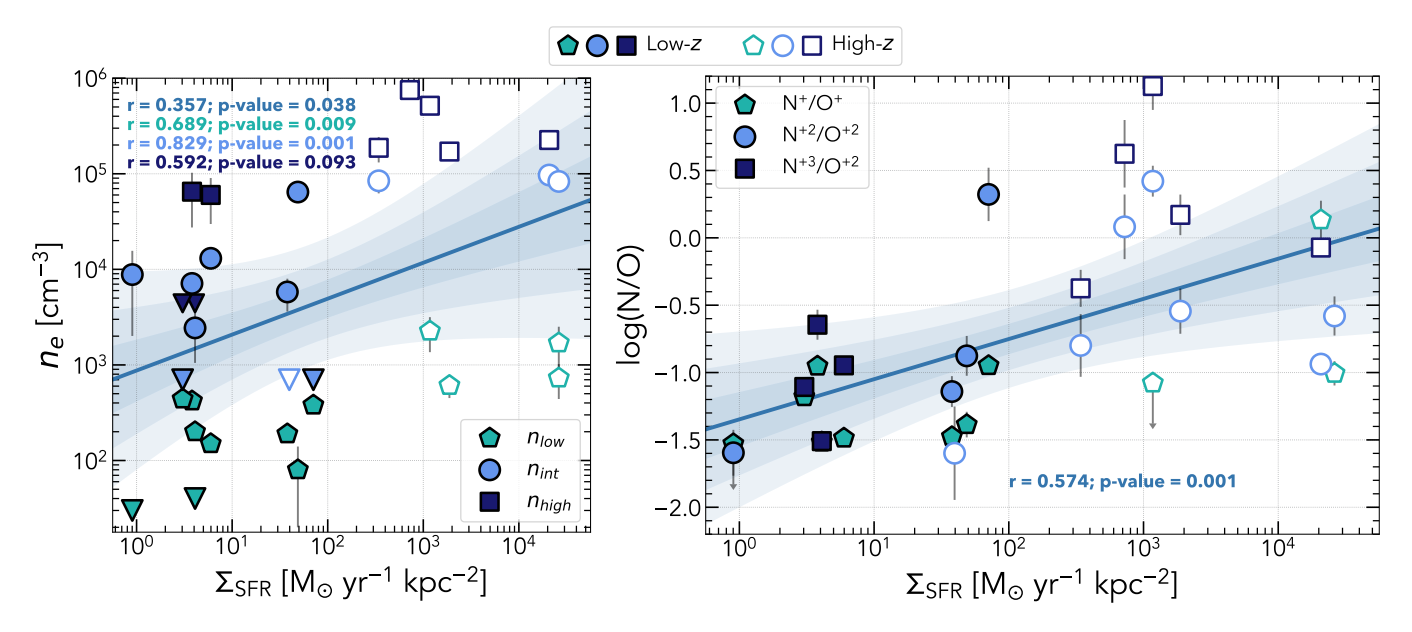


Figure 16. We demonstrate that for our sample the $\Sigma_{\rm SFR}$ correlates with both the n_e and the different tracers of N/O that we measured. We plot the linear best fit for the n_e - $\Sigma_{\rm SFR}$ and N/O- $\Sigma_{\rm SFR}$ relationships with a solid line and show the 3σ errors on the fit. Filled markers are galaxies in our low-z sample, while unfilled markers are galaxies from our high-z sample. The $\Sigma_{\rm SFR}$ clearly sorts all of our galaxies into the low-z and high-z samples since the high-z sample has significantly higher $\Sigma_{\rm SFR}$ than the low-z sample. Upper: We present the n_e - $\Sigma_{\rm SFR}$ for each measured n_e in our sample. The color and marker shape distinguish the various measured n_e , where green pentagons are the low-ionization n_e , light blue circles are the intermediate-ionization n_e , and dark blue squares are the high-ionization n_e . We show the Pearson's r correlation coefficient for all n_e and low-, intermediate-, and high-ionization n_e separately. Each of these p-values suggests a correlation between $\Sigma_{\rm SFR}$ and n_e except for the relationship between $\Sigma_{\rm SFR}$ and the intermediate-ionization n_e . Lower: We show the N/O- $\Sigma_{\rm SFR}$ relationship for every measure of N/O that we obtained in this work. In this plot, the color and marker shape distinguish the various measured N/O, where green pentagons are the N⁺/O⁺, light blue circles are N⁺²/O⁺², and dark blue squares are the high-ionization N⁺³/O⁺². For N/O- $\Sigma_{\rm SFR}$, we only show the Pearson's r correlation coefficient between all the N/O tracers and the $\Sigma_{\rm SFR}$. We find that the best linear fit for N/O- $\Sigma_{\rm SFR}$ is not as steep as the relationship between n_e - $\Sigma_{\rm SFR}$, but the correlation is tighter and less likely to be produced by two uncorrelated sets of data. Additionally, we note that the low-z outlier at high-N/O is Mrk 996, which is known to be experiencing N-enhancement from WR stars.

cosmic times, which exhibit higher values of Σ_{SFR} , may naturally reach temporarily elevated N/O levels through prompt enrichment channels.

In the lower panel of Figure 16, we plot N/O abundances derived from UV and optical ion ratios relative to $\Sigma_{\rm SFR}$, finding a relatively tight positive correlation. The best fit linear relationship between N/O and $\Sigma_{\rm SFR}$ is characterized by

$$\log(N/O) = (0.30 \pm 0.08) \times \log(\Sigma_{SFR}) - (1.35 \pm 0.20).$$
 (9)

While Arellano-Córdova et al. (2025b) finds a similarly positive, albeit weaker, trend when looking at N/O- $\Sigma_{\rm SFR}$ for the CLASSY galaxies, the authors show that the N/H- $\Sigma_{\rm SFR}$ relationship is much more significant.

Figure 16 shows that both n_e and N/O abundance increase with $\Sigma_{\rm SFR}$, indicating that compact, high-pressure star-forming regions are favorable sites for N enrichment. This picture suggests that N production is enhanced under the same conditions that generate intense, spatially concentrated star formation driven by

strong bursts in very young stellar populations, which can be observationally distinguished by their large ${\rm H}\beta$ equivalent widths. In such environments – characterized by elevated densities and ionization parameters – primary N from VMSs may be more efficiently produced and retained. These findings point to a physical link between local ISM structure and chemical enrichment and suggest that galaxies at earlier cosmic times, which exhibit higher values of $\Sigma_{\rm SFR},$ may naturally reach temporarily elevated N/O levels through prompt enrichment channels.

The extreme densities, star formation, and short-lived episodes of N-enhancement in these high—z UV N-emitters make them tantalizing candidates for precursors to little red dots (LRDs). Observationally, LRDs are distinguished by their v-shaped spectral energy distributions from imaging and significant broad emission components in their spectra. Recent works find that the observational signatures that make LRDs so unique are

consistent with dense gas enshrouding a massive black hole (Inayoshi & Maiolino 2025; Naidu et al. 2025; de Graaff et al. 2025). These black holes may be produced via direct collapse of VMSs or gravitational runaway in dense stellar environments (e.g., Greene et al. 2020), both of which could also produce the the elevated N/O in our high-z sample prior to black hole formation. Thus, we speculate that the dense gas enshrouded black holes that may be powering LRDs are remnants of stellar populations that existed in similar conditions as those that drove the elevated N/O in high-z UV N emitters (e.g. Marques-Chaves et al. 2024; Topping et al. 2025a).

7.3. The Source of N/O Enrichment

Although we outline a best-method approach for deriving N/O abundances from high-ionization UV N-emission in Section 5.6, these measurements are still at odds with the low-ionization optical measurements of N/O, especially at high-z. While we acknowledge that poor or out-of-date atomic data could potentially drive this discrepancy, the atomic data would require significant changes to resolve the discrepancy between the UV and optical measurements, which seems unlikely. Therefore, our work leads us to conclude that N/O is in fact elevated in the small fraction of high-z systems with detected N III] and/or N IV] emission lines, but the source of this N-enhancement at high-z is still up for debate.

Since the discovery of GN-z11 (Bunker et al. 2023), one of the now many anomalous UV N-emitters, many works have sought to understand and characterize its unusual UV N abundance pattern. Charbonnel et al. (2023) suggests that high-z UV N-emitters are precursors to globular clusters (GCs). Over the last several decades, studies of GCs have shown that they generally consist of two chemically-distinct populations (e.g., Sneden et al. 1991; Milone & Marino 2022). The first population (1P) shares similar light-element abundance patterns to Milky Way field stars and were born earlier, while the second population (2P) is notably enhanced in He, N, Al, and Na and depleted in O, C, and Mg compared to the field population (e.g., Kraft 1994; Gratton et al. 2019). While Mg and Si emission are sometimes observed for star forming galaxies, they vary significantly between one GC and another. Alternatively, Al and Na could provide more secure identification of GC progenitors, but are rarely observed and so require very high S/N spectra to determine their abundances. In the scenario presented by Charbonnel et al. (2023), proto-globular clusters are polluted by super massive stars (SMSs; $M_{\star} > 1000 \ M_{\odot}$) producing the abundance patterns seen in GN-z11 and other UV N-emitters. This work also shows that GN-z11 is compatible with the stellar mass density and ionized gas mass implied by SMS enrichment, but further evidence is needed to confirm the proto-GC scenario.

Young massive stellar populations provide another possible path to N/O enrichment. Kobayashi & Ferrara (2024) used chemical evolution modeling to demonstrate that multiple bursts of star formation, interspersed with quiescent periods, allows rapid enrichment from Wolf-Rayet stars (WRs) that can reproduce the abundance pattern observed in GN-z11. Further, Senchyna et al. (2024) found that the UV N III] profile of GN-z11 is notably similar to the $z \sim 0$ galaxy Mrk 996 that is known to host WRs based on their detailed optical spectra. While GN-z11 is unlikely to be dominated by classical WRs, the authors argue that high-density massive star formation serves as the primary enrichment source for N-enhanced systems. However, spectral signatures confirming WRs are often not detected or difficult to distinguish from VMSs (e.g., Martins et al. 2023; Berg et al. 2024). Alternatively, Nandal et al. (2025) found that the N/O, C/O, and Ne/O abundances in GS 3037, another remarkably N-rich system, can only be explained using the theoretical yields from SMSs. Further, Nandal et al. (2024b) find that, at extremely low metallicities $(Z=10^{-5}Z_{\odot})$, the abundance patterns seen in GN-z11 can also be reproduced using a set of moderately-torapidly rotating MS stellar evolution models.

These previous works, taken together with our results, suggest prompt enrichment from VMSs is the most plausible explanation for the high-z N-emitting galaxies, but further evidence is needed to confirm this theory. We may also be observing multiple mechanisms at play in the UV N-emitting galaxies and disentangling them with the currently available data is not yet possible. Progress will require deep, high-resolution, multiwavelength spectroscopy to better characterize the physical conditions, abundance patterns, kinematics, and more to constrain the N enrichment mechanisms in high-z galaxies.

8. SUMMARY AND CONCLUSIONS

Recent JWST studies indicate that electron density (n_e) evolves with redshift, especially for strong UV N-emitting galaxies. To assess the effects of n_e on the determination and interpretation of nebular properties and O/H and N/O abundances, we compiled a sample of low-z ($z \sim 0$) and high-z (1 < z < 11) UV N-emitting galaxies, probing a wide range in redshift, metallicity, and physical conditions. By leveraging both new and archival observations from HST and JWST for this sample, we measured n_e in the low-, intermediate-, and high-ionization gas phases and found that they support a

multi-phase density model, where higher-ionization gas is denser, reaching n_e of almost $10^6~{\rm cm}^{-3}$. Therefore, we created a custom suite of Cloudy photoionization models with densities spanning $n_e=10^2-10^9~{\rm cm}^{-3}$ to investigate their effects on nebular UV and optical diagnostics. To do so, we also created the first high-ionization $\log U_{high}$ diagnostic using the UV N₄₃ (= N IV] $\lambda\lambda 1483,1487/{\rm N~III}]~\lambda 1750)$ ratio and N/O ionization correction factors (ICFs), for both UV and optical line ratios, that are calibrated up to $n_e=10^6~{\rm cm}^{-3},$ and so are appropriate for galaxies at all redshifts.

We showed that assuming a uniform, low-density model for a multi-phase density object results in significant biases. The most notable effects are for nebular diagnostics using optical emission lines ratios with differing critical densities such as [O II] $\lambda\lambda 3727,3730/H\beta$, III] $\lambda 5008/H\beta$, [O III] $\lambda 4364/\lambda 5008$, and [O III] $\lambda 5008/\lambda \lambda 3727,3730$. Consequently, assuming the uniform low-density limit $(n_e = 10^2 \text{ cm}^{-3})$ for a high-density gas $(n_e = 10^5 \text{ cm}^{-3})$ results in overestimated $\log U$ values by 1.13 dex, overestimated direct T_e measurements by 1800 K, and underestimated direct 12+log(O/H) measurements by 0.67 dex. Alternatively, diagnostics using only emission lines with high critical densities, such as UV lines, are insensitive to density over the observed n_e range, and so the diagnostics like the [O III] $\lambda 4363/\mathrm{O}$ III] $\lambda 1666~T_e$ diagnostic and the N₄₃ $\log U_{high}$ diagnostic are much more robust. Therefore, we emphasize the importance of adopting a mutli-phase gas model, when possible, for determining nebular gas properties and abundances, especially at high-z where conditions may be more extreme than at low-z. Importantly, in this work, we have assumed the ionizing source to be stellar populations, but in future work we will examine the source of ionizing radiation and it's potential role in producing the extreme objects that feature in this work.

Adopting the multi-phase abundance model for the low-z and high-z samples, we determined O/H and N/O abundances using appropriate electron temperatures and densities for each ionization zone and the new ICFs presented here. For N/O, we considered five different UV and optical emission line ratio combinations that were used to determine the N⁺/O⁺, N⁺²/O⁺², N⁺³/O⁺², (N⁺ + N⁺²)/(O⁺ + O⁺²), and (N⁺² + N⁺³)/O⁺² ion ratios. We find that the effects of n_e are generally small for all five N/O abundance methods compared to that of O/H abundances. While the high-ionization UV N/O diagnostics seem to be robust against n_e effects, the N⁺²/O⁺² and N⁺³/O⁺² UV tracers systematically overestimate N/O by $\sim 0.3-0.4$ dex compared to the low-ionization optical benchmark

 ${
m N^{+2}/O^{+2}}$, particularly in low-metallicity systems at $z\sim 0$. While the multi-phase density structure substantially improved the consistency among methods over the uniform density model, systematic differences remain. This suggests that high-ionization N/O ratios must be interpreted with caution, especially for galaxies observed only in the rest-frame UV with JWST.

Using these diagnostics, we investigated the physical drivers of N/O enrichment. We find that, for the low-z sample, N/O is consistent with the well-established primary plateau at low metallicities and increasing secondary N/O trend at higher O/H. However, we also observe significant scatter at low O/H, including a population of galaxies with elevated N/O that deviate from the canonical plateau, and stronger deviation for the high-ionization UV-based N/O values. The high-z sample shows even stronger enhancements of N/O. While the multi-phase model did reduce this discrepancy and move some high-z objects into agreement with the N/O-O/H trend, the significance of the offset in the remaining objects suggests a real redshift evolution in N/O for this sample.

Examining N/O as a function of n_e showed that electron density plays a critical role in shaping N/O for $n_e \gtrsim 3 \times 10^3$ cm⁻³. Galaxies with higher gas densities exhibit higher N/O values, indicating that nitrogen production is enhanced in dense, high-pressure environments. While the virial density of dark matter halos increases steeply with redshift ($\propto (1+z)^3$), we find that the electron densities of the ionized gas scale more gradually, evolving as $\propto (1+z)^{1.9}$ for intermediate-ionization gas and $\propto (1+z)^{1.6}$ for high-ionization gas. This suggests that while cosmic structure sets the overall density backdrop, baryonic feedback and gas regulation mediate how nebular gas responds to the cosmological environment.

The strongest link between local conditions and enrichment is revealed in the positive correlation between N/O and star formation rate surface density (Σ_{SFR}). This trend indicates that compact, intense star formation – not just integrated star formation history – drives enhanced nitrogen abundances, which is consistent with recent studies examining the properties of UV N emitters (e.g., Topping et al. 2024; Schaerer et al. 2024). In high- $\Sigma_{\rm SFR}$ systems, the ISM is more likely to reach the pressures and densities needed to form very massive stars, which can produce substantial primary nitrogen on short timescales through rotationally mixed winds or chemically homogeneous evolution. These environments may also facilitate more efficient retention of metals, enhancing localized enrichment. Together, the density and $\Sigma_{\rm SFR}$ correlations point to a physical enrichment chan-

nel that enables prompt N production tied to the geometry, intensity, and pressure of star formation itself.

As a whole, our findings argue for more detailed determinations physical conditions and abundances and a more nuanced view of chemical evolution in galaxies at high-z. N enrichment is not governed solely by metallicity or time since star formation onset but is instead shaped by the local conditions under which stars form and evolve. This has important implications for interpreting galaxies in the early universe, where high gas densities and elevated $\Sigma_{\rm SFR}$ are more common. As JWST continues to expand the frontier of UV-based abundance studies of galaxies in the reionization era, more deep, high spectral- and spatial-resolution observations are needed to better understand how density and star formation geometry influence chemical yields and interpret the origins and evolution of elemental abundances in the first billion years.

We are grateful for the public data that made this work possible from the HST programs HST-GO-15967 and

DICT CO 15040 that many provided by NACA through

³ HST-GO-15840 that were provided by NASA through a

 $_{4}\;$ grant from the Space Telescope Science Institute, which

5 is operated by the Associations of Universities for Re-

6 search in Astronomy, Incorporated, under NASA con-

 $_{7}$ tract NAS5-26555. This work is based, in part, on obser-

8 vations made with the NASA/ESA/CSA James Webb

9 Space Telescope. We also greatly appreciate the referee

 $_{10}$ for providing thorough feedback that served to notably

improve the clarity of our work.

The HST data used in this paper for Leo P can be found in MAST: 10.17909/kze6-rr69.

Facilities: HST (COS), JWST (NIRSpec)

Software: Cloudy version 23.01 (Chatzikos et al. 2023; Gunasekera et al. 2023), astropy (Astropy Collaboration et al. 2013, 2018, 2022), jupyter (Kluyver et al. 2016), LMFIT version 1.2.2 (Newville et al. 2023), PyNeb version 1.1.18 (Luridiana et al. 2015), BPASS version 2.14 (Eldridge et al. 2017), numpy version 1.24.3 (Harris et al. 2020), scipy version 1.13.1 (Virtanen et al. 2020)

REFERENCES

Abdurro'uf, Larson, R. L., Coe, D., et al. 2024, ApJ, 973, 47, doi: 10.3847/1538-4357/ad6001

Álvarez-Márquez, J., Crespo Gómez, A., Colina, L., et al. 2025, A&A, 695, A250,

doi: 10.1051/0004-6361/202451731

Amayo, A., Delgado-Inglada, G., & Stasińska, G. 2021, MNRAS, 505, 2361, doi: 10.1093/mnras/stab1467

Arellano-Córdova, K. Z., & Rodríguez, M. 2020, MNRAS, 497, 672, doi: 10.1093/mnras/staa1759

Arellano-Córdova, K. Z., Cullen, F., Carnall, A. C., et al. 2025a, MNRAS, 540, 2991, doi: 10.1093/mnras/staf855

Arellano-Córdova, K. Z., Berg, D. A., Mingozzi, M., et al. 2025b, MNRAS, doi: 10.1093/mnras/staf1723

Astropy Collaboration, Robitaille, T. P., Tollerud, E. J., et al. 2013, A&A, 558, A33,

doi: 10.1051/0004-6361/201322068

Astropy Collaboration, Price-Whelan, A. M., Sipőcz, B. M., et al. 2018, AJ, 156, 123, doi: 10.3847/1538-3881/aabc4f

Astropy Collaboration, Price-Whelan, A. M., Lim, P. L., et al. 2022, ApJ, 935, 167, doi: 10.3847/1538-4357/ac7c74

Barchiesi, L., Dessauges-Zavadsky, M., Vignali, C., et al. 2023, A&A, 675, A30, doi: 10.1051/0004-6361/202244838

Berg, D. A., Chisholm, J., Erb, D. K., et al. 2021, ApJ, 922, 170, doi: 10.3847/1538-4357/ac141b

Berg, D. A., Erb, D. K., Auger, M. W., Pettini, M., & Brammer, G. B. 2018, ApJ, 859, 164, doi: 10.3847/1538-4357/aab7fa

Berg, D. A., Erb, D. K., Henry, R. B. C., Skillman, E. D.,
& McQuinn, K. B. W. 2019, ApJ, 874, 93,
doi: 10.3847/1538-4357/ab020a

Berg, D. A., Pogge, R. W., Skillman, E. D., et al. 2020, ApJ, 893, 96, doi: 10.3847/1538-4357/ab7eab

Berg, D. A., Skillman, E. D., Henry, R. B. C., Erb, D. K.,
& Carigi, L. 2016, ApJ, 827, 126,
doi: 10.3847/0004-637X/827/2/126

Berg, D. A., Skillman, E. D., Marble, A. R., et al. 2012, ApJ, 754, 98, doi: 10.1088/0004-637X/754/2/98

Berg, D. A., James, B. L., King, T., et al. 2022, ApJS, 261, 31, doi: 10.3847/1538-4365/ac6c03

Berg, D. A., Skillman, E. D., Chisholm, J., et al. 2024, ApJ, 971, 87, doi: 10.3847/1538-4357/ad5292

Bian, F., Kewley, L. J., & Dopita, M. A. 2018, ApJ, 859, 175, doi: 10.3847/1538-4357/aabd74

Bunker, A. J., Saxena, A., Cameron, A. J., et al. 2023, A&A, 677, A88, doi: 10.1051/0004-6361/202346159

Cameron, A. J., Katz, H., Rey, M. P., & Saxena, A. 2023, MNRAS, 523, 3516, doi: 10.1093/mnras/stad1579

Cardelli, J. A., Clayton, G. C., & Mathis, J. S. 1989, ApJ, 345, 245, doi: 10.1086/167900

- Charbonnel, C., Schaerer, D., Prantzos, N., et al. 2023, A&A, 673, L7, doi: 10.1051/0004-6361/202346410
- Chatzikos, M., Bianchi, S., Camilloni, F., et al. 2023, RMxAA, 59, 327,
 - doi: 10.22201/ia.01851101p.2023.59.02.12
- Cresci, G., Tozzi, G., Perna, M., et al. 2023, A&A, 672, A128, doi: 10.1051/0004-6361/202346001
- Croxall, K. V., Pogge, R. W., Berg, D. A., Skillman, E. D., & Moustakas, J. 2016, ApJ, 830, 4, doi: 10.3847/0004-637X/830/1/4
- Cullen, F., Carnall, A. C., Scholte, D., et al. 2025, arXiv e-prints, arXiv:2501.11099, doi: 10.48550/arXiv.2501.11099
- Davies, R. L., Förster Schreiber, N. M., Genzel, R., et al. 2021, ApJ, 909, 78, doi: 10.3847/1538-4357/abd551
- de Graaff, A., Rix, H.-W., Naidu, R. P., et al. 2025, arXiv e-prints, arXiv:2503.16600,
 - doi: 10.48550/arXiv.2503.16600
- Draine, B. T. 2011, Physics of the Interstellar and Intergalactic Medium (Princeton University Press)
- Edmunds, M. G., & Pagel, B. E. J. 1978, MNRAS, 185, 77P, doi: 10.1093/mnras/185.1.77P
- Eldridge, J. J., Stanway, E. R., Xiao, L., et al. 2017, PASA, 34, e058, doi: 10.1017/pasa.2017.51
- Endsley, R., Stark, D. P., Whitler, L., et al. 2023, MNRAS, 524, 2312, doi: 10.1093/mnras/stad1919
- Fosbury, R. A. E., Villar-Martín, M., Humphrey, A., et al. 2003, ApJ, 596, 797, doi: 10.1086/378228
- García-Benito, R., Díaz, A., Hägele, G. F., et al. 2010, MNRAS, 408, 2234,
 - doi: 10.1111/j.1365-2966.2010.17269.x
- Garnett, D. R. 1990, ApJ, 363, 142, doi: 10.1086/169324
- —. 1992, AJ, 103, 1330, doi: 10.1086/116146
 Gratton, R., et al. 2019, A&A Rv, 27, 8,
- Gratton, R., et al. 2019, A&A Rv, 27, 8, doi: 10.1007/s00159-019-0119-3

doi: 10.3847/2515-5172/ad0e75

- Grazian, A., Giallongo, E., Fiore, F., et al. 2020, ApJ, 897, 94, doi: 10.3847/1538-4357/ab99a3
- Greene, J. E., Strader, J., & Ho, L. C. 2020, ARA&A, 58, 257, doi: 10.1146/annurev-astro-032620-021835
- Groves, B. A., Dopita, M. A., & Sutherland, R. S. 2004, ApJS, 153, 9, doi: 10.1086/421113
- Gunasekera, C. M., van Hoof, P. A. M., Chatzikos, M., & Ferland, G. J. 2023, Research Notes of the American Astronomical Society, 7, 246,
- Hamel-Bravo, M. J., Fisher, D. B., Berg, D., et al. 2024, MNRAS, 530, 3855, doi: 10.1093/mnras/stae983
- Harikane, Y., Sanders, R. L., Ellis, R., et al. 2025, arXiv e-prints, arXiv:2505.09186, doi: 10.48550/arXiv.2505.09186

- Harris, C. R., Millman, K. J., van der Walt, S. J., et al. 2020, Nature, 585, 357, doi: 10.1038/s41586-020-2649-2
- Hayden-Pawson, C., Curti, M., Maiolino, R., et al. 2022, MNRAS, 512, 2867, doi: 10.1093/mnras/stac584
- Hayes, M. J., Saldana-Lopez, A., Citro, A., et al. 2025, ApJ, 982, 14, doi: 10.3847/1538-4357/adaea1
- Henry, R. B. C., Edmunds, M. G., & Köppen, J. 2000, ApJ, 541, 660, doi: 10.1086/309471
- Inayoshi, K., & Maiolino, R. 2025, ApJL, 980, L27, doi: 10.3847/2041-8213/adaebd
- Isobe, Y., Ouchi, M., Nakajima, K., et al. 2023a, ApJ, 956, 139, doi: 10.3847/1538-4357/acf376
- Isobe, Y., Ouchi, M., Tominaga, N., et al. 2023b, ApJ, 959, 100, doi: 10.3847/1538-4357/ad09be
- Izotov, Y. I., Schaerer, D., Worseck, G., et al. 2023, MNRAS, 522, 1228, doi: 10.1093/mnras/stad1036
- James, B. L., Berg, D. A., King, T., et al. 2022, ApJS, 262, 37, doi: 10.3847/1538-4365/ac8008
- Jaskot, A. E., & Ravindranath, S. 2016, ApJ, 833, 136, doi: 10.3847/1538-4357/833/2/136
- Ji, X., Übler, H., Maiolino, R., et al. 2024, MNRAS, 535, 881, doi: 10.1093/mnras/stae2375
- Juan de Dios, L., & Rodríguez, M. 2021, MNRAS, 507, 5331, doi: 10.1093/mnras/stab2488
- Kaasinen, M., Bian, F., Groves, B., Kewley, L. J., & Gupta, A. 2017, MNRAS, 465, 3220, doi: 10.1093/mnras/stw2827
- Katz, H., Saxena, A., Cameron, A. J., et al. 2023, MNRAS, 518, 592, doi: 10.1093/mnras/stac2657
- Kewley, L. J., & Ellison, S. L. 2008, ApJ, 681, 1183, doi: 10.1086/587500
- Kluyver, T., Ragan-Kelley, B., Pérez, F., et al. 2016, in Positioning and Power in Academic Publishing: Players, Agents and Agendas (IOS Press), 87–90, doi: 10.3233/978-1-61499-649-1-87
- Kobayashi, C., & Ferrara, A. 2024, ApJL, 962, L6, doi: 10.3847/2041-8213/ad1de1
- Kobayashi, C., Karakas, A. I., & Lugaro, M. 2020, ApJ, 900, 179, doi: 10.3847/1538-4357/abae65
- Kraft, R. P. 1994, PASP, 106, 553, doi: 10.1086/133416Leitherer, C., Schaerer, D., Goldader, J. D., et al. 1999,
- ApJS, 123, 3, doi: 10.1086/313233
- Luridiana, V., Morisset, C., & Shaw, R. A. 2012, in Planetary Nebulae: An Eye to the Future, Vol. 283, 422–423, doi: 10.1017/S1743921312011738
- Luridiana, V., Morisset, C., & Shaw, R. A. 2015, A&A, 573, A42, doi: 10.1051/0004-6361/201323152
- Maiolino, R., Scholtz, J., Witstok, J., et al. 2024, Nature, 627, 59, doi: 10.1038/s41586-024-07052-5
- Marconcini, C., D'Eugenio, F., Maiolino, R., et al. 2024, MNRAS, 533, 2488, doi: 10.1093/mnras/stae1971

Marques-Chaves, R., Schaerer, D., Kuruvanthodi, A., et al. 2024, A&A, 681, A30, doi: 10.1051/0004-6361/202347411

- Martins, F., Schaerer, D., Marques-Chaves, R., & Upadhyaya, A. 2023, A&A, 678, A159, doi: 10.1051/0004-6361/202346732
- Maseda, M. V., Brinchmann, J., Franx, M., et al. 2017, A&A, 608, A4, doi: 10.1051/0004-6361/201730985
- Matthee, J., Mackenzie, R., Simcoe, R. A., et al. 2023, ApJ, 950, 67, doi: 10.3847/1538-4357/acc846
- McClymont, W., Tacchella, S., D'Eugenio, F., et al. 2025, MNRAS, 540, 190, doi: 10.1093/mnras/staf745
- McQuinn, K. B. W., Skillman, E. D., Dolphin, A., et al. 2015, ApJ, 812, 158, doi: 10.1088/0004-637X/812/2/158
- Méndez-Delgado, J. E., Esteban, C., García-Rojas, J., et al. 2023, MNRAS, 523, 2952, doi: 10.1093/mnras/stad1569
- Meštrić, U., Vanzella, E., Upadhyaya, A., et al. 2023, A&A, 673, A50, doi: 10.1051/0004-6361/202345895
- Milone, A. P., & Marino, A. F. 2022, Universe, 8, 359, doi: 10.3390/universe8070359
- Mingozzi, M., James, B. L., Arellano-Córdova, K. Z., et al. 2022, ApJ, 939, 110, doi: 10.3847/1538-4357/ac952c
- Naidu, R. P., Matthee, J., Katz, H., et al. 2025, arXiv e-prints, arXiv:2503.16596, doi: 10.48550/arXiv.2503.16596
- Nandal, D., Regan, J. A., Woods, T. E., et al. 2024a, A&A, 683, A156, doi: 10.1051/0004-6361/202348035
- Nandal, D., Sibony, Y., & Tsiatsiou, S. 2024b, A&A, 688, A142, doi: 10.1051/0004-6361/202348866
- Nandal, D., Whalen, D. J., Latif, M. A., & Heger, A. 2025, arXiv e-prints, arXiv:2502.04435, doi: 10.48550/arXiv.2502.04435
- Nava, A., Casebeer, D., Henry, R. B. C., & Jevremovic, D. 2006, ApJ, 645, 1076, doi: 10.1086/504416
- Newville, M., Otten, R., Nelson, A., et al. 2023, lmfit/lmfit-py: 1.2.2, 1.2.2, Zenodo, doi: 10.5281/zenodo.8145703
- Nicholls, D. C., Sutherland, R. S., Dopita, M. A., Kewley, L. J., & Groves, B. A. 2017, MNRAS, 466, 4403, doi: 10.1093/mnras/stw3235
- Osterbrock, D. E. 1989, Astrophysics of gaseous nebulae and active galactic nuclei (University Science Books)
- Osterbrock, D. E., & Ferland, G. J. 2006, Astrophysics of gaseous nebulae and active galactic nuclei (University Science Books)
- Parker, K. S., Berg, D. A., Chisholm, J., et al. 2025,CLASSY XIII: Cutting through the Clouds ComparingIndirect Tracers of Ionizing Photon Escape
- Pascale, M., Dai, L., McKee, C. F., & Tsang, B. T. H. 2023, ApJ, 957, 77, doi: 10.3847/1538-4357/acf75c

- Peimbert, M. 1971, Boletin de los Observatorios Tonantzintla y Tacubaya, 6, 29
- Peimbert, M., & Costero, R. 1969, Boletin de los Observatorios Tonantzintla y Tacubaya, 5, 3
- Pérez-Montero, E., García-Benito, R., Vílchez, J. M., et al. 2016, A&A, 595, A62, doi: 10.1051/0004-6361/201628601
- Pilyugin, L. S., Grebel, E. K., & Mattsson, L. 2012, MNRAS, 424, 2316,
 - doi: 10.1111/j.1365-2966.2012.21398.x
- Pilyugin, L. S., Mattsson, L., Vílchez, J. M., & Cedrés, B. 2009, MNRAS, 398, 485,
 - doi: 10.1111/j.1365-2966.2009.15182.x
- Reddy, N. A., Steidel, C. C., Pettini, M., & Bogosavljević, M. 2016, ApJ, 828, 107, doi: 10.3847/0004-637X/828/2/107
- Reddy, N. A., Topping, M. W., Sanders, R. L., Shapley,
 A. E., & Brammer, G. 2023, ApJ, 952, 167,
 doi: 10.3847/1538-4357/acd754
- Rickards Vaught, R. J., Sandstrom, K. M., Belfiore, F., et al. 2024, ApJ, 966, 130, doi: 10.3847/1538-4357/ad303c
- Rickards Vaught, R. J., Hunt, L. K., Aloisi, A., et al. 2025, arXiv e-prints, arXiv:2507.12222, doi: 10.48550/arXiv.2507.12222
- Rigby, J. R., Florian, M., Acharyya, A., et al. 2021, ApJ, 908, 154, doi: 10.3847/1538-4357/abcfc9
- Rivera-Thorsen, T. E., Chisholm, J., Welch, B., et al. 2024, A&A, 690, A269, doi: 10.1051/0004-6361/202450359
- Rogers, N. S. J., Skillman, E. D., Pogge, R. W., et al. 2022, ApJ, 939, 44, doi: 10.3847/1538-4357/ac947d
- —. 2021, ApJ, 915, 21, doi: 10.3847/1538-4357/abf8b9
- Rubin, R. H. 1989, ApJS, 69, 897, doi: 10.1086/191330
- Rusakov, V., Watson, D., Nikopoulos, G. P., et al. 2025, arXiv e-prints, arXiv:2503.16595, doi: 10.48550/arXiv.2503.16595
- Sanders, R. L., Shapley, A. E., Kriek, M., et al. 2016, ApJL, 825, L23, doi: 10.3847/2041-8205/825/2/L23
- Sanders, R. L., Shapley, A. E., Reddy, N. A., et al. 2020, MNRAS, 491, 1427, doi: 10.1093/mnras/stz3032
- Sanders, R. L., Shapley, A. E., Clarke, L., et al. 2023, ApJ, 943, 75, doi: 10.3847/1538-4357/aca9cc
- Scarlata, C., Hayes, M., Panagia, N., et al. 2024, arXiv e-prints, arXiv:2404.09015, doi: 10.48550/arXiv.2404.09015
- Schaerer, D., Marques-Chaves, R., Xiao, M., & Korber, D. 2024, A&A, 687, L11, doi: 10.1051/0004-6361/202450721
- Scholte, D., Cullen, F., Carnall, A. C., et al. 2025, MNRAS, 540, 1800, doi: 10.1093/mnras/staf834
- Seaton, M. J., & Osterbrock, D. E. 1957, ApJ, 125, 66, doi: 10.1086/146282

- Senchyna, P., Plat, A., Stark, D. P., et al. 2024, ApJ, 966, 92, doi: 10.3847/1538-4357/ad235e
- Shimakawa, R., Kodama, T., Steidel, C. C., et al. 2015, MNRAS, 451, 1284, doi: 10.1093/mnras/stv915
- Skillman, E. D., Salzer, J. J., Berg, D. A., et al. 2013, AJ, 146, 3, doi: 10.1088/0004-6256/146/1/3
- Sneden, C., et al. 1991, AJ, 102, 2001, doi: 10.1086/116023
 Stanton, T. M., Cullen, F., Carnall, A. C., et al. 2025,
 MNRAS, 537, 1735, doi: 10.1093/mnras/staf106
- Stasińska, G. 2023, arXiv e-prints, arXiv:2312.01873, doi: 10.48550/arXiv.2312.01873
- Strom, A. L., Steidel, C. C., Rudie, G. C., et al. 2017, ApJ, 836, 164, doi: 10.3847/1538-4357/836/2/164
- Tacchella, S., Eisenstein, D. J., Hainline, K., et al. 2023, ApJ, 952, 74, doi: 10.3847/1538-4357/acdbc6
- Telford, O. G., McQuinn, K. B. W., Chisholm, J., & Berg, D. A. 2023, ApJ, 943, 65, doi: 10.3847/1538-4357/aca896
- Topping, M. W., Stark, D. P., Senchyna, P., et al. 2024, MNRAS, 529, 3301, doi: 10.1093/mnras/stae682
- Topping, M. W., Sanders, R. L., Shapley, A. E., et al. 2025a, MNRAS, 541, 1707, doi: 10.1093/mnras/staf903
- Topping, M. W., Stark, D. P., Senchyna, P., et al. 2025b, ApJ, 980, 225, doi: 10.3847/1538-4357/ada95c
- Übler, H., Maiolino, R., Curtis-Lake, E., et al. 2023, A&A, 677, A145, doi: 10.1051/0004-6361/202346137

- van Zee, L., & Haynes, M. P. 2006, ApJ, 636, 214, doi: 10.1086/498017
- Vanzella, E., Grazian, A., Hayes, M., et al. 2010, A&A, 513, A20, doi: 10.1051/0004-6361/200913042
- Vanzella, E., Castellano, M., Bergamini, P., et al. 2022, A&A, 659, A2, doi: 10.1051/0004-6361/202141590
- Villar-Martín, M., Cerviño, M., & González Delgado, R. M. 2004, MNRAS, 355, 1132,
 - doi: 10.1111/j.1365-2966.2004.08395.x
- Virtanen, P., Gommers, R., Oliphant, T. E., et al. 2020, Nature Methods, 17, 261, doi: 10.1038/s41592-019-0686-2
- Welch, B., Olivier, G. M., Hutchison, T. A., et al. 2024, ApJ, 975, 196, doi: 10.3847/1538-4357/ad79ec
- Welch, B., Rivera-Thorsen, T. E., Rigby, J. R., et al. 2025, ApJ, 980, 33, doi: 10.3847/1538-4357/ada76c
- Wheeler, J. C., Sneden, C., & Truran, James W., J. 1989, ARA&A, 27, 279,
 - doi: 10.1146/annurev.aa.27.090189.001431
- Xu, X., Heckman, T., Henry, A., et al. 2022, ApJ, 933, 222, doi: 10.3847/1538-4357/ac6d56
- Yanagisawa, H., Ouchi, M., Nakajima, K., et al. 2024, ApJ, 974, 180, doi: 10.3847/1538-4357/ad7097
- Zhang, Y., Morishita, T., & Stiavelli, M. 2025, arXiv e-prints, arXiv:2502.04817,
 - doi: 10.48550/arXiv.2502.04817

APPENDIX

A. REST-UV LEO P SPECTRUM

We present the co-added spectrum of the local extremely metal-poor galaxy Leo P (Skillman et al. 2013). This process is described briefly in Section 2.1. We followed the steps outlined in Berg et al. (2022) in order to combine the high-resolution grating from Telford et al. (2023) and the low-resolution grating obtained in HST-GO-17102. This final spectrum can be found in 17, and we label the crucial emission lines in this spectrum that were used in this work.

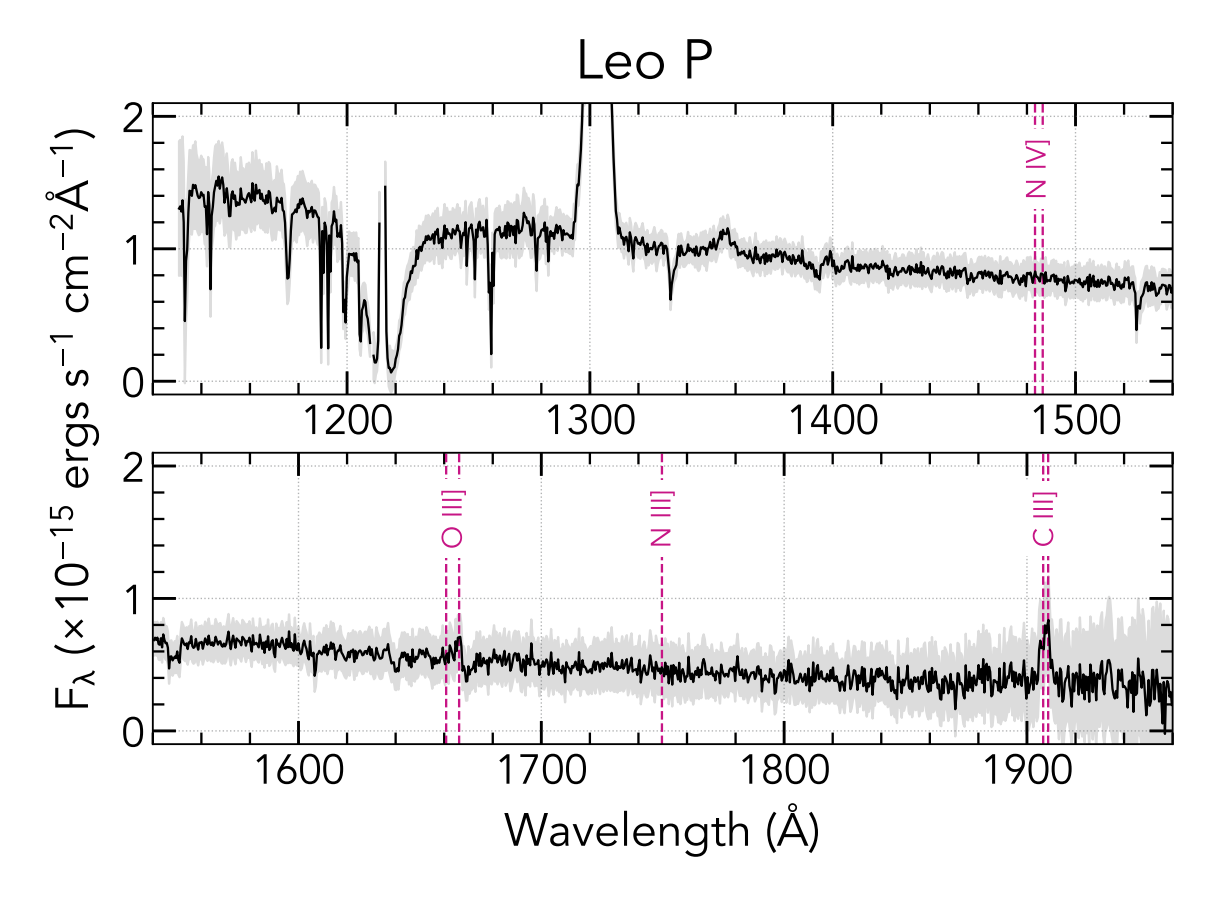


Figure 17. Final co-added rest-UV spectrum for the Leo P. We combined the high-resolution G130M and G160M gratings from Telford et al. (2023) and the G140L grating from HST-GO-17102 to obtain wavelength coverage of all key emission lines used in this study. The pink dashed lines highlight the location of these key emission lines in the rest-UV spectrum of Leo P.

B. EMISSION LINE MEASUREMENTS

We present the emission line measurements for both the low-z and high-z samples presented in this work. We discuss the fitting procedure for emission lines that we measure in this work and the selection requirement for the emission lines taken from literature sources in Section 3. The dereddened relative intensities utilized in this work are presented in Tables 6 and 7. All optical emission lines are dereddened according to Cardelli et al. (1989), while the UV emission lines are dereddened using Reddy et al. (2016). For the low-z sample, we present our rest-UV intensities relative to I(C III]) and our rest-optical intensities relative to $I(H\beta)$. However, in our high-z sample all of the intensities that we present are given relative to $I(H\beta)$.

Table 6. Rest UV+Optical Emission Lines for the Low-z Sample

| Line | J0127- 0619 | J1314+ 3452 | J1444+ 4237 | Leo P | J1253- 0312 | J1044+ 0353 | J1323- 0132 | J1545+ 0858 |
|---------------------------------------|--------------------|---------------------|---------------------|---------------------------------|---------------------|---------------------|--------------------|--------------------|
| - | | | I | $(\lambda)/I(\text{C III}])$ | | | | |
| N IV] λ1483.32 | | | | | 1.10 ± 0.35 | 1.01 ± 0.17 | 4.19±0.64 | 1.25±0.32 |
| N IV] $\lambda 1486.50$ | | | | | 1.29 ± 0.36 | $0.53 {\pm} 0.16$ | 2.79 ± 0.57 | 1.42 ± 0.35 |
| O III] $\lambda 1661.81$ | 1.05 ± 1.06 | 4.75 ± 1.11 | 12.51 ± 2.54 | $8.36 {\pm} 1.53$ | 5.10 ± 0.66 | 17.08 ± 0.77 | $20.46 {\pm} 2.08$ | 13.08 ± 0.97 |
| O III] $\lambda 1666.15$ | 5.62 ± 1.19 | | | 15.51 ± 2.51 | 16.62 ± 0.92 | 39.73 ± 1.74 | $49.89 {\pm} 4.88$ | 30.59 ± 1.68 |
| N 111] $\lambda 1750.00^{\dagger}$ | $42.92{\pm}2.48$ | 4.07 ± 1.06 | 2.29 ± 0.90 | 7.69 ± 2.49 | | | | |
| [C III] $\lambda 1906.68$ | 61.72 ± 3.02 | 57.17 ± 4.85 | $55.63{\pm}15.89$ | 37.15 ± 8.54 | 56.47 ± 3.43 | 59.00 ± 4.11 | $62.68 {\pm} 9.50$ | 53.60 ± 4.32 |
| _ C III] $\lambda 1908.73$ | $38.28 {\pm} 2.51$ | 42.83 ± 4.33 | $44.37 {\pm} 14.22$ | $62.85 {\pm} 11.15$ | 43.53 ± 3.13 | 41.00 ± 3.42 | 37.32 ± 7.33 | 46.40 ± 4.00 |
| | | | - | $I(\lambda)/I(\mathrm{H}\beta)$ | | | | |
| [O II] $\lambda 3727.10$ | | | | 46.51 ± 3.93 | 89.93 ± 0.89 | 9.60 ± 0.18 | 18.66 ± 0.16 | 63.90 ± 0.10 |
| [O II] $\lambda 3729.88$ | | | | | | $16.77 {\pm} 0.29$ | | |
| $H\gamma \lambda 4341.68$ | $42.78 {\pm} 0.65$ | 52.29 ± 0.38 | 45.77 ± 1.27 | 45.19 ± 1.44 | 47.41 ± 0.45 | $46.55 {\pm} 0.83$ | 46.62 ± 0.11 | 47.17 ± 0.05 |
| [O III] $\lambda 4364.44$ | $9.15 {\pm} 0.34$ | $5.46 {\pm} 0.10$ | $6.49 {\pm} 0.96$ | $3.80 {\pm} 0.51$ | 11.15 ± 0.13 | $13.51 {\pm} 0.25$ | $20.35 {\pm} 0.08$ | $13.42 {\pm} 0.04$ |
| [Ar IV] $\lambda 4712.67$ | | $0.47 {\pm} 0.05$ | | $0.94 {\pm} 0.38$ | 1.74 ± 0.05 | $164.99{\pm}6.24$ | 4.05 ± 0.06 | 1.42 ± 0.03 |
| [Ar IV] $\lambda 4741.53$ | | $0.32 {\pm} 0.04$ | < 2.49 | $0.08 {\pm} 0.02$ | $1.35 {\pm} 0.05$ | 115.99 ± 2.34 | 3.07 ± 0.06 | 1.26 ± 0.03 |
| $^{\mathrm{H}\beta}$ $\lambda4862.68$ | 100.00 ± 1.11 | 100.00 ± 0.61 | 100.00 ± 1.66 | 100.00 ± 2.91 | 100.00 ± 0.81 | 100.00 ± 1.49 | 100.00 ± 0.16 | 100.00 ± 0.08 |
| [O III] $\lambda 5008.24$ | 353.51 ± 2.96 | 582.27 ± 3.32 | 241.95 ± 3.21 | 145.26 ± 4.31 | 683.70 ± 8.85 | $427.48\!\pm\!6.22$ | 720.74 ± 0.83 | 559.06 ± 0.32 |
| $H\alpha \lambda 6564.61$ | $340.24{\pm}4.39$ | $282.45\!\pm\!1.65$ | 280.59 ± 3.59 | $274.92 \!\pm\! 11.06$ | $277.80\!\pm\!2.25$ | $296.70\!\pm\!5.23$ | 279.63 ± 0.32 | 265.06 ± 0.15 |
| [N II] $\lambda 6585.27$ | 22.10 ± 0.58 | 10.28 ± 0.07 | $4.58 {\pm} 0.65$ | $2.51 {\pm} 0.50$ | 14.28 ± 0.13 | $0.81 {\pm} 0.01$ | 1.39 ± 0.01 | 2.43 ± 0.01 |
| [S II] $\lambda 6718.29$ | 18.72 ± 0.20 | 12.88 ± 0.09 | 13.69 ± 0.69 | 3.60 ± 0.31 | 7.91 ± 0.07 | $2.50 {\pm} 0.05$ | 1.79 ± 0.02 | 5.54 ± 0.01 |
| [S II] $\lambda 6732.67$ | 17.07 ± 0.18 | 10.48 ± 0.08 | 9.01 ± 0.66 | 2.70 ± 0.31 | 7.35 ± 0.08 | 2.04 ± 0.05 | $1.68 {\pm} 0.01$ | 4.37 ± 0.01 |
| [Ar III] $\lambda 7137.77$ | 11.02 ± 0.17 | 9.04 ± 0.07 | $2.86{\pm}0.62$ | $2.60 {\pm} 0.21$ | 7.91 ± 0.07 | 241.99 ± 9.35 | 3.11 ± 0.02 | 4.07 ± 0.01 |
| [O II] $\lambda 7320.94$ | $4.20 {\pm} 0.17$ | $2.35 {\pm} 0.04$ | < 2.03 | $0.60 {\pm} 0.20$ | | 0.60 ± 0.02 | | |
| [O II] λ7331.68 | $3.54{\pm}0.17$ | 2.02 ± 0.03 | < 2.10 | $0.70 {\pm} 0.20$ | | $0.48 {\pm} 0.07$ | | |
| E(B-V) | 0.298 | 0.140 | 0.081 | 0.063 | 0.158 | 0.039 | 0.128 | 0.110 |
| $F_{ m C~III]}$ | $70.68 {\pm} 2.24$ | 21.38 ± 1.13 | 15.39 ± 2.67 | 1.75 ± 0.20 | 89.15 ± 3.37 | 27.28 ± 1.19 | 11.92 ± 1.16 | $33.44 {\pm} 1.61$ |
| $F_{\mathrm{H}\beta}$ | $423.38{\pm}3.33$ | 82.79 ± 0.36 | $2.47{\pm}0.03$ | $3.40{\pm}0.07$ | 189.77 ± 1.09 | $95.20{\pm}1.00$ | $10.38 {\pm} 0.01$ | 32.48 ± 0.0 . |

Note—Reddening-corrected emission-line intensities adopted for the Low-z Sample. The UV and optical fluxes are given relative to $F_{\rm C~III]} \times 100$ and $F_{\rm H\beta} \times 100$, respectively. The last three rows give the dust extinction using the Cardelli et al. (1989) reddening law and the observed C III] and H β fluxes, in units of 10^{-15} erg s⁻¹ cm⁻².

 $^{^\}dagger N$ III] $\lambda 1750$ is the integrated flux of the N III] $\lambda \lambda 1746,1748,1749,1752,1754$ quintuplet.

Table 7. Rest UV+Optical Emission Lines for the High-z Sample

| | XC 8-ID GN-z11 | GDS 3073 | | J1723+ | CEERS | CI OC | | 1.1500 |
|---|-----------------------------|--------------------|------------------|----------------------|--------------------|--|--------------------|----------------------|
| | | | Sunburst | 3411 | 1019 | $\begin{array}{c} \mathrm{SL2S} \\ \mathrm{J0217} \end{array}$ | Lynx | A1703- zd6 |
| | | | $I(\lambda)/I(1$ | $H\beta$) | | | | |
| N IV] λ1483.32 33.9 | ±1.6 7.3±1.4 | 52.6±9.3 | | | 103.2 ± 19.6 | | 17.2 ± 2.8 | 17.7±5.9 |
| N IV] λ1486.50 81.9 | ± 2.4 47.5 ± 9.2 | 245.9 ± 10.6 | | | 206.1 ± 26.8 | | 24.4 ± 2.9 | 37.6 ± 5.1 |
| Ο ΙΙΙ] λ1666.15 66.1 | ± 1.3 16.1 ± 6.2 | 13.5 ± 3.2 | 5.8 ± 0.6 | 3.9 ± 0.8 | $89.2 {\pm} 19.7$ | 11.1 ± 0.4 | 37.8 ± 3.0 | 60.6 ± 6.0 |
| N III] $\lambda 1750.00^{\dagger}$ 17.7 | ± 1.6 74.2 ± 13.3 | 99.1 ± 3.9 | 6.8 ± 1.0 | < 0.8 | 54.0 ± 22.9 | $0.8 {\pm} 0.2$ | 17.8 ± 2.8 | $21.4 {\pm} 6.8$ |
| [C III] $\lambda 1906.68$ 27.2 | ± 1.2 | | 7.3 ± 0.5 | 13.2 ± 1.1 | | 15.3 ± 0.5 | 35.0 ± 2.9 | 17.7 ± 4.6 |
| C III] $\lambda 1908.73$ 60.2 | ± 1.6 56.4 ± 9.1 | 94.1 ± 1.9 | $14.5 {\pm} 1.2$ | $9.3 {\pm} 0.8$ | 170.6 ± 30.8 | 10.1 ± 0.3 | 24.2 ± 2.9 | $35.8 {\pm} 5.7$ |
| [O II] $\lambda 3727.10$. | | | $34.5 {\pm} 6.0$ | 55.9 ± 2.1 | 33.9 ± 4.7 | | | |
| [O II] $\lambda 3729.88$ 4.3 | ±1.6 47.8±7.8 | 21.8 ± 0.6 | $25.7 {\pm} 6.7$ | 76.9 ± 2.6 | 34.6 ± 4.8 | | <25.0 | < 17.7 |
| $H\gamma \lambda 4341.68 47.3$ | ± 0.5 47.3 ± 9.1 | 47.3 ± 0.4 | 47.3 ± 0.7 | 47.3 ± 1.9 | $54.7 {\pm} 11.4$ | 47.3 ± 1.9 | 47.3 ± 1.9 | 47.3 ± 2.7 |
| [O III] $\lambda 4364.44$ 42.1 | ± 0.9 14.0 ± 7.8 | 15.1 ± 0.6 | 11.6 ± 6.4 | 2.0 ± 4.3 | $20.8 {\pm} 6.3$ | $6.7 {\pm} 4.1$ | | 34.6 ± 3.4 |
| ${ m H}eta \ \lambda 4862.68 \ 100.0$ | 0 ± 1.1 100.0 ± 19.3 | 100.0 ± 0.7 | 100.0 ± 1.4 | 100.0 ± 4.0 | 100.0 ± 14.5 | 100.0 ± 4.1 | 100.0 ± 3.9 | 100.0 ± 5.6 |
| [O III] λ5008.24 657.1 | ± 5.2 561.2 ± 121 . | 377.7 ± 2.1 | 697.6 ± 56.3 | $544.6 \!\pm\! 17.2$ | $646.7 {\pm} 67.7$ | $309.5 {\pm} 10.4$ | $750.0\!\pm\!21.0$ | $635.5 {\pm} 26.3$ |
| $H\alpha \ \lambda 6564.61 \ 254.7$ | 7 ± 2.2 277.8 ± 53.6 | $5 279.7 \pm 1.6$ | 300.4 ± 25.0 | 288.4 ± 9.8 | 277.8 ± 40.4 | $277.8 \!\pm\! 11.5$ | 277.8 ± 10.9 | $277.8 \!\pm\! 15.6$ |
| [N II] λ6585.27 6.3 | ±0.8 | < 3.2 | 9.9 ± 1.1 | 17.9 ± 0.6 | | | | |
| [S II] $\lambda 6718.29$. | | 1.1 ± 0.6 | 3.7 ± 0.5 | | | | | |
| [S II] $\lambda 6732.67$. | | $1.7 {\pm} 0.7$ | 4.0 ± 0.5 | | | | | |
| E(B-V) . | | 0.156 | 0.110 | 0.028 | 0.120 | | | |
| $F_{\mathrm{H}\beta}$ 25.4 | ± 0.2 18.6 ± 2.5 | 37.9 ± 0.2 | 100.0 ± 1.0 | 142.0 ± 4.0 | $2.1 {\pm} 0.2$ | 78.9 ± 2.3 | $3.6 {\pm} 0.1$ | $32.7 {\pm} 1.3$ |

Note—Reddening-corrected emission-line intensities adopted for the High-z Sample. The fluxes are given relative to $F_{\rm H\beta} \times 100$. The last two rows give the dust extinction using the Cardelli et al. (1989) reddening law and the observed H β fluxes, in units of 10^{-16} erg s⁻¹ cm⁻².

†N III] $\lambda 1750$ is the integrated flux of the N III] $\lambda \lambda 1746,1748,1749,1752,1754$ quintuplet.

^{*}H β λ 4862 is not covered in the spectrum of GN-z11; instead, the H β flux was inferred from the measured H γ flux.

C. O⁺²/O⁺ IONIZATION PARAMETER DIAGNOSTIC FIT

We present another n_e -insensitive diagnostic for $\log U$ using the relative ionic abundance, ${\rm O}^{+2}/{\rm O}^+$. This probe is useful when there is not access to the lines necessary to utilize ${\rm N}_{43}$ as a diagnostic that is robust to n_e or in the event it is not possible to appropriately characterize the entire n_e structure. We used the functional form $f(x,y) = A + Bx + Cy + Dxy + Ex^2 + Fy^2 + Gxy^2 + Hyx^2 + Ix^3 + Jy^3$ to fit a bicubic surface to the ${\rm O}^{+2}/{\rm O}^+$ – $\log U$ relationship for n_e ranging from 10^2 to 10^6 cm⁻³ using the same procedure outlined in Section 5.5.1. While the left panel of Figure 18, we present a 3D plot of our fits along with the models color coded by n_e , the right panel shows a 2D projection of the fits at $n_e = 10^2$ and 10^6 cm⁻³, where the color bar indicates the metallicity. Figure 18 shows that the modeled relationship between ${\rm O}^{+2}/{\rm O}^+$ – $\log U$ is very insensitive to n_e , especially at $n_e \gtrsim 10^3$ cm⁻³.

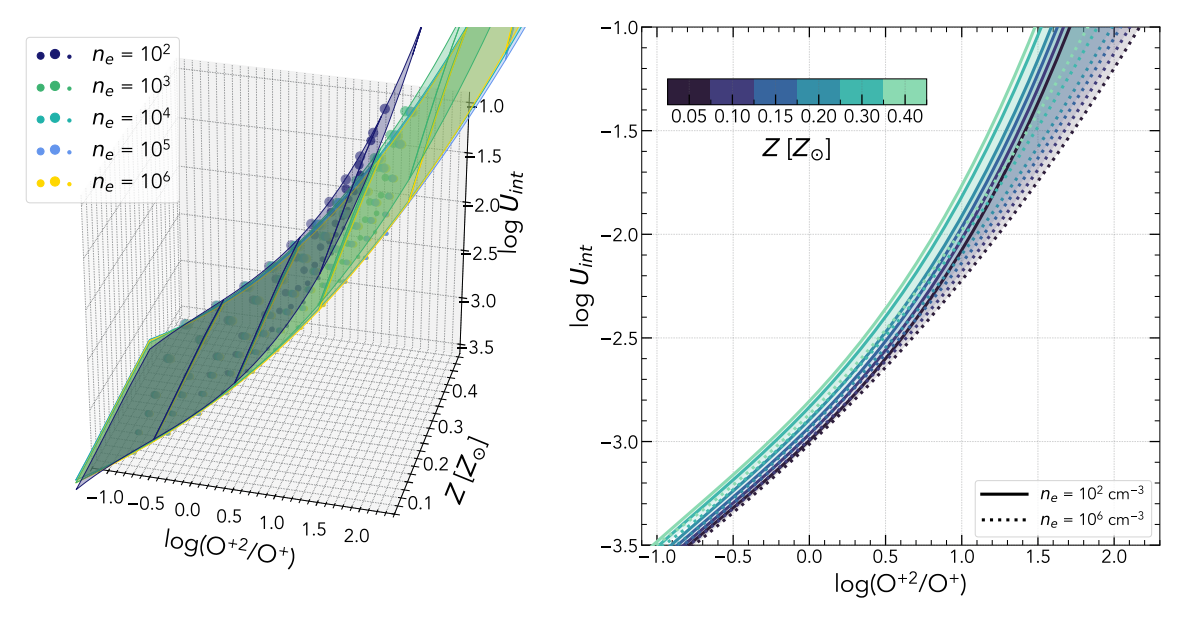


Figure 18. The cloudy model relationship between O^{+2}/O^+ and $\log U$. The left panel shows 3D plots of the bicubic fits for each grid of models, and the marker color denotes n_e ranging from $10^2 - 10^6$ cm⁻³. In the right panel, we show a 2D projection where the range of n_e is shown by the shaded region. The metallicities range between $0.05 Z_{\odot}$ and $0.40 Z_{\odot}$ as indicated by the color bar in the upper right plot. Additionally, the solid lines shows the fits at $n_e = 10^2$ cm⁻³ and the dotted lines mark where the fits are at $n_e = 10^6$ cm⁻³. The effect of n_e on O^{+2}/O^+ is minimal making this probe of $\log U$ extremely robust.

 Table 8. Ionization Parameter Fits

| | | | $n_e (cm^{-3})$ | | |
|-----------|------------------|-----------------------|-------------------|----------|----------|
| | 10^{2} | 10^{3} | 10^{4} | 10^{5} | 10^{6} |
| z = f(z) | $(x,y) = \log U$ | $J_{int}; x = \log x$ | $g(O^{+2}/O^{+})$ | ; y = Z | |
| $A \dots$ | -3.01893 | -3.02826 | -3.03228 | -3.03319 | -3.03090 |
| $B \dots$ | 0.68142 | 0.67769 | 0.68678 | 0.68770 | 0.68578 |
| $C \dots$ | 0.39134 | 0.47521 | 0.47450 | 0.41954 | 0.30140 |
| $D \dots$ | 0.40444 | 0.36650 | 0.36517 | 0.34904 | 0.25356 |
| $E \dots$ | 0.13516 | 0.08499 | 0.08376 | 0.08278 | 0.07391 |
| $F \dots$ | 1.93922 | 1.24708 | 1.01559 | 1.14266 | 1.42633 |
| $G \dots$ | -0.38687 | -0.37495 | -0.41327 | -0.39662 | -0.25902 |
| H | 0.11450 | 0.10476 | 0.11398 | 0.11960 | 0.13938 |
| $I \dots$ | 0.07717 | 0.02243 | 0.00769 | 0.00657 | 0.01181 |
| $J \dots$ | -3.95339 | -2.87921 | -2.47978 | -2.61133 | -2.90696 |

Note— The bicubic surface fit to Cloudy photoionization models for the ionization parameters are parameterized by the following equation: $f(x,y) = A + Bx + Cy + Dxy + Ex^2 + Fy^2 + Gxy^2 + Hyx^2 + Ix^3 + Jy^3.$

D. TOTAL AND RELATIVE IONIC ABUNDANCE MEASUREMENTS

We present the total and relative ionic abundances for every galaxy in our low-z and high-z samples in Tables 9 and 10. Additionally, each of these tables contains the n_e , T_e , and $\log U$ derived to determine each set of abundances. We clarify the ionization zone that each measurement traces for every property that we present. We outline the procedure for deriving all of these properties in Section 6.

Table 9. Ionic and Total N Abundances for Low-z Sample

| | Model | Ion. Zone $T_e \mid n_e$ | J0127- 0619 | J1314+ 3452 | J1444+ 4237 | Leo P | J1253- 0312 | J1044+ 0353 | J1323- 0132 | J1545+ 0858 |
|---|--------|--------------------------|--------------------|--------------------|--------------------|--------------------|--------------------|--------------------|--------------------|--------------------|
| Densities (cm^{-3}) : | | | | | | | | | | |
| $n_{e,low}(\mathrm{S}^+)(\times 10^2)$ | Both | r | 3.8 ± 0.1 | 1.9 ± 0.1 | < 0.3 | 0.8 ± 0.6 | 4.2 ± 0.1 | 2.0 ± 0.2 | 4.4 ± 0.1 | 1.5 ± 0.1 |
| $n_{e,int.}(C^{+2})(\times 10^3)$ | Multi | <u> </u> | < 0.7 | 5.8 ± 2.2 | 8.8 ± 6.8 | 64.4 ± 14.7 | 7.1 ± 2.1 | 2.4 ± 1.4 | < 0.7 | 13.0 ± 2.8 |
| $n_{e,high}(\mathbf{N}^{+3})(\times 10^4)$ | Multi | H | 0.2 | 2.0 | 3.0 | 88.8 | 6.5 ± 3.8 | < 0.4 | < 0.4 | 6.0 ± 3.0 |
| Temperatures (K): | | | | | | | | | | |
| $T_{e,low}(imes 10^4)^a$ | Uni. | $\frac{\Gamma}{\Gamma}$ | 1.50 ± 0.01 | 1.08 ± 0.01 | 1.52 ± 0.06 | 1.50 ± 0.06 | 1.27 ± 0.01 | 1.64 ± 0.01 | 1.55 ± 0.01 | 1.46 ± 0.01 |
| $T_{e,high}(O^{+2})(\times 10^4)$ | Uni. | $H \mid L$ | 1.71 ± 0.02 | 1.12 ± 0.01 | 1.74 ± 0.09 | 1.72 ± 0.08 | 1.38 ± 0.01 | 1.91 ± 0.01 | 1.79 ± 0.01 | 1.65 ± 0.01 |
| $T_{e,low}(\times 10^4)^b$ | Multi | Г Н | 1.50 ± 0.01 | 1.08 ± 0.01 | 1.52 ± 0.06 | 1.50 ± 0.03 | 1.27 ± 0.01 | 1.64 ± 0.01 | 1.55 ± 0.01 | 1.46 ± 0.01 |
| $T_{e,int.}(\times 10^4)^c$ | Multi | н п | 1.59 ± 0.02 | 1.07 ± 0.01 | 1.55 ± 0.07 | 1.27 ± 0.04 | 1.22 ± 0.01 | 1.75 ± 0.01 | 1.65 ± 0.01 | 1.42 ± 0.01 |
| $T_{e,high}({\rm O}^{+2})(\times 10^4)$ | Multi | н н | 1.71 ± 0.02 | 1.09 ± 0.01 | 1.66 ± 0.08 | 1.32 ± 0.05 | 1.27 ± 0.01 | 1.90 ± 0.01 | 1.78 ± 0.01 | 1.51 ± 0.01 |
| Ionization Parameters: | ters: | | | | | | | | | |
| $\log U_{int.}({ m O}_{32})$ | Uni. | LH | -2.724 | -2.256 | -2.736 | -2.612 | -1.857 | -1.619 | -1.000 | -1.952 |
| $\log U_{high}({ m N}_{43})$ | Multi | ΗI | : | -1.738 | -1.745 | -1.979 | -1.280 | -1.563 | -1.075 | -1.619 |
| Ionic and Total O Abundances: | Abunda | ances: | | | | | | | | |
| $O^+/H^+(\times 10^{-5})$ | Both | $\Gamma \mid \Gamma$ | 1.677 ± 0.074 | 5.408 ± 0.345 | < 1.064 | 0.384 ± 0.061 | 1.367 ± 0.042 | 0.170 ± 0.004 | 0.149 ± 0.003 | 0.581 ± 0.011 |
| $O^{+2}/H^+(\times 10^{-5})$ | Uni. | H L | 2.825 ± 0.069 | 14.589 ± 0.417 | 1.865 ± 0.164 | 1.149 ± 0.121 | 9.325 ± 0.226 | 2.682 ± 0.046 | 5.192 ± 0.067 | 4.870 ± 0.074 |
| $O^{+2}/H^+(\times 10^{-5})$ | Multi | н н | 2.816 ± 0.090 | 16.087 ± 0.569 | 2.133 ± 0.271 | 2.878 ± 0.355 | 12.641 ± 0.843 | 2.703 ± 0.056 | 5.249 ± 0.074 | 6.454 ± 0.339 |
| $12 + \log(O/H)$ | Uni. | All L | 7.653 ± 0.010 | 8.301 ± 0.012 | < 7.483 | 7.185 ± 0.037 | 8.029 ± 0.009 | 7.455 ± 0.007 | 7.728 ± 0.005 | 7.736 ± 0.006 |
| $12 + \log(O/H)$ | Multi | All | 7.653 ± 0.011 | 8.345 ± 0.014 | < 7.487 | 7.561 ± 0.042 | 8.157 ± 0.025 | 7.459 ± 0.008 | 7.732 ± 0.006 | 7.856 ± 0.020 |
| Ionic and Relative N Abundances | N Abu | ındances: | | | | | | | | |
| $^{+}O/^{+}N$ | Both | $\frac{\Gamma}{\Gamma}$ | 0.108 ± 0.006 | 0.032 ± 0.003 | > 0.035 | 0.054 ± 0.013 | 0.121 ± 0.004 | 0.033 ± 0.001 | 0.072 ± 0.002 | 0.036 ± 0.001 |
| N^{+2}/O^{+2} | Uni. | H L | 1.589 ± 0.913 | 0.062 ± 0.018 | 0.015 ± 0.007 | 0.103 ± 0.039 | : | : | : | : |
| N^{+2}/O^{+2} | Multi | IH IH | 2.230 ± 1.283 | 0.071 ± 0.022 | 0.021 ± 0.009 | 0.119 ± 0.049 | : | : | : | : |
| N^{+3}/O^{+2} | Uni. | $H \mid L$ | : | : | : | : | 0.024 ± 0.007 | 0.006 ± 0.000 | 0.023 ± 0.002 | 0.014 ± 0.001 |
| N^{+3}/O^{+2} | Multi | н н | : | : | : | : | 0.025 ± 0.007 | 0.006 ± 0.000 | 0.023 ± 0.001 | 0.015 ± 0.001 |
| $ICF(N^+)$ | | | 1.039 | 1.101 | 0.943 | 0.978 | 1.008 | 0.926 | 0.919 | 0.974 |
| $ICF(N^{+2})$ | | | 0.942 | 1.016 | 1.209 | 1.114 | 1.120 | 1.260 | 1.385 | 1.149 |
| $ICF(N^{+3})$ | | | 55.951 | 25.092 | 5.984 | 9.963 | 8.892 | 4.926 | 3.425 | 7.588 |
| $ICF(N^++N^{+2})$ | | | 0.977 | 1.029 | 1.184 | 1.095 | 1.111 | 1.236 | 1.370 | 1.131 |
| $ICF(N^{+2}+N^{+3})$ | | | 0.930 | 0.972 | 1.000 | 0.994 | 0.994 | 1.000 | 0.993 | 966.0 |
| $\log({ m N/O})_{ m N+}$ | Both | $\Gamma \mid \Gamma$ | -0.948 ± 0.021 | -1.476 ± 0.031 | > -1.529 | -1.386 ± 0.100 | -0.952 ± 0.015 | -1.516 ± 0.010 | -1.179 ± 0.009 | -1.487 ± 0.012 |
| $\log({\rm N/O})_{\rm N+2}$ | Uni. | H L | 0.175 ± 0.197 | -1.221 ± 0.113 | -1.838 ± 0.156 | -0.993 ± 0.149 | : | : | : | : |
| $\log({\rm N/O})_{\rm N+2}$ | Multi | HI HI | 0.322 ± 0.197 | -1.141 ± 0.115 | -1.595 ± 0.157 | -0.876 ± 0.140 | : | : | : | : |
| $\log({ m N/O})_{ m N+3}$ | Uni. | $H \mid L$ | • | : | : | : | -0.454 ± 0.108 | -1.493 ± 0.017 | -1.178 ± 0.022 | -0.807 ± 0.036 |
| $\log({\rm N/O})_{{ m N+3}}$ | Multi | н н | : | : | : | : | -0.645 ± 0.112 | -1.509 ± 0.018 | -1.107 ± 0.026 | -0.947 ± 0.039 |
| $\log(\mathrm{N/O})_{\mathrm{N}^+ + \mathrm{N}^{+2}}$ | Multi | All | 0.325 ± 0.194 | -1.077 ± 0.105 | > -1.358 | -0.852 ± 0.146 | : | : | : | : |
| $\log(\mathrm{N/O})_{\mathrm{N}+2~+~\mathrm{N}+3}$ | Multi | IH IH | | : | : | :: | • • • | | • • • | |
| 6 | | | 0 | | | | | | | |

z sample (see Section 6.1). Every $T_e(\mathrm{O}^{+2})$ derived for our low-z sample utilized the [O III] $\lambda 4364/\lambda 5008$ emission line ratio.

^a The low-ionization zone temperature for the constant- n_e model was calculated from $T_e(\mathrm{O}^+^2)$, determined with $n_e(\mathrm{S}^+)$ or $n_e(\mathrm{O}^+)$, using the NOTE— N^{+3} densities for galaxies without N^{+3} measurements are italicized for identification and were assumed to be $3.15 \times n_e(C^{+2})$ for the low-

^bThe low-ionization zone temperature for the 3-zone n_e model was calculated from $T_e(O^{+2})$, determined with $n_e(N^{+3})$, using the theoretical theoretical Garnett (1992) T_e-T_e relationship. Garnett (1992) $T_e - T_e$ relationship.

^cThe intermediate-ionization zone temperature for the 3-zone n_e model was calculated from $T_e(O^{+2})$, determined with $n_e(N^{+3})$, using the theoretical Garnett (1992) $T_e - T_e$ relationship.

Table 10. Ionic and Total N Abundances for High-z Sample

| | Model | Ion. Zone $T_e \mid n_e$ | $\frac{\text{RXC}}{\text{J2248-ID}^d}$ | $\mathrm{GN}	ext{-z}11^d$ | GDS 3073° | $\mathrm{Sunburst}^e$ | $\frac{J1723+}{3411^d}$ | $\begin{array}{c} \text{CEERS} \\ 1019^d \end{array}$ | $\frac{\rm SL2S}{\rm J0217}^e$ | Lynx^d | $\begin{array}{c} A1703 - \\ \text{zd6}^{d} \end{array}$ |
|---|-------------|--------------------------|--|---------------------------|-------------------|-----------------------|-------------------------|---|--------------------------------|--------------------|--|
| Densities (cm^{-3}) : | | | | | | | | | | | |
| $n_{e,low}(\mathbf{S}^+)(\times 10^2)$ | Both | <u>1</u> | 5.7 | 10.2 | 22.6 ± 9.0 | 17.0 ± 8.1 | 1.0 ± 0.2 | 6.1 ± 1.6 | 1.9 | 3.1 | 9.9 |
| $n_{e,int.}(C^{+2})(\times 10^4)$ | Multi | <u> </u> | 9.7 ± 0.4 | 32.4 | 22.2 | 8.3 ± 0.8 | 0.3 ± 0.2 | 7.4 | < 0.07 | 0.2 ± 0.2 | 8.4 ± 2.2 |
| $n_{e,high}(\mathbf{N}^{+3})(\times 10^5)$ | Multi | H | 3.1 ± 0.1 | 7.5 ± 1.0 | 3.9 ± 0.1 | 3.1 | 0.1 | 1.7 ± 0.3 | 0.0 | 1.0 ± 0.2 | 2.0 ± 0.1 |
| Temperatures (K): | | | | | | | | | | | |
| $T_{e,low}(\times 10^4)^a$ | Uni. | $\Gamma \mid \Gamma$ | 1.83 ± 0.01 | 1.33 ± 0.06 | 1.85 ± 0.03 | 1.08 ± 0.01 | 1.06 ± 0.02 | 2.05 ± 0.12 | 1.40 ± 0.14 | 1.50 ± 0.02 | 1.80 ± 0.03 |
| $T_{e,high}(O^{+2})(\times 10^4)$ | Uni. | $H \mid L$ | 2.19 ± 0.01 | 1.47 ± 0.09 | 2.21 ± 0.04 | 1.12 ± 0.02 | 1.09 ± 0.03 | 2.50 ± 0.17 | 1.57 ± 0.20 | 1.72 ± 0.03 | 2.14 ± 0.05 |
| $T_{e,low}(\times 10^4)^b$ | Multi | L H | 1.67 ± 0.01 | 1.18 ± 0.05 | 1.29 ± 0.01 | 1.03 ± 0.01 | 1.06 ± 0.02 | 1.93 ± 0.10 | 1.39 ± 0.14 | 1.47 ± 0.01 | 1.69 ± 0.03 |
| $T_{e,int.}(\times 10^4)^c$ | Multi | П Н | 1.80 ± 0.01 | 1.21 ± 0.06 | 1.34 ± 0.02 | 1.03 ± 0.02 | 1.07 ± 0.02 | 2.10 ± 0.12 | 1.46 ± 0.16 | 1.56 ± 0.02 | 1.82 ± 0.03 |
| $< 10^{4})$ | Multi | н н | 1.96 ± 0.01 | 1.25 ± 0.07 | 1.41 ± 0.02 | 1.04 ± 0.02 | 1.08 ± 0.03 | 2.33 ± 0.15 | 1.56 ± 0.20 | 1.67 ± 0.02 | 1.99 ± 0.04 |
| Ionization Parameters: | ers: | | | | | | | | | | |
| $\log U_{int.}(\mathrm{O}_{32})$ | Uni. | ГH | -1.000 | -1.670 | -1.615 | -1.279 | -2.105 | -2.015 | -1.500 | -1.000 | -1.000 |
| $\log U_{high}(\mathrm{N}_{43})$ | Multi | IH | -1.000 | -1.000 | -1.000 | : | | -1.000 | • • • | -1.000 | -1.000 |
| tal O | Abundances: | ances: | | | | | | | | | |
| $O^+/H^+(\times 10^{-5})$ | Both | $\Gamma \mid \Gamma$ | 0.022 ± 0.008 | 0.678 ± 0.171 | 0.136 ± 0.018 | 2.026 ± 0.409 | 3.777 ± 0.310 | 0.265 ± 0.048 | : | < 0.216 | < 0.096 |
| $O^{+2}/H^+(\times 10^{-5})$ | Uni. | H L | 3.116 ± 0.035 | 6.472 ± 1.636 | 1.757 ± 0.053 | 17.335 ± 1.683 | 14.900 ± 1.137 | 2.396 ± 0.363 | 3.040 ± 1.029 | 5.917 ± 0.266 | 3.152 ± 0.188 |
| $O^{+2}/H^+(\times 10^{-5})$ | Multi | н н | 5.360 ± 0.095 | 20.263 ± 5.832 | 7.320 ± 0.297 | 31.814 ± 3.414 | 15.238 ± 1.357 | 3.262 ± 0.505 | 3.072 ± 1.010 | 7.051 ± 0.373 | 4.525 ± 0.270 |
| $12 + \log(\mathrm{O/H})$ | Uni. | All L | 7.497 ± 0.005 | 7.854 ± 0.090 | 7.277 ± 0.013 | 8.287 ± 0.037 | 8.271 ± 0.027 | 7.425 ± 0.056 | > 7.483 | < 7.788 | < 7.512 |
| $12 + \log(\mathrm{O/H})$ | Multi | All | 7.731 ± 0.008 | 8.328 ± 0.105 | 7.888 ± 0.017 | 8.535 ± 0.042 | 8.279 ± 0.031 | 7.553 ± 0.058 | > 7.487 | < 7.862 | < 7.666 |
| Ionic and Relative N Abundances: | N Abu | ındances: | | | | | | | | | |
| $^{+}O/_{+}N$ | Both | $\Gamma \mid \Gamma$ | 1.624 ± 0.627 | : | < 0.131 | 0.083 ± 0.020 | 0.085 ± 0.009 | • | : | • | : |
| N^{+2}/O^{+2} | Uni. | H L | 0.059 ± 0.003 | 0.917 ± 0.721 | 1.624 ± 0.450 | 0.213 ± 0.075 | < 0.035 | 0.137 ± 0.073 | 0.014 ± 0.020 | 0.098 ± 0.017 | 0.078 ± 0.056 |
| N^{+2}/O^{+2} | Multi | HI HI | 0.079 ± 0.004 | 1.048 ± 0.848 | 1.886 ± 0.576 | 0.221 ± 0.085 | < 0.038 | 0.186 ± 0.095 | 0.020 ± 0.024 | 0.134 ± 0.018 | 0.106 ± 0.075 |
| N^{+3}/O^{+2} | Uni. | $H \mid L$ | 0.276 ± 0.011 | 0.570 ± 0.491 | 3.497 ± 1.733 | : | : | 0.544 ± 0.279 | : | 0.179 ± 0.030 | 0.145 ± 0.057 |
| N^{+3}/O^{+2} | Multi | н н | 0.288 ± 0.014 | 0.625 ± 0.575 | 3.902 ± 1.991 | : | : | 0.557 ± 0.257 | : | 0.186 ± 0.023 | 0.150 ± 0.057 |
| $ICF(N^+)$ | | | 0.915 | 1.065 | 0.939 | 1.280 | 1.090 | 0.895 | 0.920 | 0.934 | 0.907 |
| $ICF(N^{+2})$ | | | 1.470 | 1.152 | 1.396 | 1.191 | 0.981 | 1.534 | 1.290 | 1.409 | 1.495 |
| $ICF(N^{+3})$ | | | 2.944 | 6.735 | 3.430 | 2.353 | 41.966 | 2.658 | 4.440 | 3.328 | 2.816 |
| $ICF(N^++N^{+2})$ | | | 1.460 | 1.149 | 1.386 | 1.169 | 1.006 | 1.526 | 1.267 | 1.399 | 1.487 |
| $ICF(N^{+2}+N^{+3})$ | | | 0.989 | 0.993 | 0.992 | 0.956 | 0.960 | 0.987 | 0.999 | 0.991 | 0.988 |
| $\log({ m N/O})_{ m N+}$ | Both | $\Gamma \mid \Gamma$ | 0.134 ± 0.142 | : | < -1.078 | -1.006 ± 0.093 | -1.035 ± 0.040 | : | : | • | : |
| $\log(\mathrm{N/O})_{\mathrm{N}+2}$ | Uni. | $H \mid L$ | -1.038 ± 0.021 | 0.021 ± 0.245 | 0.315 ± 0.105 | -0.632 ± 0.128 | < -1.459 | -0.813 ± 0.176 | -1.746 ± 0.347 | -0.849 ± 0.068 | -0.921 ± 0.234 |
| $\log({ m N/O})_{ m N+2}$ | Multi | HI HI | -0.937 ± 0.024 | 0.082 ± 0.224 | 0.421 ± 0.116 | -0.580 ± 0.144 | < -1.426 | -0.544 ± 0.185 | -1.599 ± 0.326 | -0.725 ± 0.060 | -0.799 ± 0.234 |
| $\log({ m N/O})_{ m N+3}$ | Uni. | H L | -0.144 ± 0.016 | 0.645 ± 0.239 | 1.231 ± 0.173 | : | : | 0.733 ± 0.156 | : | -0.257 ± 0.070 | -0.422 ± 0.145 |
| $\log({ m N/O})_{ m N+3}$ | Multi | н н | -0.072 ± 0.022 | 0.624 ± 0.234 | 1.127 ± 0.178 | : | : | 0.170 ± 0.158 | : | -0.208 ± 0.056 | -0.375 ± 0.146 |
| $\log(\mathrm{N/O})_{\mathrm{N}^+ + \mathrm{N}^{+2}}$ | Multi | All | -0.907 ± 0.137 | : | < 0.416 | -0.579 ± 0.162 | < -1.236 | : | : | : | : |
| $\log(\mathrm{N/O})_{\mathrm{N}+2~+~\mathrm{N}+3}$ | Multi | HI HI | -0.441 ± 0.018 | 0.220 ± 0.176 | 0.759 ± 0.132 | | | -0.134 ± 0.132 | : | -0.499 ± 0.042 | -0.597 ± 0.139 |

Note— N^{+3} densities for galaxies without N^{+3} measurements are italicized for identification and were assumed to be $2.59 \times n_e \, (C^{+2})$ for the highz sample (see Section 6.1).

^aThe low-ionization zone temperature for the constant- n_e model was calculated from $T_e(O^{+2})$, determined with $n_e(S^+)$ or $n_e(O^+)$, using the theoretical Garnett (1992) $T_e - T_e$ relationship.

^bThe low-ionization zone temperature for the 3-zone n_e model was calculated from $T_e(\mathsf{O}^{+2})$, determined with $n_e(\mathsf{N}^{+3})$, using the theoretical Garnett (1992) $T_e - T_e$ relationship.

^cThe intermediate-ionization zone temperature for the 3-zone n_e model was calculated from $T_e(\mathsf{O}^{+2})$, determined with $n_e(\mathsf{N}^{+3})$, using the theoretical Garnett (1992) $T_e - T_e$ relationship.

^dThe $T_e(\mathsf{O}^{+2})$ measured for these objects used the O III] $\lambda 1666/\lambda 5008$ emission line ratio.

^eThe $T_e(\mathsf{O}^{+2})$ measured for these objects used the [O III] $\lambda 4364/\lambda 5008$ emission line ratio.